

FACIES, SEQUENCE STRATIGRAPHY AND RESERVOIR HETEROGENEITY OF THE
UPPER WOLFCAMPIAN GROUP (WOLFCAMP A EQUIVALENT): GLASS MOUNTAINS
OF WEST TEXAS

A Thesis

by

NICHOLAS MATTHEW DUSAK

Submitted to the Graduate and Professional School of
Texas A&M University
in partial fulfillment of the requirements for the degree of
MASTER OF SCIENCE

Chair of Committee,
Co-Chair of Committee,
Committee Member,
Head of Department,

Michael M. Pope
Arthur Donovan
Ibrahim Akkutlu
Julie Newman

August 2022

Major Subject: Geology

Copyright 2022 Nicholas Matthew Dusak

ABSTRACT

The Latest Artinskian to Early Kungurian Upper Wolfcamp (Skinner Ranch) Formation is exposed in the Lenox Hills of the Glass Mountains in Brewster County, Texas. These outcrops provide geoscientists and engineers a window to examine strata equivalent to the Wolfcamp A unconventional reservoirs in the southern Delaware Basin. This study provides an outcrop-based sequence stratigraphic analysis to identify distinct chemo/litho facies within a regionally correlative framework for improved reservoir characterization of organic-rich, mudrock-dominated successions. We use modern advances in Energy-Dispersive X-Ray Fluorescence (ED-XRF) chemostratigraphy to better understand depositional constraints on reservoir quantity (spatio-temporal variations) and quality (compositional, TOC richness) within a mixed carbonate-siliciclastic system.

Within the Lenox Hills, the Upper Wolfcamp Formation consists from the base up of the: 1) carbonate conglomerate-prone Decie Ranch Member, 2) organic rich, mudstone-prone Poplar Tank Member, 3) mixed carbonate-siliciclastic conglomerate-prone Sullivan Peak Member, and (4) the organic poor, mudstone-prone Dugout Mountain Member. The lowermost three members of the Upper Wolfcamp Formation, especially the mudstone-prone Poplar Tank Member, were the focus of this study. Five facies were identified within the Poplar Tank Member: 1) Facies 1a (skeletal packstone/grainstone) and 1b (skeletal wackestone), Facies 2 (calcareous silty mudstone), Facies 3 (argillaceous shale/mudstone), Facies 4 (siliceous mudstone/siltstone), and Facies 5 (siliceous shale/siltstone). Within the Poplar Tank Member, the heterogeneity of the observed facies and elemental proxies throughout the lower depositional sequence of the Upper Wolfcamp Formation suggest strong depositional cyclicity. Detrital and paleo-redox proxies indicate increase

in siliciclastic deposition occurred during the interpreted TST and early HST, and carbonate deposition occurring during the interpreted late TST and HST.

Comparison of reservoir quality between the Upper Wolfcamp mudstone in outcrop and core studies indicate an equivalence of strata to the informal “Wolfcamp A” reservoirs in the subsurface of the Delaware Basin. Likewise, preliminary analysis of the shale/siltstone at the base of the Dugout Mountain Member indicate a correlation to the X, Y, and Z Sands of the Wolfcamp A. These findings, coupled with complete sedimentary and geochemical analysis of the type Upper Wolfcamp (Skinner Ranch) Formation provides chronostratigraphic insights for the surface to subsurface correlations. This work indicates that to make the Wolfcamp Group in outcrop coeval to the Wolfcamp Group in the subsurface, the base of the Leonard Group (Bone Springs) should be placed at the base of the Wedin Member of the overlying Cathedral Mountain Formation.

DEDICATION

I dedicate this thesis to my fiancée, Mariana Figueroa, and to my parents. Your constant support and encouragement have largely influenced my academic success.

ACKNOWLEDGEMENTS

I would not be able to complete my works without the tremendous support of my advisors, Drs. Art Donovan, Michael Pope, and I. Yucel Akkutlu. Your trust and guidance were critical in the success of my project and degree as a whole. There are countless lessons that each of you taught me that will remain with me as I progress in industry and life.

I am also appreciative of the Unconventional Reservoir and Outcrop Characterization (UROC) Consortium in the College of Geosciences at Texas A&M University for funding not only my research, but also the works of the other Master and Ph.D. students that have successfully graduated due to your inherent interests and contributions. Thank you to the folks at Chemostrat for being reliable and responsive in aiding our geochemical analysis.

Lastly, there are many others that contributed to this study. Thank you, Eric Peavey, Ben Richards, Conor Sullivan, Parker Johnson, Alex Ferrell, Maria Gutierrez, and Jake Sleight, for your assistance. Whether that be provided data, academic references and discussions, guidance, or personal reassurance, this project is a reflection of all of your help.

CONTRIBUTORS AND FUNDING SOURCES

Contributors

This research was supervised by a thesis committee consisting of Drs. Michael Pope, Arthur Donovan of the Department of Geology and Geophysics, and Ibrahim Akkutlu of the Department of Petroleum Engineering.

Funding

This study was funded by the supporting members of the Unconventional Reservoir and Outcrop Characterization (UROCC) Consortium, the Houston Geological Society (HGS), and the Society of Independent Professional Earth Scientists (SIPES).

TABLE OF CONTENTS

	Page
ABSTRACT.....	ii
DEDICATION.....	iv
ACKNOWLEDGEMENTS.....	v
CONTRIBUTORS AND FUNDING SOURCES	vi
TABLE OF CONTENTS.....	vii
LIST OF FIGURES	ix
LIST OF TABLES	xiii
1 INTRODUCTION.....	1
2 GEOLOGIC SETTING.....	5
2.1 Permian Basin	5
2.2 Glass Mountains (West Texas)	7
3 METHODS.....	9
3.1 Measured Sections and Sampling	9
3.2 Handheld Gamma Ray	10
3.3 Geochemistry (FTIR and ED-XRF).....	11
3.4 Petrographic Thin Sections	12
3.5 Spotfire Clustering and Facies Association	13
4 RESULTS.....	14
4.1 Bulk Geochemical and Sedimentary Characteristics	14
4.1.1 Upper Wolfcamp (Skinner Ranch) Mineralogical Composition.....	14
4.1.2 Poplar Tank Facies	17
4.1.2a Facies 1a (Skeletal Packstone/Grainstone)	20
4.1.2b Facies 1b (Skeletal Wackestone)	21
4.1.2c Facies 2 (Calcareous Silty Mudstone).....	21
4.1.2d Facies 3 (Argillaceous Shale/Mudstone)	22
4.1.2e Facies 4 (Siliceous Mudstone/Siltstone)	22
4.1.2f Facies 5 (Siliceous Shale/Siltstone).....	23
4.2 Elemental Distribution and Proxies.....	23
4.3 Vertical and Lateral Distribution and Depositional Architecture	27

5	DISCUSSION.....	30
5.1	Chemo/Sequence Stratigraphy and Depositional Model	30
5.1.1	Depositional Model	30
5.1.2	Lowstand Systems Tract (LST).....	32
5.1.3	Transgressive Systems Tract (TST)	33
5.1.4	Highstand Systems Tract (HST).....	34
5.2	Geochemistry	35
5.2.1	Upper Wolfcamp Formation.....	35
5.2.2	Upper Wolfcamp Group Mudstone	36
5.3	Wolfcamp A Delineation: Outcrop to Subsurface Correlation	37
5.4	Implications for Reservoir Heterogeneity	38
6	FUTURE WORK	40
7	CONCLUSIONS	41
	REFERENCES	44
	APPENDIX.....	52

LIST OF FIGURES

	Page
Figure 1. Historical stratigraphic chart summarizing regional interpretations on the Lower Permian Wolfcamp Group of the Glass Mountains (Ross & Ross, 2003; Cooper & Grant, 1972). Red line highlights the sequence stratigraphic findings of this study within outcrop and subsurface equivalents within the Delaware Basin (Sleight et al., 2020; Gutierrez et al., in prep; Peavey et al., 2022; Richards et al., 2022).	4
Figure 2. Palaeoceanographic reconstruction of Pangea from the Late Pennsylvanian (left) and Early Permian (right). Modified from Blakey (2019).....	7
Figure 3. Reconstructed geologic map of representative exposed strata along the Glass Mountains of West Texas. Map inspired by King (1937) and regional studies of the Unconventional Reservoir and Outcrop Characterization (UROC) Consortium at Texas A&M University. Base layer is google terrain map from geolocate.....	10
Figure 4. Photograph of the front of the Lenox Hills looking in the direction of dip (NW). Member name (white) and outcrop exposure contacts (yellow) are denoted.	10
Figure 5. Average mineralogy of the Decie Ranch, Poplar Tank, and Sullivan Peak Members derived from Fourier transform infrared (FTIR) spectroscopy measurements.....	15
Figure 6. Linear relationship between FTIR and ED-XRF data establishing correlation between: (A) measured quartz (yellow); (B) calcite (blue); (C) and total clay (brown) minerals within Section 8.....	17
Figure 7. Type thin section and outcrop representation of each respective facies.	19
Figure 8. (A) Compositional distribution of mudstones based on XRD-based mudstone organofacies classification modified from Donovan et al., (2017). (B) Average mineralogy measured from FTIR.....	20
Figure 9. (A) Paleoredox through time at each measured section is illustrated and denoted by elemental distribution of U/Th values. Anoxic/suboxic conditions (Facies 1 and 2, red color), oxic/suboxic (Facies 3 and 4, yellow color), oxic (Facies 5, dark green color). Sequence stratigraphic interpretations denoted by the transgressive surface (WC75ts and WC90ts – green line), maximum flooding surface (WC75mfs – blue line), and sequence boundary (WC90sb – red line). (B) Average values of paleoredox proxies and interpreted redox conditions of the paleo-environment denoted in table.....	25
Figure 10. Paleoproductivity/bioproduktivty illustrated by measured values of nickel (Ni), colored by Facies representation at each measured section. Sequence stratigraphic interpretations denoted by the transgressive surface (WC75ts and WC90ts – green line), maximum flooding surface (WC75mfs – blue line), and sequence boundary (WC90sb – red line). Increase in nickel values indicate zones with higher TOC	

content, as seen around the WC75mfs. Average value of nickel trends higher moving each section to the right, interpreted as greater organic accumulation. 26

Figure 11. Cross plot of ED-XRF measured silica (SiO₂) Zr at Section 8. Detrital silica trend shown in black. Biogenic/authigenic silica trend shown in red. Data points are colored by their respective facies. Facies 1 does not show a correlation. Facies 2 and 5 have a detrital silica trend. Facies 3 and 4 trend along with biogenic/authigenic silica. 27

Figure 12. Gray-scaled (top) and ultra-violet light (bottom) of the digital outcrop model (DOM) of the Lenox Hills. Measured section locality illustrated in yellow. Depositional architecture is detailed in the red outline of the exposed members, which was captured by roughly 2.5 miles of collected drone photogrammetry. Interpreted faults are shown in white, along with direction of fault displacement. 28

Figure 13. Gray-scaled digital outcrop model (DOM) of the Lenox Hills. Locality of sections and members are denoted in yellow. Geometries of the Decie Ranch and Sullivan Peak members are outlined in red. Quantitative vertical distribution of facies abundance at each measured section is illustrated by the associated pie charts. Facies 1 and 4 distributions vary between sections. Facies 2 increases from the southwest to northeast. Inversely, distribution of facies 3 decreases from southwest to northeast. Facies 5 not shown because its total thickness is not determined..... 29

Figure 14. Interpreted depositional model of the Lower Member (Decie Ranch and Poplar Tank members) of the Upper Wolfcamp Formation. Dominant lithotypes throughout the depositional sequence are illustrated in the lower right box. Modified from Li et al., (2015). 32

Figure 15. Elemental distribution, outcrop description, total gamma ray, and facies of Section 8. Sequence boundary (red), transgressive surface (green), and maximum flooding surface (blue) based on observed outcrop sedimentology, total gamma ray, and chemostratigraphic proxies. 35

Figure A 1. Dendrogram visualization tree produced in TIBCO Spotfire. Rows of ED-XRF data are clustered together (y-axis) and based on similarity of elemental data, specifically relative abundance clastic/detrital, carbonate, redox, and bioproductivity/paleoproductivity proxies (x-axis). Higher measured elemental abundance is colored red, lower abundance in blue.....59

Figure A 2. Partitioning index displaying elemental distribution between each facies derived from hierarchal clustering. Elements are colored and listed in order of significance for each facies. 60

Figure A 3. Th-K cross plots demonstrating clay mineralogy within the Poplar Tank Member at each measured section. Plots indicate that the dominant clay mineralogy is illite and mixed layer..... 60

Figure A 4. (A) Paleoredox through time at each measured section is illustrated and denoted by elemental distribution of V/Cr values. Anoxic/suboxic conditions (Facies 1 and 2, red color), oxic/suboxic (Facies 3 and 4, yellow color), oxic (Facies 5, dark green color). Sequence stratigraphic interpretations denoted by the transgressive surface (WC75ts and WC90ts – green line), maximum flooding surface (WC75mfs – blue line), and sequence boundary (WC90sb – red line). (B) Average values of paleoredox proxies and interpreted redox conditions of the paleo-environment denoted in table..... 61

Figure A 5. (A) Paleoredox through time at each measured section is illustrated and denoted by elemental distribution of V/(V+Ni) values. Anoxic/suboxic conditions (Facies 1 and 2, red color), oxic/suboxic (Facies 3 and 4, yellow color), oxic (Facies 5, dark green color). Sequence stratigraphic interpretations denoted by the transgressive surface (WC75ts and WC90ts – green line), maximum flooding surface (WC75mfs – blue line), and sequence boundary (WC90sb – red line). (B) Average values of paleoredox proxies and interpreted redox conditions of the paleo-environment denoted in table..... 62

Figure A 6. Paleoproductivity/bioproductivity illustrated by measured values of uranium (U), colored by Facies representation at each measured section. Sequence stratigraphic interpretations denoted by the transgressive surface (WC75ts and WC90ts – green line), maximum flooding surface (WC75mfs – blue line), and sequence boundary (WC90sb – red line)..... 63

Figure A 7. Paleoproductivity/bioproductivity illustrated by measured values of chromium (Cr), colored by Facies representation at each measured section. Sequence stratigraphic interpretations denoted by the transgressive surface (WC75ts and WC90ts – green line), maximum flooding surface (WC75mfs – blue line), and sequence boundary (WC90sb – red line)..... 63

Figure A 8. Skeletal wackestone with numerous fine-grained bioclasts. Abundant calcareous sponge spicules as well as lime mud. Organic matter occurs as black discontinuous lenses..... 64

Figure A 9. Box plot comparison of measured TOC from each facies. Median and mean of TOC is denoted by the solid black line and x, respectively, within each box. Higher average TOC values are plotted within Facies 2 (calcareous silty mudstone) and Facies 4 (siliceous mudstone/siltstone). Basal Dugout Mountain shale and siltstone of Facies 5 contains the lowest TOC content. 65

Figure A 10. Elemental distribution, outcrop description, total gamma ray, and facies of Section 8B. Sequence boundary (red), transgressive surface (green), and maximum flooding surface (blue) based on observed outcrop sedimentology, total gamma ray, and chemostratigraphic proxies. 65

Figure A 11. Elemental distribution, outcrop description, total gamma ray, and facies of Section 10. Sequence boundary (red), transgressive surface (green), and maximum

flooding surface (blue) based on observed outcrop sedimentology, total gamma ray, and chemostratigraphic proxies. 66

Figure A 12. Stratigraphic correlations between measured sections of the study area. Outcrop description, total gamma ray, and gross compositional profiles of the respective members were illustrated within Easycore software. Sequence stratigraphic interpretations denoted by the transgressive surface (WC75ts and WC90ts – green line), maximum flooding surface (WC75mfs – blue line), and sequence boundary (WC90sb – red line)..... 66

LIST OF TABLES

	Page
Table 1. Integrated geochemical and sedimentary characterization of facies based on clustering of normalized ED-XRF elements and petrographic thin section analysis.	18
Table 2. List of elements/elemental ratios and their interpreted proxies.....	24
Table A 1. 648 rows of data from ED-XRF measurements from samples collected from the Decie Ranch, Poplar Tank, Sullivan Peak, Dugout Mountain members.....	59

1 INTRODUCTION

Early Permian strata, commonly mapped as the Skinner Ranch Formation in the Lenox Hills (Cooper and Grant, 1973; Ross and Ross, 2003), but herein termed the Upper Wolfcamp Formation to better convey superposition within the Wolfcamp Group, as well as to avoid local provincial nomenclature, outcrop along the Glass Mountains in Brewster County, Texas. These Early Permian strata, located at the margin of the Marathon fold-belt region, record sedimentary fill of foreland basin strata, that formed because of the Late Paleozoic collision of the Laurentia and Gondwana plates and assembly of Pangea (Hill, 1995; Ye et al., 1996; Poole et al., 2005; Soto-Kerans et al., 2020). The resulting complex syn-tectonic stratigraphic history provides a challenge in establishing a consistent stratigraphic framework of the Pennsylvanian and Permian units throughout the Glass Mountains. In this study, high-resolution sequence stratigraphic methods, as well as chemostratigraphic (XRF) data, are used to resolve biostratigraphic boundaries of the basal facies of the Upper Wolfcamp Formation, which are coeval to the unconventional tight- and source-rock plays of the Wolfcamp A unit in the adjacent subsurface in the Delaware Basin. This study also utilized a multi-scale approach, which ranged from petrographic thin section analysis of the fine-grained strata to seismic-scale drone photography to better constrain the large-scale reservoir architectures exposed in Upper Wolfcamp Formation in the Lenox Hills.

As mentioned previously, the Upper Wolfcamp Formation deposits exposed along the southeast face of the Lenox Hills of the Glass Mountains provides an exceptional opportunity to study slope and sea-floor associated strata (Cooper and Grant, 1964, 1966, 1972; Rogers, 1978; Cys and Mazzullo, 1978, 1981) coeval to the productive Wolfcamp A interval in the subsurface in the Delaware Basin. Historically, these Early Permian strata received little attention due to their

mudstone-dominated facies, and location on private property, however, with recent interest in similar coeval facies as unconventional reservoirs in the Delaware Basin, studies of these outcrops is now critical and timely.

At its type locality in the Lenox Hills, the Upper Wolfcamp (Skinner Ranch) Formation is a mixed carbonate-siliciclastic unit, approximately 420' (128 meters) thick, comprised of interbedded assemblage of limestone conglomerate, organic-rich shale, siltstone, sandstone, calcareous siltstone, and limestone (Cooper and Grant, 1964, 1972; Cys and Mazzullo, 1978; Cys, 1981; Ross and Ross, 2003). In the subsurface of the Delaware Basin, the coeval Wolfcamp A Formation ranges in thickness from 100 ft. to 700 ft., and contains an estimated undiscovered hydrocarbon resource of 29 billion barrels of oil, 220 trillion cubic feet of natural gas, and 14 billion barrels of natural gas liquids (Gaswirth et al., 2018; EIA, 2020). Exploitation of these reservoirs has garnered interest, largely within the last decade due to enhanced production and completion technologies that which provides economic incentive to develop these previously undeveloped petroleum resources.

Previous geologic studies in the area primarily focused on biostratigraphic markers to constrain the Upper Wolfcamp (Skinner Ranch) Formation from its platform to basinal facies (Hill, 1995). As a result of this biostratigraphic focus, little work on the facies, depositional setting, and sequence stratigraphy of these strata were previously conducted. During the early 20th Century, Udden and King provided a comprehensive account of the Pennsylvanian and Permian units within the Glass Mountains (Udden, 1917; King, 1930). Later, Ross sub-divided King's Wolfcamp Formation into the Neal Ranch and Lenox Hills formations based on stratigraphic interpretations from their descriptions of changing fusulinid faunas (Ross, 1960, 1963). Because of this work

(Figure 1), Ross (1986) placed the start of the Leonard Group at the base of the Skinner Ranch Formation, coinciding with the first occurrence of the fusilinid *Schzuagerina crassitectoria*, a fusilinid that appears in the Decie Ranch Member (base Skinner Ranch Formation) within the Lenox Hills. Within Ross's stratigraphic framework, the Wolfcamp Group (Figure 1) spans the Asselian to Artinskian stages on the Geologic Time Scale (Cohen et al., 2013).

Cooper and Grant (1964, 1972) also studied these outcrops, and in their research determined that the mudstone-dominated Skinner Ranch Formation was coeval to the carbonate-dominated shelf-margin deposits of the Hess Formation (Figure 1). These correlations were based on an occurrence of the fusilinid *Schzuagerina crassitectoria* in the top of the Skinner Ranch and Hess formations (Cooper and Grant, 1964, 1972; Ross, 1986). In their work, Cooper and Grant (1964, 1966, 1972) sub-divided the Skinner Ranch Formation from the base up into the (conglomerate-dominated) Decie Ranch, (mudstone-dominated) Poplar Tank, (conglomerate-dominated) Sullivan Peak, and (mudstone-dominated) Dugout Mountain members. Within their stratigraphic framework, Cooper and Grant (1972) placed the base of the Leonard Group at the base of the overlying Cathedral Mountain Formation (Figure 1). Based on the work of Cooper and Grant (1972), the Wolfcamp Group, as defined by them (Figure 1), spans the Asselian to Early Kungurian stages on the Geologic Time Scale (Cohen et al., 2013).

While most subsequent biostratigraphic studies have typically assigned the Skinner Ranch Formation in the Lenox Hills to the Leonard Group (Cys and Mazzullo, 1978; Cys, 1981; Davydov et al., 1995; Wahlman and West, 2010; Cohen et al., 2013; Wardlaw and Nestell, 2019), strata mapped as the Wolfcamp A in the subsurface appear to be Kungurian (Wilde 1975; Reid et al., 1988; Cohen et al., 2013; Kohn et al., 2016). However, this study (Figure 1) followed the

2 GEOLOGIC SETTING

2.1 Permian Basin

The greater Permian Basin, which is a large geologic province located in West Texas and southeast New Mexico, is one of the largest hydrocarbon producing basins in the United States (Gaswirth et al., 2018; EIA, 2020). This complex foreland basin is segmented into the western Delaware Basin, the structural uplifted Central Basin Platform, the eastern Midland Basin, and the southern Val Verde Basin. Stratigraphic and structural evolution of the greater Permian Basin can be observed through geologic time, with emphasis on two principal partitions which began in the Cambrian and rapidly developed throughout the Permian (Adams, 1965; Ewing, 2016).

Throughout the Early and Mid-Paleozoic, a transcontinental arch formed along the southern cratonic margin of Laurentia, forming an adjacent extensional marine depression, commonly referred to as the Tobosa Basin (Galley, 1958; Adams, 1965; Adams and Keller, 1996; Ewing, 2016). Marine incursion onto this cratonic margin throughout the Early Ordovician deposited of the Ellenburger Group, which is comprised of widespread shelf carbonate, as well as deep-water mudstone and carbonate (Yang and Dorobek, 1995; Derby et al., 2012). From the Mid to Late Ordovician, tectonic warping formed an intracratonic sag (Tobosa Basin) bounded by the Texas and Diablo Archs (Galley, 1958; Adams, 1965; Adams and Keller, 1996; Ewing, 2016). Deposition sourced from the northwest highlands provided sediment infill of marginal-marine and fine-grained offshore carbonate along extended platform and ramp settings (Wuellner et al., 1986). Continual deposition and subsequent suppression of the basin lasted through the Mississippian.

During the Carboniferous, depocenters formed along the axis of the Tobosa Basin during early collision of the Laurentia and Gondwana plates (Figure 2). Foredeep facies were thrust to the northwest by displacement of the Gondwana plate. Cratonic shortening along the thrust front coincided with depressed sub-basins and crustal uplifts of the Tobosa Basin (Yang and Dorobek, 1995; Ewing, 2016, 2019). Partitioning of the ancestral basin formed the Delaware Basin, Midland Basin, and Central Basin Platform, respectively. Continued tectonic loading and subsidence caused evolution and maturity of the basins. Deposition of fine-grained sand, limestone, and mudstone, on the sea floor, along with limestone-dominated deposition on the shelf, dominated Permian deposition (King, 1930; Ross, 1986; Hill, 1995). The resultant assemblage of facies and stratigraphy that make up the bulk of the Greater Permian Basin was a result of cyclic-sedimentation infill driven by the complex interplay between tectonics and eustacy (Hill, 1995; Poole et al., 2005; Soto-Kerans et al., 2020; Wilson et al., 2020).

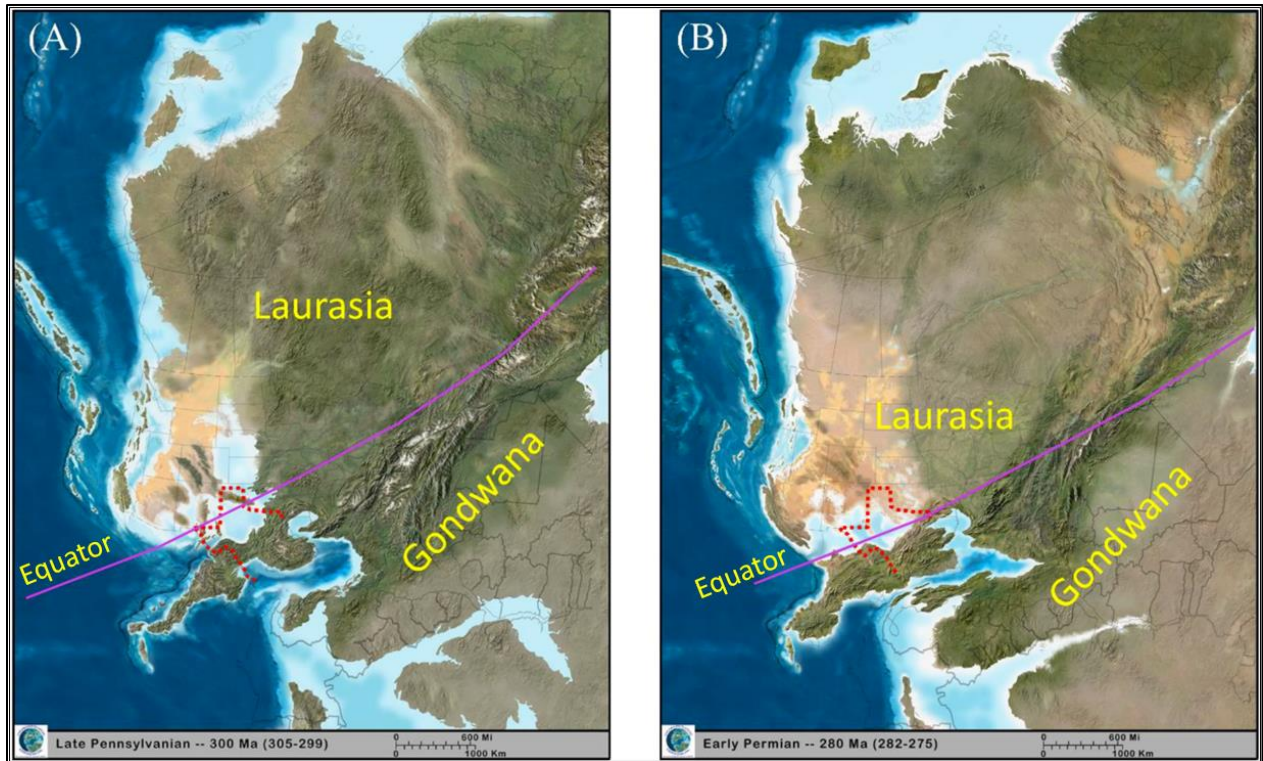


Figure 2. Palaeoceanographic reconstruction of Pangea from the Late Pennsylvanian (left) and Early Permian (right). Modified from Blakey (2019).

2.2 Glass Mountains (West Texas)

The Glass Mountains of West Texas are located on the southwest flank of the Delaware Basin within the greater Permian Basin (Figure 3). The Glass Mountains are mainly comprised of Permian strata with an overall southwest to northeast strike and dip sloping to the northwest. These Permian sediments record deposition along a profile that extends from a carbonate platform to mudstone-prone seafloor setting (Cooper and Grant, 1964, 1966, 1972; Ross, 1986; Ross and Ross, 2003). The stratigraphy and structure of the Glass Mountains are a result of the paleo deposition and regional deformation along the Ouachita-Marathon orogenic belt (King, 1930; Cooper and Grant, 1972; Ross, 1986; Wuellner et al., 1986; Poole et al., 2005). During the Carboniferous, the Marathon hinterland region experienced an uplift and increase of siliciclastic deposition in accordance with the onset of the southern subduction of the Laurentia plate under Gondwana (Hill,

1995; Poole et al., 2005). The peripheral foredeep and foreland-basin system developed structural lows that captured basin-fill sediment along continental margins in deep marine settings. As the Carboniferous progressed, the Marathon fold-and-thrust belt formed by renewed tectonic flexure along sutures derived from ancestral rifts during the break up of Rodinia (Poole et al., 2005; Pyles et al., 2010; Soto-Kerans et al., 2020). Throughout the evolution of the Marathon Orogenic belt, the continental margin deposits located between the collisional margins were thrust, forming an accretionary wedge that advanced northward over Laurentia continental shelf deposits (Ross, 1986; Ye et al., 1996; Ross and Ross, 2003; Poole et al., 2005). By Early Permian (Wolfcamp) deposition, northward structural propagation of the Marathon Orogen became stable, ushering in a period of undisturbed reciprocal sedimentation in a mixed carbonate-siliciclastic depositional system (Hill, 1995; Soto-Kerans et al., 2020). Diminishing structural intensity is recorded in the rock record as the undisturbed strata overlying the angular unconformity at the base of the Gaptank Formation in the Glass Mountains (Ross, 1986). Deposition of the Lenox Hills, Skinner Ranch, and Cathedral Mountain Formations occurred during the Early Permian to early Late Permian (Cooper and Grant, 1964, 1966, 1972; Ross, 1986; Hill, 1995; Ross and Ross, 2003). Renewed folding and uplift began during the Late Cretaceous to Early Tertiary Laramide Orogeny, forming a structural high and a broad dome in the Glass Mountain region, which led to the erosion of less resilient beds and exposed the currently outcropping strata in the Glass Mountains (King, 1930; Wuellner et al., 1986; Winfree, 1994, 1995; Cherney et al., 1998).

3 METHODS

3.1 Measured Sections and Sampling

Vertical and lateral facies heterogeneity within the Upper Wolfcamp Formation in the Lenox Hills is documented in the three detailed measured sections collected in this study (Figure 3 and 4). Each section was recorded using a 1.56-meter-tall Jacob's Staff and Brunton Compass, measuring parallel to dip. Sampling of the Decie Ranch and Sullivan Peak members varied, however sampling of the mudstone-dominated Poplar Tank Member was at a consistent interval of every foot, when well exposed. Samples were systematically acquired for sedimentological rock descriptions at the hand sample scale for geochemical evaluation and petrographic thin section analysis.

Drone and outcrop photography was utilized to aid in providing seismic-scale architecture of the respective members, as well as to document sampling localities within the measured sections. Aerial images were taken by a DJI Phantom 4 Pro drone, which flew parallel to strike. The images were then processed using the guided workflow within Agisoft Metashape, where they were optimally aligned, filtered, and projected into 3-D space via a dense point cloud and textured model. Lastly, the segmented drone images captured along the Lenox Hills were imported into the drone visualization software Lime, where the newly rendered digital outcrop model (DOM) was texturized and colored based on properties such as dip/slope.

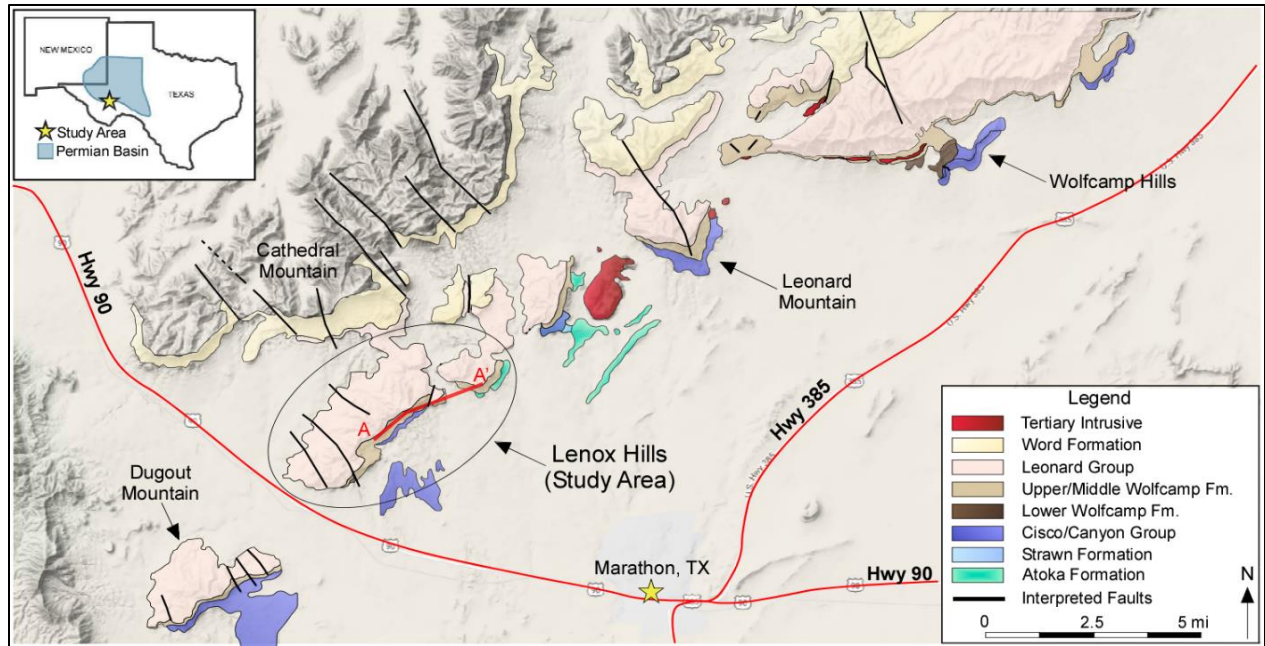


Figure 3. Reconstructed geologic map of representative exposed strata along the Glass Mountains of West Texas. Map inspired by King (1937) and regional studies of the Unconventional Reservoir and Outcrop Characterization (UROC) Consortium at Texas A&M University. Base layer is google terrain map from geolocate.

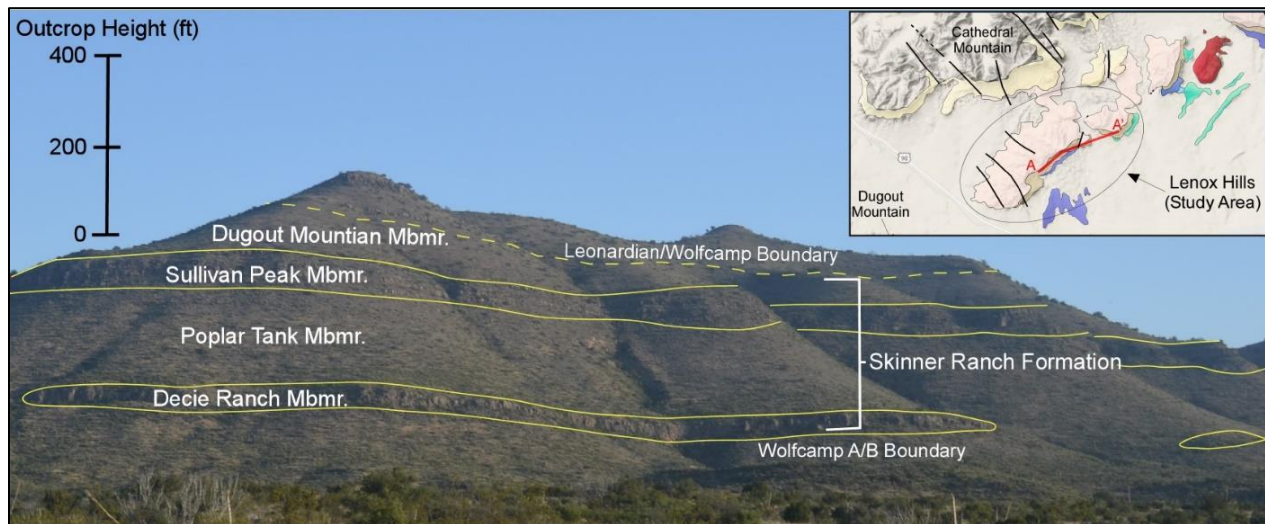


Figure 4. Photograph of the front of the Lenox Hills looking in the direction of dip (NW). Member name (white) and outcrop exposure contacts (yellow) are denoted.

3.2 Handheld Gamma Ray

A RS-230 handheld gamma-ray scintillometer was utilized to record a spectral gamma-ray (SGR) profile for each stratigraphic section. Gamma-ray measurements were taken at a one-foot

interval for 60-second assays within each member, with an exception to the Poplar Tank of Section 10 where outcrop exposure in the upper 20 feet was completely covered. The mass concentrations of Uranium²³⁸, Potassium⁴⁰, and Thorium²³² associated with the scintillometer measurements help derived a total gamma-ray profile inspired by methods established by Herron and Herron (1996). The total gamma-ray profiles of each section allow for a direct comparison of the radioactivity patterns with subsurface gamma-ray well logs to resolve sequence stratigraphic correlations and improve geologic interpretations. Vertical clay variability within the mudrocks were observed by creating a Thorium-Potassium cross-plot and correlating the results to the clay minerals recorded from Fourier transform infrared (FTIR) spectroscopy measurements from Section 8 samples. Thorium-Potassium cross-plots for Sections 8B and 10 also were generated and analyzed to better understand lateral variation of clay mineralogy within the study area (Figure A3).

3.3 Geochemistry (FTIR and ED-XRF)

Mineralogical components were recorded using Fourier transform infrared (FTIR) spectroscopy. FTIR was used because of its comparable results to that of X-Ray Diffraction (XRD) measurements as well as the effectiveness and timely manner in which the samples were processed (Craddock et al., 2017). Samples were prepped and processed by an external industry vendor (Chemostrat). Mineral percentages are reported alongside measured organics within the samples acquired from the Upper Wolfcamp at the type section of this study. FTIR data was analyzed only from Section 8 samples.

In order to provide a correlative mineralogical analysis within the other two sections that did not have FTIR data, a stoichiometric correlation between the ED-XRF and FTIR data of Section 8 was established (Figure 6). Then, we generated an “XRF Composition” column to

provide a rough lithologic profile differentiating between quartz (silica), clay (aluminum), and calcite (calcium) for each section.

Bulk samples from the outcrop were powdered by running a SPEX SamplePrep 8000M Mixer Mill for 5 minutes, and then sieving the powdered sample through a <90 μm mesh into 4-gram aliquots. The powders were then pressed into compact cylindrical pellets using a Specac Manual Hydraulic Press. Pellets were used for Energy Dispersive X-Ray Fluorescence (ED-XRF) measurements taken by a Bruker Tracer 5g Handheld ED-XRF. An 8 mm spot size count under a 1 μm Graphene detector window was used to minimize X-Ray scatter and statistical noise from the elemental abundance readings. The mudstone setting was used to determine major elements (wt.%), as well as trace elements (ppm). Additionally, elements were recorded in their respective oxide concentrations.

3.4 Petrographic Thin Sections

23 petrographic thin sections were prepared and analyzed using an Olympus BX53MTRF Petrographic microscope located in the Carbonate Petrology Lab at Texas A&M University. The petrographic microscope was paired with a digital imaging software (Olympus Stream Essentials 2.1) to easily export visual representations of observed textures (grain size and sorting), minerals, sedimentary structures, porosity, clasts, and mud. Each thin section was categorized using the Dunham (1962) classification for carbonate samples, or Folk (1968) and Donovan et al. (2017) for siliciclastic samples. The thin sections themselves were prepared by Wagner Petrographic at a thickness of 20 μm . Each thin section was impregnated with a blue epoxy for visual representation of porosity, as well as stained with Alizarin Red to help identify calcite within most of the carbonate dominated thin sections (Dickson, 1965).

3.5 Spotfire Clustering and Facies Association

All 648 rows of ED-XRF data were compiled into a single spreadsheet (Table A1). Columns comprised of major and trace elements were filtered based on which geochemical proxies warranted interest in providing insights into the environmental conditions at the time of deposition. Due to the scale at which the major and trace elements are reported (wt.% vs ppm), we chose to normalize the data between 0 and 1 before exporting it into the TIBCO Spotfire software. Agglomerative hierarchical clustering was performed in order to group rows (sample depth within each measured section) based on their elemental similarities (Figure A1). Ward's Method was chosen to derive clusters due to its quantitative significance in reducing variance within clusters while maintaining maximum variance between each cluster (Temple et al., 2008; Roush, 2015). This is useful in order to assure that our clusters provide geologic significance within the context of our facies and sequence stratigraphic model.

Once the desired number of clusters were chosen, we exported the cluster ID, along with their correlative sample numbers, into Excel. In order to quantify which elements are representative and/or significant within each cluster, we utilized a partitioning index and derived an elemental rank (Figure A2) outlined in Phillip (1991). Descriptive sedimentological analysis from our petrographic thin sections was integrated with their labeled geochemical cluster IDs in order to characterize an incorporated chemo/litho facies. Analyzing the geochemical nature, as well as the lithologic characteristics of each respective cluster, was used in order to provide a descriptive facies name.

4 RESULTS

The three stratigraphic measured sections of the Upper Wolfcamp Formation along the Lenox Hills record lithologic, mineralogical, and geochemical heterogeneity. Over 648 samples were collected from these three sections, of which, 247 samples were gathered from the Decie Ranch and Sullivan Peak members, and 401 samples from the Poplar Tank and overlying Dugout Mountain members. All 648 were prepped and processed for Energy Dispersive XRF, and 193 were measured for Fourier transform infrared spectroscopy. From the type section (Section 8), 23 petrographic thin sections were analyzed for sedimentological characterization of representative carbonate and siliciclastic strata.

4.1 Bulk Geochemical and Sedimentary Characteristics

4.1.1 Upper Wolfcamp (Skinner Ranch) Mineralogical Composition

Average mineralogical abundance (wt.%) of the members of the Upper Wolfcamp Formation is illustrated on Figure 5. One-hundred ninety-three (193) measurements of: quartz, potassium, feldspar, plagioclase, chlorite, illite/smectite/mica, kaolinite, calcite, ankerite/dolomite, pyrite, and organics; record the bulk compositional differences among the various members.

The Decie Ranch Member (Figure 5) contains the greatest average of calcite abundance (76.4 wt.%) and least measured organics (0.7 wt.%). Additionally, this calcite-bearing member yields 0.7 wt.% ankerite/dolomite and 14.3 wt.% quartz. This in contrast with the overlying mudstone-dominated Poplar Tank Member, which is primarily comprised of quartz and clay-rich mudstone (Figure 5). Quartz is the greatest mineralogical contribution within this member at 41.2 wt.%. Illite/smectite/mica are the most abundant clay minerals (28.8 wt.%), whereas chlorite has

a minimal contribution at 2.1 wt.%. The calcareous mudstone and limestone produce an average of 14.6 wt.% calcite in this member. The Sullivan Peak Member (Figure 5) contains nearly equal mineralogical abundance of calcite (31.9 wt.%) and quartz (33.5 wt.%). In contrast to the other members, the Sullivan Peak Member yields the greatest average ankerite/dolomite (14.3 wt.%). Lastly, the Dugout Mountain Member, which directly overlies the Sullivan Peak Member, is compositionally similar to the shale and siltstone of the Poplar Tank Member. Quartz and clay abundance of the Dugout Mountain Member from FTIR measures at 48.8 wt.% and 28.7 wt.%, respectively (Figure 5). Average carbonate content of the Dugout Mountain Member is 7.9 wt.% calcite and 0.3 wt.% ankerite/dolomite. Compositional contribution from organics in this member is minimal (0.1 wt.%).

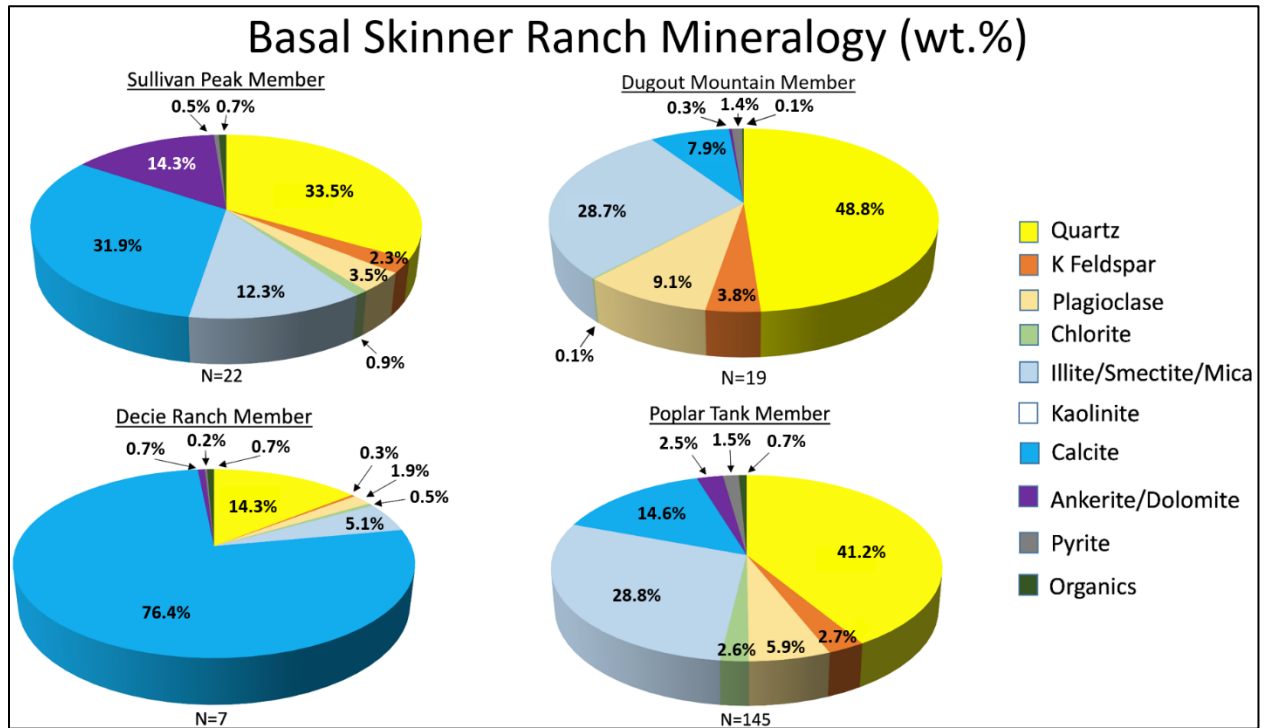


Figure 5. Average mineralogy of the Decie Ranch, Poplar Tank, and Sullivan Peak Members derived from Fourier transform infrared (FTIR) spectroscopy measurements.

Spectral Gamma Ray measurements were analyzed for K (wt.%), U (ppm), and Th (ppm) concentrations, specifically, to aid in clay mineralogy identification within the Poplar Tank Member. Two-hundred seventy-four (274) data points adequately contrast dominant clay composition across the three measured sections (Figure A3). Qualitative analysis indicates that Sections 8 and 8B clays are comprised primarily of illite, and mixed layer clays are common. The data spread of Section 10 makes it difficult to draw similar conclusions; however, the clays generally fall within smectite to illite compositional boundaries.

Linear relationships between Energy Dispersive X-Ray Fluorescence and Fourier transform infrared spectroscopy measurements were generated for gross lithologic comparison between members and sections. The stoichiometric checks indicate a positive correlation between the two methods, with aluminum oxide readings from ED-XRF and total clays from FTIR having the highest correlation coefficient of 0.95 (Figure 6). Calcium oxide and silicon oxide follow closely behind in comparison to calcite and quartz with R^2 values of 0.92 and 0.82, respectively (Figure 6). The stoichiometric checks provide the basis for further compositional evaluation, discussed in a later section within this paper.

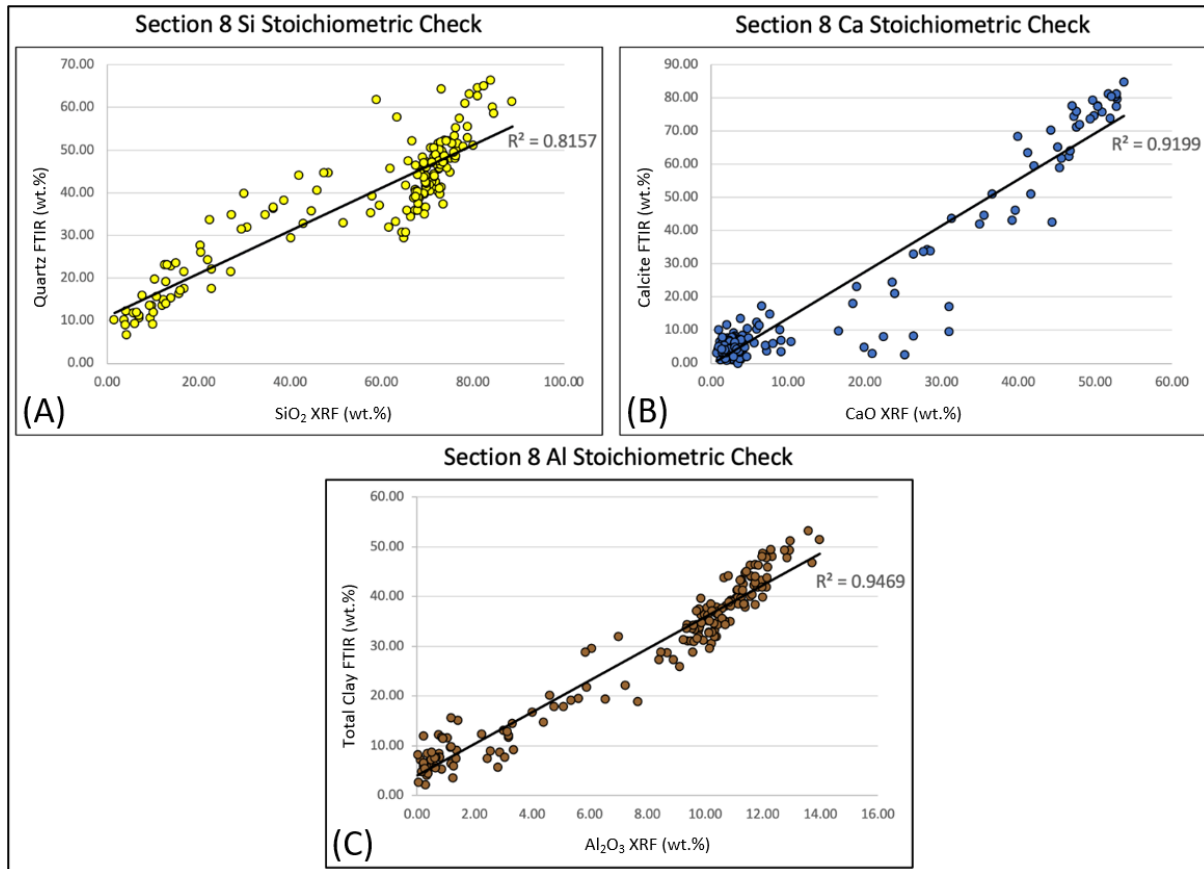


Figure 6. Linear relationship between FTIR and ED-XRF data establishing correlation between: (A) measured quartz (yellow); (B) calcite (blue); (C) and total clay (brown) minerals within Section 8.

4.1.2 Poplar Tank Facies

Five primary facies, termed Facies 1 to 5, were identified from hierarchical clustering of 648 Energy Dispersive X-Ray Fluorescence measurements. The facies succession was sub-divided based not only on geochemical characteristics, but also on micro-textures and sedimentary structures from petrographic analysis (Table 1). The carbonate-dominated chemofacies (Facies 1) was further divided into two textural subfacies, a coarse-grained Facies 1a and a fine-grained, Facies 1b. The five primary facies defined in this study are: (1a) Skeletal packstone/grainstone, (1b) Skeletal wackestone, (2) Calcareous silty mudstone, (3) Argillaceous shale/mudstone, (4) Siliceous mudstone/siltstone, and (5) Siliceous shale/siltstone. Locally, the siliceous-rich facies

(Facies 3-5) tend to outcrop in thicker beds (Figure 7), than that of carbonate-rich facies (Facies 1-2). A compositional organofacies comparison between our derived chemo/litho facies (Figure 8a) and organic matter type in the Skinner Ranch Formation is within the (Organofacies B) Siliceous Mudstone Class as defined by Donovan and others (2017). Additional interpretations of depositional environments are denoted in Table 1, as well as discussed in a later section. Further analysis of these basin-floor facies establishes a framework in which vertical and lateral heterogeneity within the Poplar Tank Member can be properly described.

	Facies 1a	Facies 1b	Facies 2	Facies 3	Facies 4	Facies 5
Defining Geochemical Characteristics	High Ca Low Si, Al, K Poor TOC	High Ca Low Si, Al, K Poor TOC	Moderate Ca, Si Low Al, K Good TOC	High Si, Al, Zr Low Ca Moderate to Poor TOC	High U, Ni, Si Low Mo, Ca Good TOC	High Si, Zr Low Al, Ca, U Poor TOC
Dominant Lithotype(s)	Skeletal Grainstone/Packstone	Skeletal Wackestone	Calcareous mudstone, massive and laminated calcareous siltstone	Argillaceous shale, massive silty mudstone	Siliceous shale and massive siltstone	Siliceous siltstone and shale
Grain Size	Mud to Gravel	Mud to very fine sand	Mud to very fine sand	Mud to coarse sand	Mud to very fine sand	Mud to very coarse sand
Sorting	Poor	Poor	Poor to well	Poor to moderate	Moderate to well	Poor to well
Sedimentary Structures	No observed grading, massive	No observed grading, massive	Laminations – lenticular, discontinuous; mostly massive	Laminations – lenticular, wavy, horizontal; loading structures; normal grading	Moderately laminated; bioturbation; mostly massive	Massive; faintly laminated
Grain Types	Crinoids, Bryozoans, Trilobites, Fusulinids, Brachiopods, Gastropods, Algae, quartz, phosphate, pyrite, calcite, chert	Calcareous sponge spicules, crinoids, brachiopods, lime mud, clay, quartz, organic matter	Calcite, quartz, clay, chlorite, organic matter, dolomite	Quartz, clay, organic matter	Quartz, calcite, clay, pyrite, organic matter	Quartz, clay, calcite, chert
Interpreted Depositional Setting	<u>Upper Depositional Slope:</u> medium- to thick bedded limestone between fairweather and storm wave base	<u>Depositional Slope:</u> thin bedded limestone below storm wave base	<u>Lower depositional slope/Basin:</u> distal portion of sedimentary gravity flow (dilute turbidites)	<u>Basin:</u> traction and suspension settling from waning turbidity flow	<u>Basin:</u> hemipelagic sedimentation and dilute turbidites	<u>Basin:</u> hemipelagic sedimentation and dilute turbidites

Table 1. Integrated geochemical and sedimentary characterization of facies based on clustering of normalized ED-XRF elements and petrographic thin section analysis.

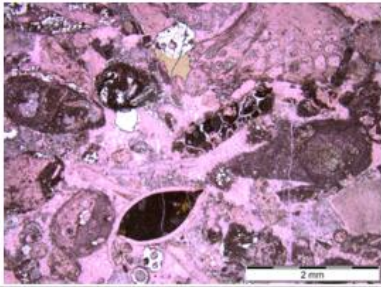
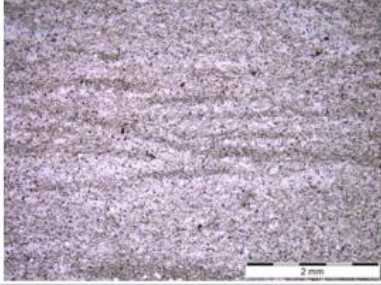
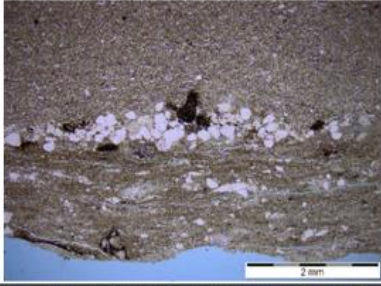
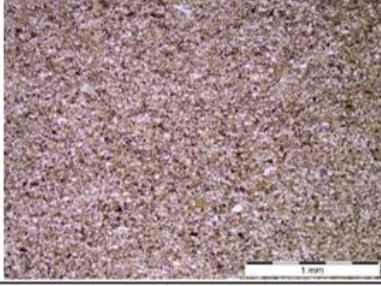
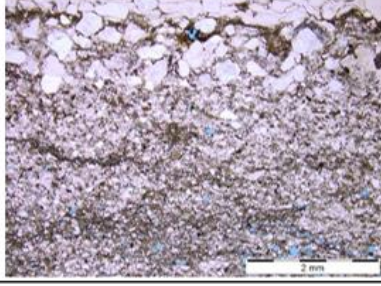
	Type Thin Section	Outcrop Representation
Facies 1		
Facies 2		
Facies 3		
Facies 4		
Facies 5		

Figure 7. Type thin section and outcrop representation of each respective facies.

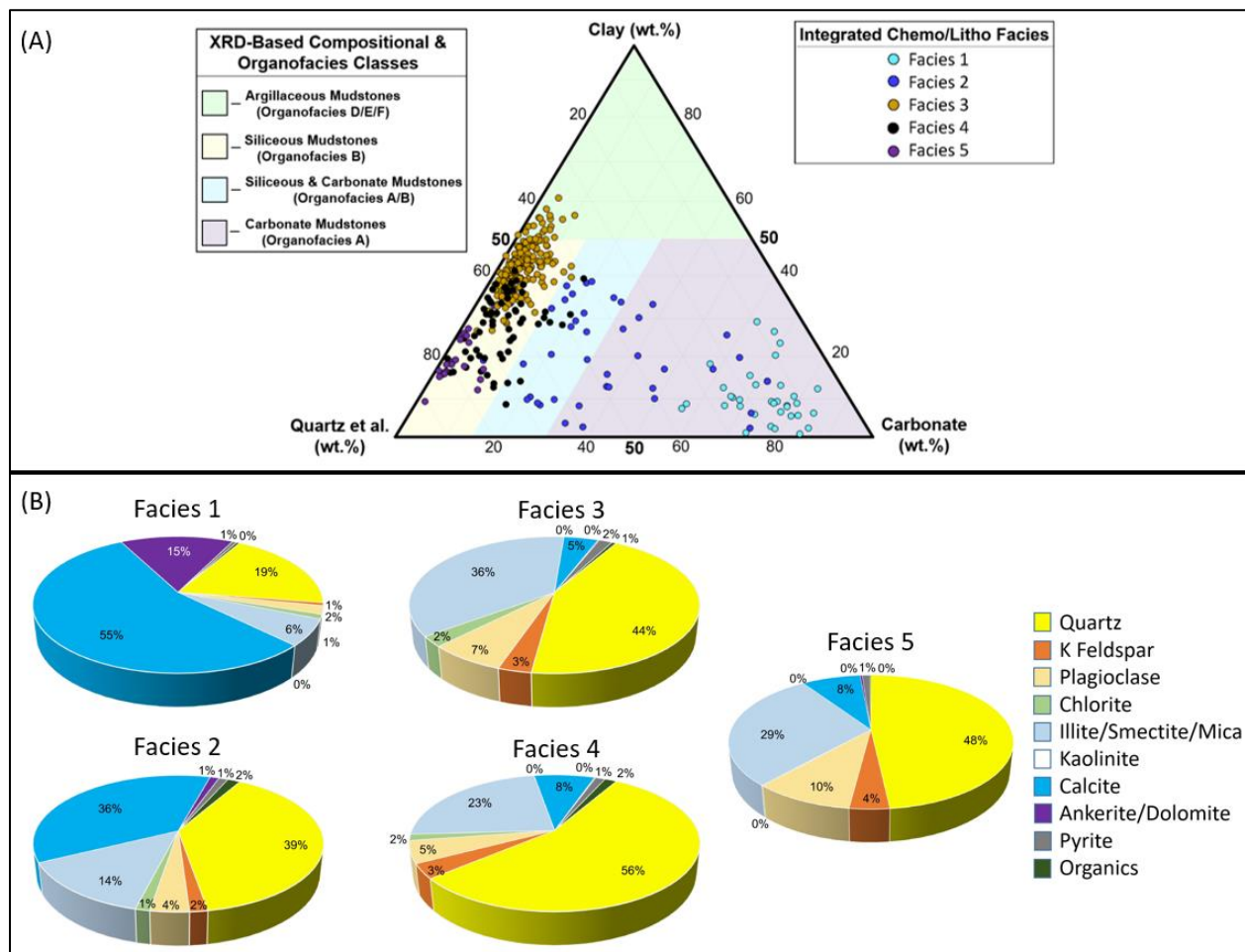


Figure 8. (A) Compositional distribution of mudstones based on XRD-based mudstone organofacies classification modified from Donovan et al., (2017). (B) Average mineralogy measured from FTIR.

4.1.2a Facies 1a (Skeletal Packstone/Grainstone)

The skeletal packstone/grainstone facies varies in color from light to dark gray. Grain sizes range from mud to gravel. Variations and nature of allochems lead the depositional units to comprise more than one lithofacies. Skeletal grainstone and packstone deposits typically contain intraclasts with skeletal grains. Additionally, the skeletal packstone lithofacies has a large diversity in marine fauna, including bioclasts such as gastropods, fusulinids, trilobites, crinoids, algae, brachiopods, bryzoans, and ostracods. Other constituents include limestone lithoclasts, chert

nodules, sandstone grains, siltstone grains, and phosphate grains. The skeletal grainstone and packstone deposits are grain supported with recrystallized micrite matrix; further reduction in porosity occurred due to later silica replacement. In both outcrop and thin section, this facies is massive with no observed grading. Within outcrop, this facies commonly has an erosional oscillatory base.

4.1.2b Facies 1b (Skeletal Wackestone)

The thin-bedded skeletal wackestone deposits are dark brown to black, with abundant fine-grained bioclasts of calcareous sponge spicules, which typically are aligned with bedding. Skeletal debris of crinoids and brachiopods is observed in thin section as well. Within outcrop, this facies is intercalated with intervals of thin- to thick-bedded skeletal packstone and grainstone. The matrix is predominantly comprised of pure lime mud, but also contains terrigenous clay and organic material. Organic matter is seen in thin sections as irregular black, discontinuous lenses (Figure A8). Angular to rounded detrital quartz grains occur in this facies but is more common in Facies 1a deposits. Similar to the skeletal packstone/grainstone facies, the skeletal wackestone deposits are massive. Additionally, there are no observed sedimentary structures indicating cohesive/fluidized flow. This facies is defined geochemically by containing high amounts of Ca and low concentrations of Si, Al, K, and TOC.

4.1.2c Facies 2 (Calcareous Silty Mudstone)

The calcareous silty mudstone facies is thin bedded, and ranges between light gray to tan in color, and is characterized as containing both massive and thinly interbedded laminae, and is comprised of sub-rounded, very-fine sand grains and silt sized particles. These coarser grains are dispersed between discontinuous, lenticular dark clay laminae (Figure 7). This facies contains

roughly equal parts Si and Ca, and relatively low quantities of clay minerals. FTIR measurements show this facies contains an average TOC of 1.7 wt.%, and in thin section, the organic matter occurs as thin black seams.

4.1.2d Facies 3 (Argillaceous Shale/Mudstone)

The argillaceous shale and mudstone facies of the Poplar Tank Member are medium to thick bedded locally and is the most volumetrically abundant facies in the study area. This facies commonly overlies the limestone deposits of Facies 1 and is interbedded with the mudstone and siltstone beds of Facies 4. These deposits are light to dark brown and vary in grain size (mud to coarse sand) and sorting (poor to moderate). Compositionally, this facies is distinguished between the other facies by its high clay content with average ED-XRF readings of 10.6 wt.% Al and 2.8 wt.% K. Average TOC for facies 3 is 0.9 wt.%. Laminae are rich in argillaceous grains and occur as lenticular, wavy, and horizontal. In some areas, silt to very-fine sand grade into overlying clay laminae. Compaction or loading structures are rare where overlying silt grains penetrate underlying clay/mud.

4.1.2e Facies 4 (Siliceous Mudstone/Siltstone)

The siliceous mudstone/siltstone facies outcrops as thin to medium thick beds of moderately laminated shale and massive siltstone. The laminae of the shale typically grade from silt to finer clay grains. In outcrop, this facies is fissile, breaking along bedding planes. Identification of structures within outcrops vary depending on quality of exposure. Bioturbation in thin sections show lenses of silt grains infilling downward. The siltstone beds of this facies tend to be massive and light to medium gray in outcrop. In some areas, there are gradational contacts with the under or overlying clay-dominated shale beds of Facies 4, but other exposures show sharp

contacts between this facies and that of the carbonate-rich limestone deposits. Sub-angular to rounded silt-size quartz grains are prominently dispersed within a brown clay matrix. ED-XRF analysis shows that this facies has high concentrations of Si, Ni, and U, and low Ca concentrations. TOC values in this facies range as high as 2.8 wt.%.

4.1.2f Facies 5 (Siliceous Shale/Siltstone)

The siliceous shale/siltstone facies that comprise the lower Dugout Mountain Member outcrops as orange to yellow-colored strata of varying thin to medium thick beds. Similar to Facies 4, the shale in this facies tends to be platy and fissile. This facies weathers pink, red, and purple and commonly has Liesegang rings or banding. Contacts are sharp between the interbedded siltstone and shale and are rarely capped by beds of pebble conglomerate. Analysis from thin sections show that this facies is comprised of sub-angular to sub-rounded silt-sized quartz grains. In some areas, dark argillaceous laminae are dispersed between silt grains, however, this facies is commonly massive and lacks sedimentary structures.

Geochemically, the bulk composition of Facies 5 is similar to that of Facies 4, however, TOC abundance is considerably less with an average value of 0.1 wt.% (Figure 8B). Average quartz and clay (illite/smectite/mica) measure at 48.8 wt.% and 28.7 wt.%, respectively. The partitioning index ranking elemental importance from ED-XRF measurements illustrate that this facies is distinguished by high amounts of detrital elements (Zr, Th, and V), as well as low concentrations of elements (Ni and U) associated with bioproductivity (Figure A2).

4.2 Elemental Distribution and Proxies

SGR and ED-XRF measurements were analyzed to determine the depositional record of the rocks of the Poplar Tank Member. Controls include changes in provenance, paleoredox, and

bioproductivity/paleoproductivity. Elements and elemental ratios plotted for chemostratigraphy include: silicon (Si), aluminum (Al), potassium (K), zirconium (Zr), zirconium/thorium (Zr/Th), and silicon/zirconium (Si/Zr) (Clastic/Terrigenous/Detrital Proxies); molybdenum (Mo), vanadium/ vanadium+nickel (V/V+Ni), vanadium/chromium (V/Cr), and uranium/thorium (U/Th) (Paleoredox proxies); and chromium (Cr), nickel (Ni), and uranium (U) (bioproductivity proxies). The elements and their respective proxies are also outlined in Table 2.

Element	Proxy	References
Al	Clay, Feldspar, and Terrigenous Input	Tribovillard et al., 2006; Sano et al., 2013
K	Clay, Feldspar, and Terrigenous Input	Tribovillard et al., 2006; Driskill et al., 2018; Pearce and Jarvis, 1992; Nance and Rowe, 2015
Si	Quartz	Pearce and Jarvis, 1992; Martin et al., 2013
Ca	Carbonate source and phosphate	Tribovillard et al., 2006; Nance and Rowe, 2015; Turner et al., 2016; Driskill et al., 2018
Zr	Continental/Terrigenous source	Bhatia and Crook, 1986; Mu et al., 2013; Turner et al., 2016
Zr/Th	Continental/Terrigenous source	Ratcliffe et al., 2006
Si/Zr	Authigenic/Biogenic vs. Detrital Silica	Sageman and Lyons, 2003; Ratcliffe et al., 2012; Driskill et al., 2018
Ni	Bioproductivity, OM accumulation	Tribovillard et al., 2006; Driskill et al., 2018
Cr	Bioproductivity with siliciclastic	Driskill et al., 2018
U	Redox sensitive, OM accumulation	Tribovillard et al., 2006; Algeo and Rowe, 2012; Ratcliffe et al., 2012; Driskill et al., 2018
Mo	Bottom water euxinia, redox sensitive	Tribovillard et al., 2006; Algeo and Rowe, 2012; Ratcliffe et al., 2012; Turner et al., 2016; Driskill et al., 2018
V/Cr	Bottom water anoxia, redox sensitive	Jones and Manning, 1993
V/(V+Ni)	Bottom water anoxia, redox sensitive	Driskill et al., 2018
U/Th	Bottom water anoxia, redox sensitive	Jones and Manning, 1993

Table 2. List of elements/elemental ratios and their interpreted proxies.

For paleoredox interpretations of each facies, we averaged Mo, V/ V+Ni, V/Cr, and U/Th values from the three measured sections (Figures 9a and 9b). For Mo and V/V+Ni, Facies 5 records the greatest averages at 5.3 ppm and 0.7, respectively. Average V/Cr is greatest in Facies 1 at 2.3

(Figures 9, A4, A5). Likewise, Facies 3 and 4 record similar averages of 0.9. Average U/Th data shows that the carbonate-rich facies (Facies 1 and 2) have the greatest values of 1.2 and 1.3, respectively. Bioproductivity proxies Cr and Ni are established in linear regressions compared to TOC (Peavey et al., in prep). Plotted correlation coefficients for Cr is 0.7 and 0.5 for Ni. Both U/Th and Ni distributions increase around the maximum flooding surface (Figures 9a and 10). Figures A6 and A7 show similar increases in paleoproductivity proxy values of U and Cr at the maximum flooding surface.

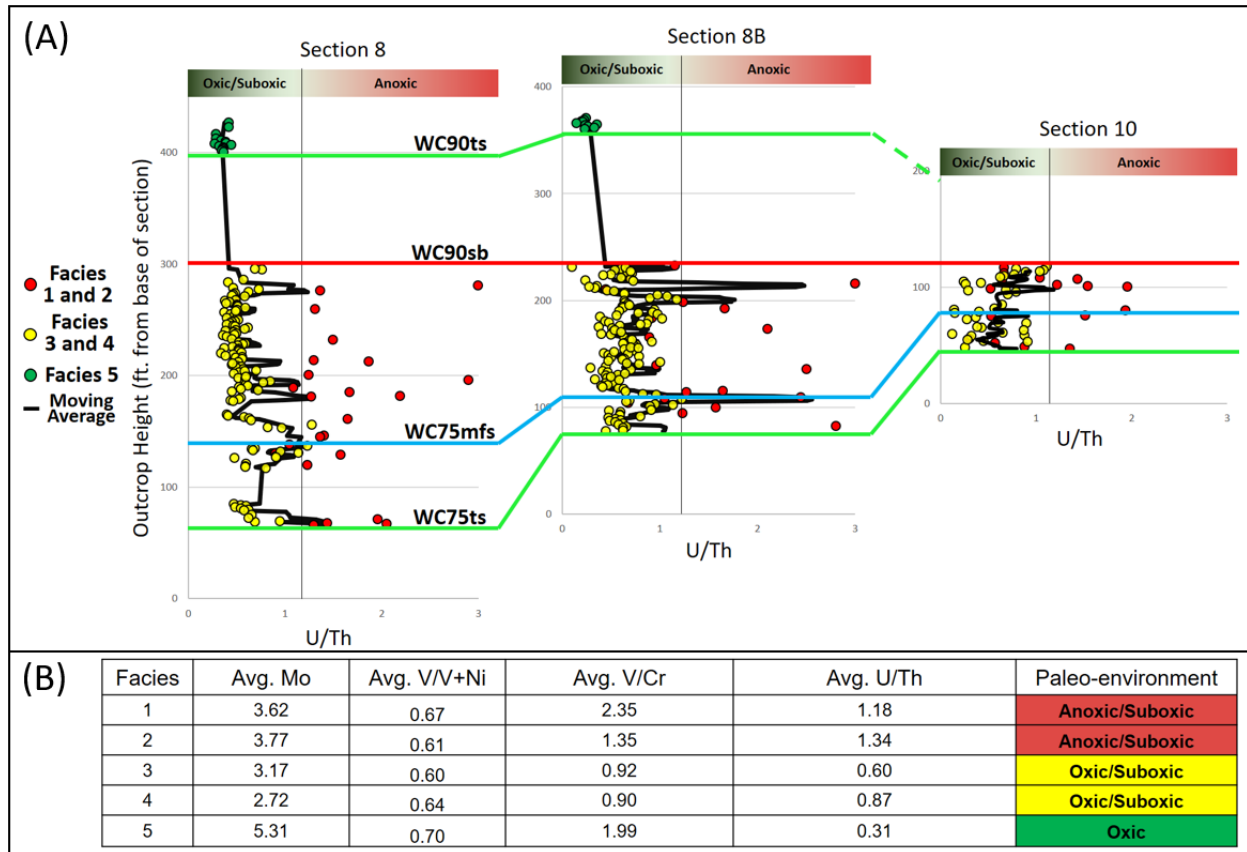


Figure 9. (A) Paleoredox through time at each measured section is illustrated and denoted by elemental distribution of U/Th values. Anoxic/suboxic conditions (Facies 1 and 2, red color), oxic/suboxic (Facies 3 and 4, yellow color), oxic (Facies 5, dark green color). Sequence stratigraphic interpretations denoted by the transgressive surface (WC75ts and WC90ts – green line), maximum flooding surface (WC75mfs – blue line), and sequence boundary (WC90sb – red line). (B) Average values of paleoredox proxies and interpreted redox conditions of the paleo-environment denoted in table.

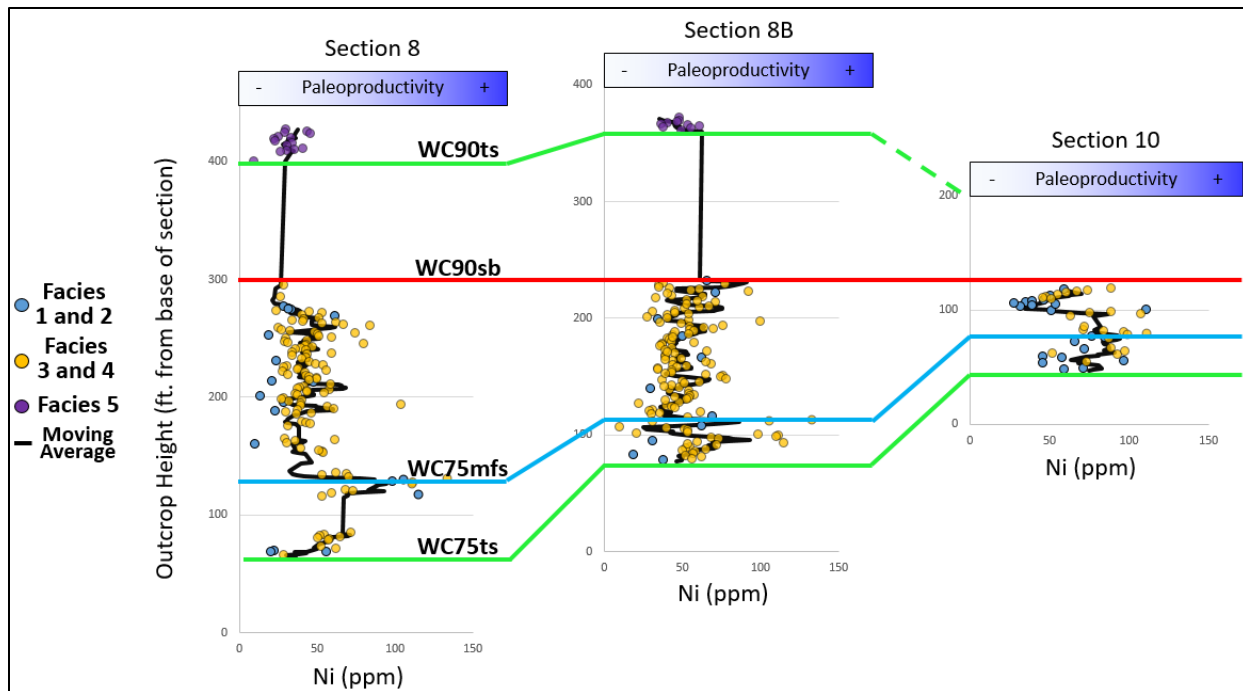


Figure 10. Paleoproductivity/bioproductivity illustrated by measured values of nickel (Ni), colored by Facies representation at each measured section. Sequence stratigraphic interpretations denoted by the transgressive surface (WC75ts and WC90ts – green line), maximum flooding surface (WC75mfs – blue line), and sequence boundary (WC90sb – red line). Increase in nickel values indicate zones with higher TOC content, as seen around the WC75mfs. Average value of nickel trends higher moving each section to the right, interpreted as greater organic accumulation.

Cross-plotting Si with Zr on a per facies basis suggests a positive correlation between the two elements within Facies 2 and 5 (Figure 11). By these methods, we determine that the silica within these facies are of detrital origin (Driskill et al., 2018; Wilson et al., 2020). Inversely, Facies 3 and 4 silica is negatively correlated to zirconium, which suggests an authigenic/biogenic source (Figure 11). Facies 1 does not have a significant observable trend. Additional qualitative analysis of the terrigenous/detrital proxies was performed to record stratigraphic variations throughout our transgressive systems tract and highstand systems tract within our depositional sequence. This is discussed in further detail in a later section.

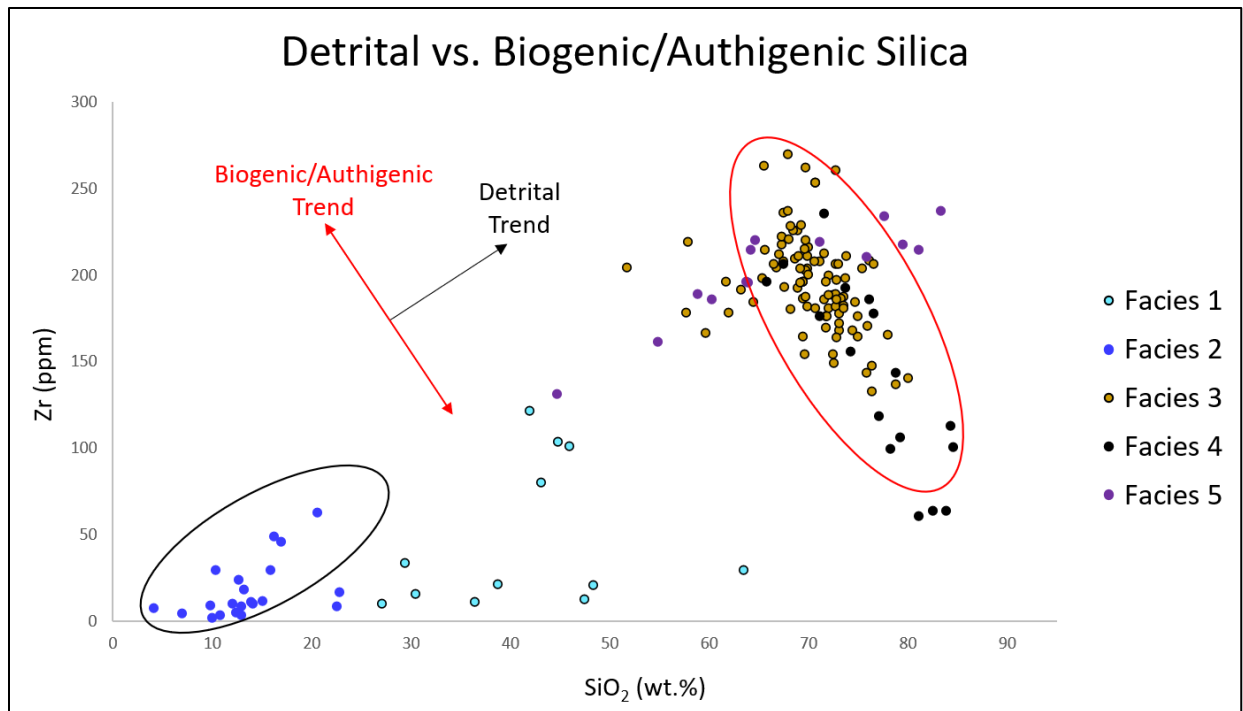


Figure 11. Cross plot of ED-XRF measured silica (SiO₂) Zr at Section 8. Detrital silica trend shown in black. Biogenic/authigenic silica trend shown in red. Data points are colored by their respective facies. Facies 1 does not show a correlation. Facies 2 and 5 have a detrital silica trend. Facies 3 and 4 trend along with biogenic/authigenic silica.

4.3 Vertical and Lateral Distribution and Depositional Architecture

Seismic-scale geometries observed from outcrop photography aid in the deduction of the depositional history between the three members. Within our digital drone model of the Lenox Hills, we delineate unconformities at the base of the Decie Ranch and Sullivan Peak members (Figure 12). These two members appear to contain more resistant beds in outcrop, as opposed to the mixed carbonate-siliciclastic deposition of the shale, mudstone, and limestone beds within the Poplar Tank Member, which is poorly exposed due to its finer grain size and increased weathering. Analysis of the integrated facies within the three measured sections and the digital drone model show a laterally discontinuous Poplar Tank deposition. Thickness of this member ranges between 88 ft.-245 ft., and is greatest at the type section (Hill 5300) before it decreases Northeast until eventually lapping out onto the underlying Decie Ranch Member at Hill 5021, where the Decie

Ranch Member and Sullivan Peak Member are in contact (Figures 12 and A12). Architecture of the basinal contact is shaped by the discontinuous geometry of the underlying carbonate-rich conglomerate beds of the Decie Ranch Member (Figure 12). Likewise, the top contact is undulatory, where the overlying sediments of the Sullivan Peak Member truncate the top of the Poplar Tank Member, defining the unconformity.

Distribution of the facies varies between the measured sections (Figure 13). Facies 1 and 2, the carbonate-rich facies, increase in deposition from Section 8 (15% and 7%) to Section 10 (23% and 10%). This is at the expense of the argillaceous shale/mudstone facies, which decreases in deposition from the southwest (66%) to northeast (45%). Facies 4, the siliceous mudstone/siltstone facies, generally increases from Section 8 (12%) to Section 10 (22%).

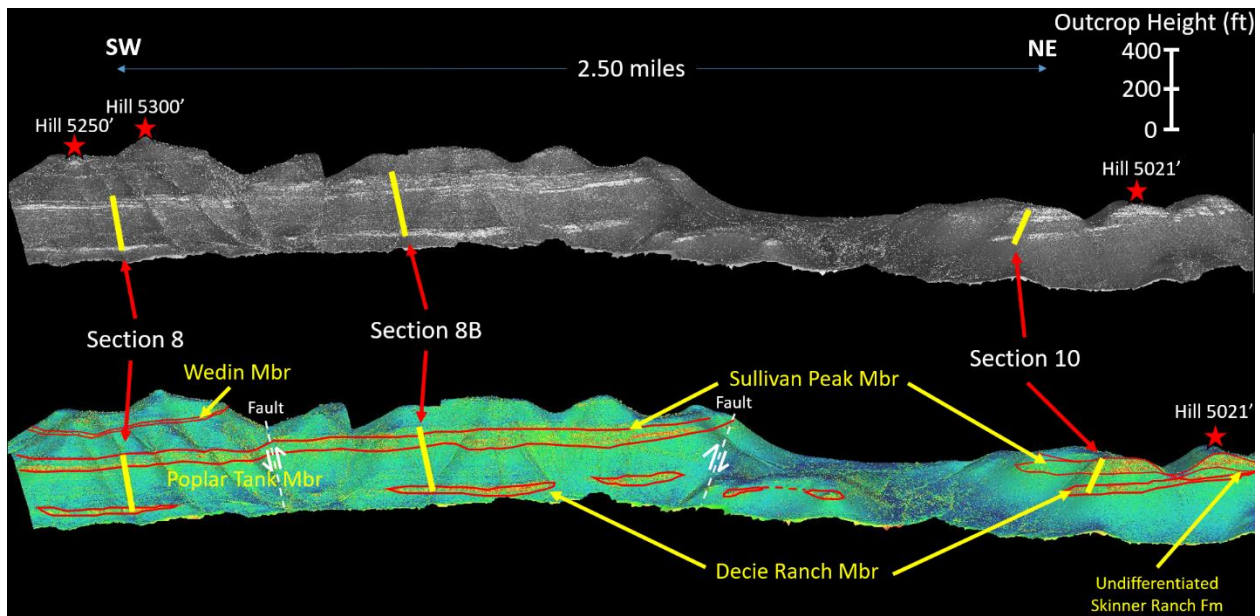


Figure 12. Gray-scaled (top) and ultra-violet light (bottom) of the digital outcrop model (DOM) of the Lenox Hills. Measured section locality illustrated in yellow. Depositional architecture is detailed in the red outline of the exposed members, which was captured by roughly 2.5 miles of collected drone photogrammetry. Interpreted faults are shown in white, along with direction of fault displacement.

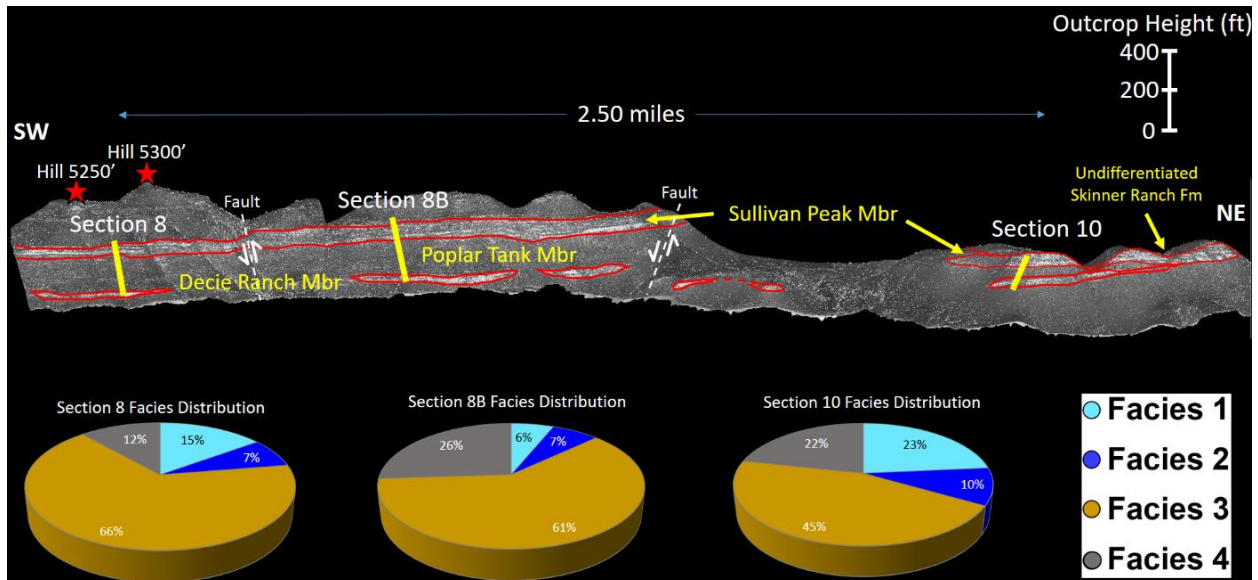


Figure 13. Gray-scaled digital outcrop model (DOM) of the Lenox Hills. Locality of sections and members are denoted in yellow. Geometries of the Decie Ranch and Sullivan Peak members are outlined in red. Quantitative vertical distribution of facies abundance at each measured section is illustrated by the associated pie charts. Facies 1 and 4 distributions vary between sections. Facies 2 increases from the southwest to northeast. Inversely, distribution of facies 3 decreases from southwest to northeast. Facies 5 not shown because its total thickness is not determined.

5 DISCUSSION

5.1 Chemo/Sequence Stratigraphy and Depositional Model

Reconstruction of the depositional history of the mixed carbonate-siliciclastic system of the Upper Wolfcamp Formation is facilitated by geobody architecture of the facies, integrated with geochemical process of the paleoenvironment. Figure 14 summarizes the depositional evolution associated within the reciprocal sedimentation model for the Upper Wolfcamp Formation. Chemo - and sequence stratigraphic interpretations of the Upper Wolfcamp Formation are determined on the distribution and trends of the facies, total gamma ray values, and elemental proxies (Figure 15).

5.1.1 Depositional Model

Geochemical and sedimentary analysis shows evidence of anoxic/suboxic to oxic conditions during Upper Wolfcamp Formation deposition. The presence of shallow marine fauna, phosphate nodules, and high redox proxy values of the mudstone interbedded with skeletal packstone/grainstone strata (Figure 14a) suggests deposition along an overall anoxic/suboxic depositional slope, primarily during the late highstand, when there is a change to a carbonate dominated shelf. The sharp erosional/oscillatory basal contact of the beds containing Facies 1a, combined with the lack of observed grading and other sedimentary structures, suggests reworked storm-event deposits of relatively shallow marine limestone beds along an upper depositional slope. Likewise, the lack of observed sedimentary features and high redox indicate an anoxic/suboxic setting of undisturbed sedimentation of skeletal wackestone. This facies is commonly interbedded with argillaceous shale/mudstone, calcareous siltstone, and infrequent storm event deposits of bioclastic (skeletal) packstone/grainstone. The skeletal wackestone of

Facies 1b are more abundant in mud/clay grains and lack both grading and structure, indicating a lower energy depositional environment, likely along a depositional slope below the storm wave base. Late highstand deposition of carbonate-rich strata to the basin likely was coincident with maximum carbonate production (Schlager et al., 1994). We interpret that dilution of the carbonate facies occurs within the early highstand where hemipelagic sedimentation of siliciclastic beds and bedsets are more prominent (Figures 13 and 14a). We interpret that siliceous mudstone and siltstone beds (Facies 4) represent hemipelagic sedimentation on the sea floor, as well as along the lower and middle depositional slope, punctuated by intermittent deposition of Facies 1-3. Argillaceous shale and mudstone are comprised of terrigenous/detrital siliciclastic grains (Figure 11). Deposition of these mudstone are attributed to traction and suspension settling from waning turbidity flows (Schieber et al., 2010; Kvale et al., 2019; Wilson et al., 2020). Soft sediment deformation and discontinuous laminae observed in thin section suggest deposition as a result of rapid loading of sandy turbidites onto unconsolidated clay-rich sediment. Furthermore, textural constituents, terrigenous matrices, and general lack of sedimentary structures of the fissile, clay shale suggests normal marine hemipelagic deposition prior to turbidity disturbance. Minor organic matter content and presence of silty lenses suggests oxygenated conditions reworked by bottom currents. TOC is greatest in the siliceous mudstone/siltstone associated with slow accumulation and preservation of marine organic matter (Organofacies B) during suboxic to oxic conditions.

Lastly, limestone and mixed limestone/siliciclastic conglomerate deposition records lowstand shedding of mass-transport deposits caused by nearby slope and shelf margin failure, resulting in fauna-rich, massive, cohesive debris flows (Figure 14b). Mudstone lithoclasts at the base of the deposits indicate rapid transport and mixing of unconsolidated sediment from erosion of underlying shale within the HST. Within the LST of the Sullivan Peak Member of the Upper

Wolfcamp Formation, an increase in silica, bedding thickness, as well as continuous sheet-like geometry from a point source indicates a mixed carbonate-siliciclastic fan dominated by sediment gravity flows (Kvale et al., 2019). In some areas of the Sullivan Peak Member, carbonate debris flows are similar to those of the LST at the base of the Upper Wolfcamp Formation (Decie Ranch Member), which is characteristically different, and discussed in a later section. In other areas, hybrid event beds of linked debrites underlie normal-graded bedded sandstone (Kvale et al., 2019).

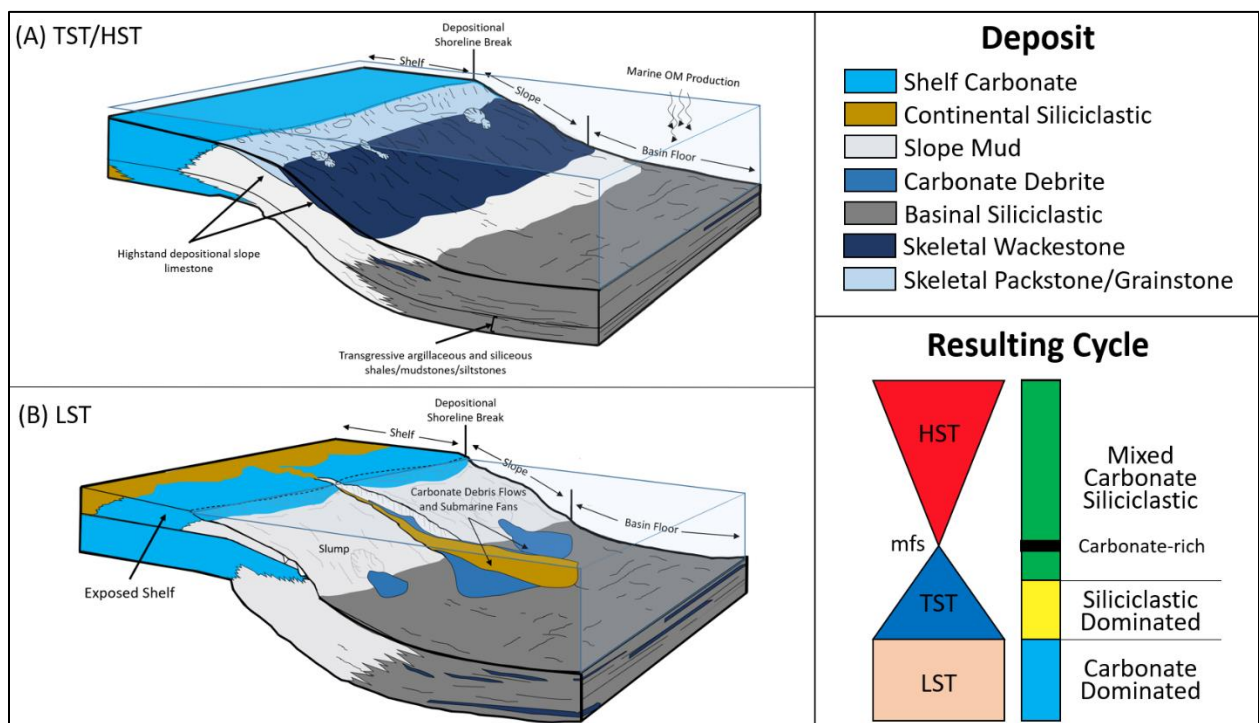


Figure 14. Interpreted depositional model of the Lower Member (Decie Ranch and Poplar Tank members) of the Upper Wolfcamp Formation. Dominant lithotypes throughout the depositional sequence are illustrated in the lower right box. Modified from Li et al., (2015).

5.1.2 Lowstand Systems Tract (LST)

Two sequence boundaries, one at the base of the Decie Ranch Member (Wc75sb), and one at the base of the Sullivan Peak Member (Wc90sb), are interpreted at the base of these limestone-rich conglomerate zones. These interpreted sequence boundaries coincide (Figures 15, A10, A11)

with a decrease in total gamma ray, as well as erosion or non-deposition of overlying mudstone due to limestone conglomerate deposition, which we interpret as the onset of our LST. The LST caps an upward increase in the detrital proxies Zr and Zr/Th that occurs in the underlying HST, which reflect an increased proximity to a siliciclastic source during a basinward shift in facies and prograding continental strata. In outcrop, LST deposition is observed as an abrupt change in depositional facies separated by an erosional, undulatory base, which we interpret as a sequence boundary. This sharp contact occurs at the base of the conglomerate in both the Sullivan Peak and Decie Ranch members. Scouring at the base of the carbonate-rich gravity flows is indicated by shale lithoclasts near its base that was brought by basinward transport of shelf margin and slope shedding (Ross and Ross, 2003). Carbonate beds (skeletal packstone, grainstone) and limestone boulder conglomerate beds are observed in the Decie Ranch Member LST. Similarly, the Sullivan Peak Member is conglomerate-rich but comprised more commonly with mixed carbonate/siliciclastic beds interpreted as LST mass transport deposits.

5.1.3 Transgressive Systems Tract (TST)

The onset of argillaceous and siliceous mudstone/shale deposition, in concurrence with a spike in the total SGR values is interpreted as the transgressive surface (Figures 15, A10, A11), which we denote as Wc75ts and Wc90ts. The Transgressive Systems Tract (TST), bounded by the transgressive surface and maximum flooding surface, is marked by a general increase in gamma ray values. Terrigenous and detrital proxies (Al, K, Zr, Zr/Th) decrease as sea level increased, indicating a shift of deposition from the paleo-shelf to more distal siliciclastic sediment sources. Widespread basinal depositions of siliciclastic dominated Facies 3 and 4 occur most frequently within the TST and are interpreted as turbidites and event bed packages. Previous studies of the Wolfcamp A interval elsewhere in the Permian Basin (Ward, 2013;

Baumgardner, 2014; Driskill et al., 2018; Bievenour and Sonnenberg, 2019; Colborne et al., 2019) have shown similar observations and made similar interpretations. The top of the TST is marked by the occurrence of calcareous siltstone, mudstone, and limestone deposition at and around the maximum flooding surface (mfs). This is expressed as discrete fluctuation of carbonate-prone Facies 1 and 2, as well as localized highs in the redox-sensitive proxies Mo, U/Th, and V/Cr. We denote this as Wc75mfs within our cross sections, and it is interpreted to mark the most distal marine deposition within the Wolfcamp A Formation. The high SGR values reflect increases in uranium caused by organic-rich mudrock successions (Figures 15, A10, A11). This coincides with spikes of biogenic/authigenic silica (Si/Zr) during carbonate Facies 1 and 2 deposition.

5.1.4 Highstand Systems Tract (HST)

Deposition of siliciclastic prone facies is intermittently disturbed by carbonate siltstone, mudstone, and limestone within the early Highstand Systems Tract (HST). The shift from a mixed carbonate siliciclastic shelf to a carbonate dominated shelf reflect more more frequent carbonate-prone facies successions within the Poplar Tank Member comprise the late Highstand Systems Tract (HST). Bounded below by the Wc75mfs, there is an overall decrease in total SGR values and siliciclastic input. Detrital/Terrigenous proxies Al, K, Zr, Zr/Th increase, whereas redox-sensitive proxies decrease within the HST. Those simultaneous changes reflect depositional environment shift from distally sourced terrigenous clastic and anoxic deposition during sea level rise, to more proximal facies as sea level fell. Coarse-grained sedimentation of Facies 1a, 2, and 4 dominate the generally thicker packages within the upper half of the HST, likely during a period of a slower sea level rise, when strata was derived from shallow marine carbonate, and a shift to a carbonate dominated shelf.

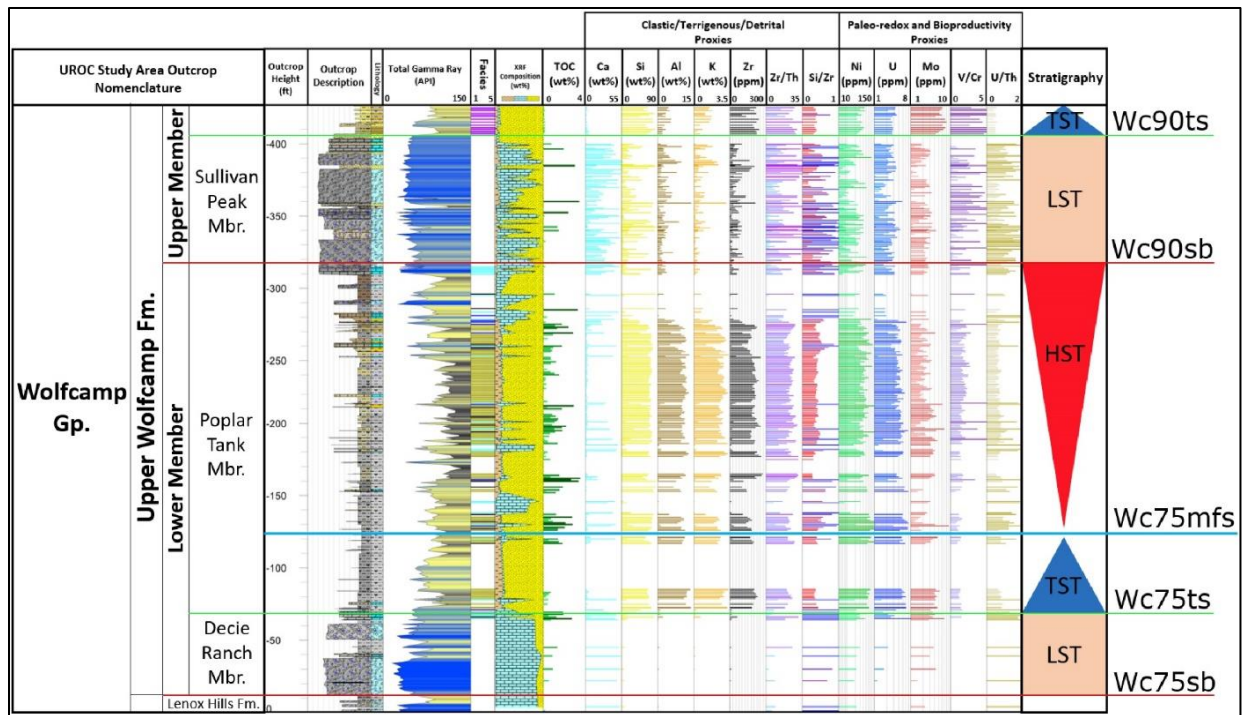


Figure 15. Elemental distribution, outcrop description, total gamma ray, and facies of Section 8. Sequence boundary (red), transgressive surface (green), and maximum flooding surface (blue) based on observed outcrop sedimentology, total gamma ray, and chemostratigraphic proxies.

5.2 Geochemistry

5.2.1 Upper Wolfcamp Formation

The bulk geochemistry of the Upper Wolfcamp Formation outcrop records distinct changes in mineralogy and paleoenvironment of the sediment deposited within the North American Wolfcampian and Leonardian stages. Stark differences in conglomerate composition, specifically the increase in silica content within the Sullivan Peak Member indicates a higher influx of detrital silica and suggests sea level was lowered, allowing increased siliciclastic input. The conglomerate within the Decie Ranch Member lacks silica, possibly due to a difference in sediment sourcing from a nearby carbonate platform, less accommodation, and a more humid environment, per similar depositional analogs (e.g., Tabor et al., 2008; Li et al., 2015; Zeller et al., 2015; Kvale et al., 2019). Another possible explanation is an alleviation in basin subsidence and rapid sea level

rise that moved the supply of siliciclastic grains landward throughout the North American Wolfcampian Stage, thus leading to carbonate-rich deposition. A change from a humid to arid depositional environment, as well as sediment source occurred during transitional icehouse-greenhouse climatic conditions (Gastaldo et al., 1996; Tabor et al., 2008; Ward, 2013; Ruppel, 2019). Some interpret the initiation of Leonardian deposition within the Permian Basin to be coincident with sedimentation of shallow marine, tidal-flat facies comprised of sandstone, anhydritic shale, bedded evaporites, and dolomite (Silver and Todd, 1969; Mazzullo and Reid, 1989; Fitchen, 1997; Kerans et al., 2000). Our observations of the Skinner Ranch members within our study area do not show such depositional facies.

5.2.2 Upper Wolfcamp Group Mudstone

Major and trace elements, such as Si, Al, K, Th, and Zr are reliable indicators of siliciclastic and/or detrital input. Th-K cross plots demonstrate a dominant mixed-layer illite clay-type for the mudstone within the Upper Wolfcamp Formation. Additionally, a strong linear relationship between ED-XRF measured aluminum and total clays from FTIR show that aluminum is adequate in representing bulk clay abundance. A similar interpretation is made for the silica fraction based on its correlation to the quartz measured from FTIR (Figure 6). The ED-XRF derived bulk compositional profile, as well as average mineralogical abundance from FTIR of the mudstone reveal that they are quartz-dominated. Inversely correlated Si and Zr indicate that the bulk of silica within the Upper Wolfcamp are primarily of biogenic and/or authigenic origin. Similar observations were made based on core studies within the Delaware Basin (Nance and Rowe, 2015; Ratcliffe et al., 2015; Driskill et al., 2018; Peavey et al., 2022).

TOC comparison between carbonate and siliciclastic beds within the Upper Wolfcamp Formation are comparable and demonstrate that bulk composition does not coincide with organic richness. Instead, major/trace elements and ratios such as Ni, U, Cr, Mo, V/Cr, and U/Th associated with bioproductivity and redox-sensitive proxies indicate a greater propensity for organic matter preservation. Ni and Cr are soluble in oxygenated surface waters, and act as micronutrients for microbial marine organisms (Tribovillard et al., 2006). Wolfcamp A studies indicate Ni, Cr, and U are strongly correlated to TOC (Meyers, 1994; Tribovillard et al., 2006; Algeo and Rowe, 2012; Mu et al., 2013; Sano et al., 2013; Baumgardner et al., 2014; Ratcliffe et al., 2015; Driskill et al., 2018). The partitioning index of our facies quantitatively supports the link between these elements and TOC. The mudstone, shale, and siltstone beds with the greatest TOC in the Upper Wolfcamp Formation coincide with relatively higher amounts of Ni, U, and Mo.

5.3 Wolfcamp A Delineation: Outcrop to Subsurface Correlation

Geochemistry of the Upper Wolfcamp Formation in the Lenox Hills outcrops provide a vertical succession to compare and delineate the North American Wolfcampian and Leonardian depositional boundary. Gross lithological variations, as well as organic composition of the fine-grained strata within the Upper Wolfcamp Formation denote a shift from organic-rich, mixed carbonate-siliciclastic sedimentation of the Poplar Tank Member to the poor TOC, silica-dominated shale/siltstone beds of the basal Dugout Mountain Member. Similar trends occur within the subsurface between the Wolfcamp A and X,Y, and Z Sands (Driskill et al., 2018). Other petrophysical parameters were used to define this boundary within core and other subsurface data, however the outcrop boundary is more difficult to determine. Within the outcrops, we place the Base Leonardian Unconformity at the base of the Wedin Member based on our observations in

depositional facies evolution. Furthermore, biostratigraphic and sequence stratigraphic relationships aid in confining the depositional age of the Skinner Ranch Formation. This interpretation designates the Upper Wolfcamp Formation in the Glass Mountains within the North American Wolfcampian Stage, as coeval to the Wolfcamp A Formation in the subsurface of the Delaware Basin (Nance and Rowe, 2015; EIA, 2020; Richards et al., 2022; Peavey et al., 2022). This placement agrees with the basinal Skinner Ranch Formation being Wolfcampian (Cooper and Grant, 1964, 1966, 1972, 1973). An added complexity is the correlation of the shale/mudstone beds within the Dugout Mountain Member that overlie the Sullivan Peak Member southeast of the Lenox Hills. Lack of accessibility means we were not able to sample and characterize this member at its type locality. Based on our interpretations, we hypothesize that the Dugout Mountain Member also is Wolfcampian.

5.4 Implications for Reservoir Heterogeneity

Understanding the mechanisms governing the changes in the mixed depositional system is of key importance in evaluating and understanding facies and reservoir heterogeneity of the Upper Wolfcamp (Wolfcamp A) Formation. In the context of petroleum exploration, Facies 2 (calcareous silty mudstone) and Facies 4 (siliceous mudstone/siltstone) yield the highest TOC (Figure A9) and are more commonly preserved northeast in the study area, at and around the Upper Wolfcamp maximum flooding surface (Wc75mfs). Chemostratigraphic methods indicate that these hydrocarbon-bearing units could possibly act as source beds due to their potential for accumulating and preserving organic matter. Dolomitized carbonate are principal hydrocarbon reservoirs in the Wolfcampian and Lower Leonardian (Lucia and Ruppel, 1996; Caf and Pigott, 2021); however, in our study area organic accumulation within these facies (Facies 1) is

minimal. Due to its high clay content and volumetric significance, Facies 3 (argillaceous shale/mudstone) may act as a geomechanical barrier inhibiting fracture propagation and development (Evenick, 2016; Donovan et al., 2017). Carbonate dominated successions within the TST may have a greater propensity for fracture maturation and connectivity of vertically stacked reservoirs.

6 FUTURE WORK

Additional sedimentology studies are needed on the conglomerate beds of the Upper Wolfcamp Formation (Decie Ranch and Sullivan Peak members) in order to provide an improved understanding of their compositional and textural differences to their specific depositional setting. Furthermore, coupling this with high-resolution drone photogrammetry could provide insights in the evolution of the bedding architecture throughout LST deposition during the Late Wolfcampian. Further analysis is needed to evaluate diagenetic constraints affecting the permeability and porosity between these facies to better understand hydrocarbon retention and migratory pathways within these source and tight-rock systems. Chemostratigraphic studies in the shale and siltstone of the Dugout Mountain Member, which overlies the Sullivan Peak Member and comprise the HST and TST of the second depositional sequence within the Upper Wolfcamp Formation are necessary. Depositional controls concurrent with carbonate siliciclastic deposition should be further explored to improve upon the understanding of the sourcing of siliciclastic sediment that accumulate beyond the carbonate zone. Although there were recent studies on the Upper Wolfcampian slope facies (Skinner Ranch Formation) at its type locality further northeast of the Lenox Hills (Janson et al., 2017), there is a need to improve upon this analysis by integrating the chemostratigraphic findings of this study which emphasizes the deposits at the basin and slope margin. Lastly, we encourage U-Pb dating of bentonite samples within the Poplar Tank Member to more accurately constrain the age and rate of deposition within the Upper Wolfcamp Formation. Additionally, integrating these methods should provide a more robust subsurface correlation for future regional studies.

7 CONCLUSIONS

The Upper Wolfcamp Formation was identified within outcrop at the Lenox Hills by its bulk mineralogical and depositional characteristics, as a mixed carbonate-siliciclastic depositional system. The conglomerate beds of the Upper Wolfcamp (Decie Ranch and Sullivan Peak members) are interpreted as LST deposition, resulting from down slope transport of sediment initiated from upper slope failure or carbonate highstand shed due to decreased accommodation space due to relative falls in sea level. Seismic-scale geometries of these conglomeratic units indicate carbonate-dominated gravity flow deposits of toe-of-slope debris flow aprons (Decie Ranch and Sullivan Peak Members) and mixed hybrid event beds (Sullivan Peak Member).

Reciprocal sedimentation within the Wolfcamp A (Poplar Tank Member) interval is indicated by integrated chemo/litho facies. These changes in sedimentation occur as a direct result of local variations in source (carbonate vs siliciclastic) and chemistry of the paleoenvironment during the deposition of the Upper Wolfcamp Formation throughout transgressive and highstand systems tract (HST & TST) deposition. As a result, we interpret that the reservoir stratigraphy is reflective of the environment in which they were deposited, thus influencing properties such as composition, organic abundance, and distribution or architecture. Furthermore, analysis of the sedimentological characteristics and geochemical proxies of the facies within the Poplar Tank Member lead us to the following:

- (1) The high values of redox-sensitive proxies, absence of sedimentary structures, lack of mud, and presence of shallow marine fauna within Facies 1a (skeletal packstone/grainstone) indicate storm event deposition of slope-attached carbonate

- storm beds occurred within an anoxic/suboxic environment during interpreted highstand in sea level.
- (2) The abundance of mud/clay grains, lack of grading and sedimentary structures, high redox proxy values, and low detrital proxy values of Facies 1b (skeletal wackestone) indicate a lower energy, anoxic/suboxic depositional environment, likely along a depositional slope ramp setting below the storm wave base.
 - (3) Low redox proxy values, and high detrital proxy values indicate deposition of Facies 3 and 4 occurred within an oxic/suboxic environment during early-to-mid TST and HST.
 - (4) Dilution of the carbonate strata occurs at the expense of hemipelagic sedimentation of fine-grained siliciclastic grains.
 - (5) Carbonate-rich deposits (Facies 1 and 2) are interbedded with siliceous/argillaceous mudstone within the HST and is indicative of Upper Wolfcamp mixed carbonate-siliciclastic reciprocal sedimentation.

Geochemical analysis of the mudrock successions within the Lenox Hill outcrops aid in our correlation of the Upper Wolfcamp Formation as being coeval to the Wolfcamp A Formation in the subsurface of the Delaware Basin. The Base Leonardian Unconformity is picked at the base of the Wedin Member of the Cathedral Mountain Formation, which appears to correlate to the base of the Bone Springs in the subsurface of the Delaware Basin. This study establishes a consistent regionally correlative framework, which provides sequence stratigraphic significance to the Upper Wolfcamp (Skinner Ranch) Formation in outcrops. Furthermore, this evaluation aids in understanding spatio-temporal variations, as well as lithologic and geochemical heterogeneity of basin-floor strata, which comprise the unconventional source rock plays of the Wolfcamp A Formation. Modern chemostratigraphic techniques indicate that redox influences sediment

chemistry, organic matter accumulation, and when coupled with bioproductivity proxies and other geochemical markers, can be useful in interpreting units with hydrocarbon potential.

REFERENCES

- Adams, J.E. et al., 1939, Standard Permian section of North America: AAPG Bulletin, 23, p. 1673-1681.
- Adams J. E., 1965, Stratigraphic-Tectonic Development of Delaware Basin. AAPG Bulletin 1965; 49 (11): 2140–2148.
- Adams, D.C., & Keller, G.R., 1996, Precambrian Basement Geology of the Permian Basin Region of West Texas and Eastern New Mexico: A Geophysical Perspective. AAPG Bulletin, 80, 410-431.
- Algeo, T.J. and Rowe, H., 2012, Paleoceanographic applications of trace-metal concentration data: Chemical Geology, v. 324-325, p. 6-18.
- Alvarez, J. O., and Schechter, D.S., 2016, Wettability, Oil and Rock Characterization of the Most Important Unconventional Liquid Reservoirs in the United States and the Impact on Oil Recovery. Paper presented at the SPE/AAPG/SEG Unconventional Resources Technology Conference, San Antonio, Texas, USA, August 2016.
- Baumgardner Jr, R. W., DiMichele, W.A., and de Siqueira Vieira, N., 2016, An early Permian coastal flora dominated by Germaropteris martinsii from basinal sediments in the Midland Basin, West Texas: Palaeogeography, Palaeoclimatology, Palaeoecology, 459, p. 409-422, doi: 10.1016/j.palaeo.2016.07.024.
- Bievenour, A., and Sonnenberg, S., 2019, Reservoir Characterization of the Bone Spring and Wolfcamp Formations, Delaware Basin, Ward County, West Texas. Paper presented at the SPE/AAPG/SEG Unconventional Resources Technology Conference, Denver, Colorado, USA, July 2019. doi: <https://doi.org/10.15530/urtec-2019-633>
- Blakey, R., 2019, North America Paleogeographic Maps: Deep Time Maps TM.
- Caf, A.B., and Pigott, J.D., 2021, Dolomitization geometry and reservoir quality from supervised Bayesian classification and probabilistic neural networks: Midland Basin Leonardian Wichita and Clear Fork Formations, Interpretation 9: T585-T598. <https://doi.org/10.1190/INT-2020-0204.1>.
- Cherney, J.L., 1998, Investigation of anisotropy from Spraberry horizontal cores: Fourth Annual Naturally Fractured Reservoir Symposium Petroleum Recovery Research Center, New Mexico Institute of Mining and Technology, Socorro, NM, October 27, 1998.
- Cohen, K.M., Finney, S.C., Gibbard, P.L. & Fan, J.-X., 2013; updated, The ICS International Chronostratigraphic Chart: Episodes v. 36: p. 199-204.

- Colborne, J. and Sonnenberg, S., 2019, Reservoir Facies, Depositional Processes, and the Implications on Reservoir Characterization of the Wolfcamp A, Texas Delaware Basin: In Unconventional Resources Technology Conference, 11 pp., DOI:10.15530/urtec-2019-316.
- Cooper, G.A., and Grant, R.E., 1964, New Permian stratigraphic units in Glass Mountains, West Texas: American Association of Petroleum Geologists Bulletin, v. 48, no. 9, p. 1581-1588.
- Cooper, G.A., and Grant, R.E. 1966. Permian rock units in the Glass Mountains, West Texas, In: Contributions to stratigraphy, 1966: U.S. Geological Survey Bulletin 1244-E: E1-E9.
- Cooper, G.A., and Grant, R.E., 1972, Permian brachiopods of West Texas; I: Smithsonian Contributions to Paleobiology, no. 14, 183 p.
- Cooper, G.A. & Grant, R.E., 1973. Dating and Correlating the Permian of the Glass Mountains in Texas. In: A. Logan & L.V. Hills, Eds., The Permian and Triassic Systems and their Mutual Boundary. Canadian Society of Petroleum Geologists, Memoir (Calgary), 2:363-377.
- Craddock, P.R., Herron, M.M., Herron, S.L., 2017, Comparison of Quantitative Mineral Analysis By X-Ray Diffraction And Fourier Transform Infrared Spectroscopy. Journal of Sedimentary Research, 87 (6): 630–652.
- Cys, J.M., and S.J. Mazzullo, 1978, Lithofacies and sedimentation of Lower Permian carbonates of the Leonard Mountain area, Glass Mountains, western Texas: a discussion; Journal of Sedimentary Petrology, v. 48, p. 1363-1368.
- Cys, J. M., 1981, Preliminary report on proposed Leonardian lectostratotype section, Glass Mountains, West Texas: Symposium and Guidebook, 1981 Field Trip, Permian Basin Section, Society of Economic Paleontologists and Mineralogists, pp. 183-205.
- Davydov, V I, Glenister, B F, Spinosa, C, Ritter, S M, Chernykh, V V, Wardlaw, B R, and Snyder, W S, 1995, Proposal of Aidaralash as the GSSP for the base of the Permian System, Permophiles 26, p. 1-9.
- Derby, J.R., Fritz, R.D., Longacre, S.A., Morgan, W.T., & Sternbach, C.A., 2012, The Great American carbonate bank : the geology and economic resources of the Cambrian-Ordovician sauk megasequence of Laurentia.
- Dickson, J.A., 1965, Modified Staining Technique for Carbonates in Thin Section. Nature 205, 587. <https://doi.org/10.1038/205587a0>.
- Donovan, A., J. Evenick, L. Banfield, N. McInnis, and W. Hill, 2017, An Organofacies-Based Mudstone Classification for Unconventional Tight Rock and Source Rock Plays, Unconventional Resources Technology Conference, Austin, Texas, USA, SPE/AAPG/SEG, p. 15.

- Driskill, B., Pickering, J. and Rowe, H., 2018, Interpretation of High Resolution XRF data from the Bone Spring and Upper Wolfcamp, Delaware Basin, USA: Unconventional Resources Technology Conference.
- Dunham, R. J., 1962, Classification of carbonate rocks according to depositional texture. Memoir - American Association of Petroleum Geologists, 108-121.
- EIA, 2020, Wolfcamp, Bone Spring, Delaware Shale Plays of the Delaware Basin, U.S. Energy Information Administration report, accessed on February 21, 2022.
- Ewing, T.E., 2016, Texas Through Time: Lone Star Geology, Landscapes, and Resources: The University of Texas at Austin, Bureau of Economic Geology Udden Series No. 6, 431 p.
- Fitchen, W.M., 1997, Lower Permian sequence stratigraphy of the western Delaware Basin margin, Sierra Diablo, West Texas.
- Flores, R.M., T.L. McMillan, and G.E. Watters 1977. Lithofacies and Sedimentation of Lower Permian Carbonate of the Leonard Mountain Area, Glass Mountains, Western Texas. *Journal of Sedimentary Petrology*, 47(4): 1610-1622.
- Folk, R.L., 1968, Petrology of Sedimentary Rocks, University of Texas Publication, Austin, p. 170.
- Galley, J. E., 1958, Oil and geology in the Permian Basin of Texas and New Mexico, in *Habitat of Oil: American Association of Petroleum Geologists, Special Publication*, p. 395-446.
- Gastaldo, R.A., DiMichele, W.A., and Pfefferkorn, H.W., 1996. Out of the icehouse into the greenhouse: A late Paleozoic analogue for modern global vegetational change: *Gsa Today*, v. 6, p. 1-7.
- Gaswirth, S. B., K. L. French, J. K. Pitman, K. R. Marra, T. J. Mercier, H. M. Leathers Miller, C. J. Schenk, M. E. Tennyson, C. A. Woodall, M. E. Brownfield, and T. M. Finn, 2018, USGS National and Global Oil and Gas Assessment Project-Permian Basin Province, Delaware Basin, Wolfcamp Shale and Bone Spring Assessment.
- Herron, S. L. and Herron, M. M. (1996). Quantitative lithology: an application for open and cased hole spectroscopy. In *SPWLA 37th Annual Logging Symposium*, pages 1–14, New Orleans, Louisiana.
- Hill, C. A., 1995, Geology of the Delaware Basin: Guadalupe, Apache and Glass Mountains, New Mexico and West Texas: *SEPM Special Publication No. 96-39*, 480 pp.
- Janson, X., Zahm, C. and Welch, P., 2017, Marathon Thrust Influences on Lower Permian Deposition: In *West Texas Geological Society 2017 Fall Symposium Field Trip*, Bureau of Economic Geology at The University of Texas at Austin, 177 pp.

- Jones, B., Manning, D.A.C., 1994, Comparison of geochemical indices used for the interpretation of palaeoredox conditions in ancient mudstones, *Chemical Geology*, Volume 111, Issues 1–4, Pages 111-129.
- Kerans, C., 2000, Stratigraphic architecture and paleokarst development within the Abo (Leonardian 1) composite sequence, Apache Canyon and Kingdom Abo field, Permian basin, in S. T. Reid, *Southwest Section AAPG 2000 Convention Transactions: West Texas Geological Society Publication SWS 2000-107*, p. 250.
- King, P. B., 1930, *The Geology of the Glass Mountains, Texas*, The University of Texas Bulletin, The University of Texas, p. 165.
- Kohn, J. L., 2016, Late Pennsylvanian (Virgilian) to early Permian (Leonardian) conodont biostratigraphy of the “Wolfcamp Shale,” Northern Midland Basin, Texas: M.S. thesis, Texas Tech University, Lubbock, Texas, 112 p.
- Kvale, E. P., C. M. Bowie, C. Flentrop, C. Mace, J. M. Parrish, B. Price, S. Anderson, and W. A. DiMichele, 2019, Facies variability within a mixed carbonate-siliciclastic sea-floor fan (upper Wolfcamp Fm., Permian, Delaware Basin, New Mexico): *AAPG Bulletin*, v. 104, p. 525-563.
- Li, S., Yu, X., Li, S., Giles, K., 2015, The role of sea level change in deep water deposition along a Carbonate Shelf Margin, Early and Middle Permian, Delaware Basin: Implications for reservoir characterization. *Geologica Carpathica*. 10.1515/geoca-2015-0013.
- Lucia, F.J., and Ruppel, S.C., 1996, Characterization of Diagenetically Altered Carbonate Reservoirs, South Cowden Grayburg Reservoir, West Texas. Paper presented at the SPE Annual Technical Conference and Exhibition, Denver, Colorado, October 1996. doi: <https://doi.org/10.2118/36650-MS>.
- Mazzullo, S., and Reid, A., 1989. Lower Permian platform and basin depositional systems, northern Midland Basin, Texas: *SEPM Special Publication*, v. 44, p. 305-320.
- Meyers, P.A. 1994. Preservation of elemental and isotopic source identification of sedimentary organic matter. *Chemical Geology*. 114: 289-302.
- Mu G., Singh N., Wang S., Wright M., Davis E., and Bao L., 2013, Chemostratigraphy and sequence stratigraphic investigation of the Lower Silurian-Upper Ordovician Hot Shale, Southeastern of the Sichuan Basin, SPE Unconventional Resources Conference and Exhibition-Asia Pacific, Paper SPE 167022, Brisbane, Australia, 11-13 November, 10 p, doi:10.2118/167022-MS.
- Nance, H.S. and Rowe, H., 2015, Eustatic controls on stratigraphy, chemostratigraphy, and water mass evolution preserved in a Lower Permian mudrock succession, Delaware Basin, west Texas, USA: Interpretation, SH11-SH25, doi: <http://dx.doi.org/10.1190/INT-2014-0207.1>

- Nestell, M.K., Nestell, G.P., and Wardlaw, B.R., 2019, Integrated fusulinid, conodont, and radiolarian biostratigraphy of the Guadalupian (Middle Permian_ in the Permian Basin region, USA, *in* Ruppel, S.C., ed., *Anatomy of a Paleozoic basin: the Permian Basin, USA* (vol. 1, ch. 9): The University of Texas at Austin, Bureau of Economic Geology Report of investigations 285; AAPG Memoir 118, p. 251-291.
- Phillips II, N. D., 1991, Refined subsidence analysis as a means to constrain late Cenozoic fault movement, Ventura Basin, California. MS Thesis, The University of Texas at Austin, 121 p.
- Poole, F. G., W. J. Perry, Jr., R. J. Madrid, and R. Amaya-Martínez, 2005, Tectonic synthesis of the Ouachita-Marathon-Sonora orogenic margin of southern Laurentia: Stratigraphic and structural implications for timing of deformational events and plate-tectonic model, *in* T. H. Anderson, J. A. Nourse, J. W. McKee, and M. B. Steiner, eds., *The Mojave-Sonora Megashear Hypothesis: Development, Assessment, and Alternatives*, v. 393, Geological Society of America.
- Pyles, D.R., Jennette, D.C., Tomasso, M., Beaubouef, R.T., and Rossen, C., 2010, Concepts learned from a 3D outcrop of a sinuous slope channel complex: Beacon Channel Complex, Brushy Canyon Formation, West Texas, USA: *Journal of Sedimentary Research*, v. 80, no. 1, p. 67–96, [https:// doi .org /10 .2110 /jsr .2010 .009](https://doi.org/10.2110/jsr.2010.009).
- Ratcliffe, K.T., Wilson, A., Payenberg, T., Rittersbacher, A., Hildred, G.V. and Flint, S.S., 2015, Ground truthing chemostratigraphic correlations in fluvial systems: *AAPG Bulletin*, v. 99, no. 1, p. 155-180. DOI: 10.1306/06051413120.
- Reid, A. M., S. T. Reid, S. J. Mazzullo, and S. T. Robbins, 1988, Revised fusulinid biostratigraphic zonation and depositional sequence correlation, subsurface Permian basin: *AAPG Bulletin*, v. 72, p. 102.
- Richards, B. H., Wehner, M., Pope, M. C., Donovan, A. D., 2021, An Integrated Chemo and Sequence Stratigraphic Analysis of Extended (>1000 ft) Lower Permian Wolfcamp Cores, Reagan County, Southern Midland Basin, *AAPG Bulletin*, in review.
- Ross, C. A., 1960, Fusulinids from the Hess Member of the Leonard Formation, Leonard Series (Permian), Glass Mountains, Texas: *Contributions from the Cushman Foundation for Foraminiferal Research*, v. 11, Pt. 4, pp. 117-133.
- Ross, C. A., 1963, Standard Wolfcampian Series (Permian), Glass Mountains, Texas: *GSA Memoir* v. 88, Geological Society of America, 205 p.
- Ross, C. A., 1986, Paleozoic evolution of southern margin of Permian basin: *Geological Society of America Bulletin*, v. 97, p. 536-554.
- Ross, C. A., and Ross, J. R. P., 1994, Permian sequence stratigraphy, *in*, Scholle, P. A., Peryt, T. M., and Ulmer-Scholle, D. S., eds., *The Permian of Northern Pangea*, Vol. 1, Springer-

- Verlag, Berlin, Heidelberg, New York, pp. 98-123.
- Ross, C. A., and Ross, J. R. P., 1998, Bursumian Stage, uppermost Carboniferous of Midcontinent and Southwestern North America: *Carboniferous Newsletter*, v. 16, p. 40-42.
- Ross, C. A., and Ross, J. R. P., 1998, Bursumian Stage, uppermost Carboniferous of Midcontinent and Southwestern North America: *Carboniferous Newsletter*, v. 20, p. 39-40.
- Ross, C.A., Ross, R.P., 2003, Sequence evolution and sequence extinction: Fusulinid biostratigraphy and species-level recognition of depositional sequences, Lower Permian, Glass Mountains, West Texas, U.S.A. In: Olson, H. C. and Leckie, R. M., Eds., *Micropaleontologic proxies for sea-level change and stratigraphic discontinuities*, 317–359. Tulsa, Oklahoma: SEPM (Society for Sedimentary Geology). Special Publication, 75.
- Roush, R. S., 2015, Regional stratigraphic and core-based characterization of the Cline Shale, Midland Basin, Texas: Doctoral Dissertation, The University of Texas at Austin, Department of Geological Sciences.
- Rowe, H., N. Hughes, and K. Robinson, 2012, The quantification and application of handheld energy-dispersive Energy Dispersive X-Ray Fluorescence (ED-ED-XRF) in mudrock chemostratigraphy and geochemistry: *Chemical Geology*, v. 324-325, p. 122-131.
- Rowe, H., Morrell, A., Nieto, M., Nance, S., Narasimhan, S., Mainali, P., Ganser, N., Garza, J. and Grillo, J., 2017, Inorganic Geochemical Characteristics of Lithofacies and Their Linkages to the Mechanical Stratigraphy of Upper Wolfcamp and Bone Spring Formations, Delaware Basin, Texas, 8 pp. DOI: 10.15530/urtec-2017-2689141.
- Ruppel, S.C., 2019, Anatomy of a Paleozoic basin: the Permian Basin. USA: introduction, overview, and evolution, *in* Ruppel, S.C., ed., *Anatomy of a Paleozoic basin: the Permian Basin, USA* (vol. 1, ch. 1): The University of Texas at Austin, Bureau of Economic Geology Report of investigations 285, AAPG Memoir 118, p. 1-27.
- Sano J.L., Ratcliffe K.T., and Spain D.R., 2013, Chemostratigraphy of the Haynesville Shale, in Hammes U. and Gale J. (eds), *Geology of the Haynesville Gas Shale in East Texas and West Louisiana, USA*, American Association of Petroleum Geologists Memoir 105, pp 137-154.
- Schieber, J., J. B. Southard, and A. Schimmelmann, 2010, Lenticular shale fabrics resulting from intermittent erosion of water-rich muds—Interpreting the rock record in the light of recent flume experiments: *Journal of Sedimentary Research*, v. 80, no. 1, p. 119–128, doi:10.2110/jsr.2010.005.
- Schlager, W., Reijmer, J.J.G., Droxler, A., 1994, Highstand shedding of carbonate platforms. *J Sediment Geol*, 64-3:270 – 81.

- Silver, B.A., and Todd, R.G., 1969. Permian cyclic strata, northern Midland and Delaware basins, west Texas and southeastern New Mexico: *Assoc.Petroleum Geologists Bull.*, v. 53, p. 2223-2251.
- Soto-Kerans, G.M., Stockli, D.F., Janson, X., Lawton, T.F., and Covault, J.A., 2020, Orogen proximal sedimentation in the Permian foreland basin: *Geosphere*, v. 16, no. 2, p. 567– 593, <https://doi.org/10.1130/GES02108.1>.
- Tabor, N.J., Montañez, I.P., Scotese, C.R., Poulsen C.J., and Mack, G.H., 2008, Paleosol archives of environmental and climatic history in paleotropical western Pangea during the latest Pennsylvanian through early Permian, in Fielding, C.R., Frank, T.D., and Isbell, J.L., eds., *Resolving the Late Paleozoic Ice Age in Time and Space: Geological Society of America, Special Publication 441*, p. 291– 303, doi: 10.1130/2008.2441(20).
- Temple, M., P. Filzmoser, C. Reimann, 2008, Cluster analysis applied to regional geochemical data – problems and possibilities: *Applied Geochemistry*, v. 23, p. 2198–2213.
- Tribovillard, N., Algeo, T.J., Lyons, T. and Riboulleau, A., 2006, Trace metals as paleoredox and paleoproductivity proxies: An update: *Chemical Geology*, v. 232, p. 12-32.
- Udden, J. A., 1917, Notes on the geology of the Glass Mountains, *BEG Bulletin 1753*, University of Texas, Austin, Bureau of Economic Geology and Technology.
- Wahlman, Gregory. (2013). Lower Permian (Wolfcampian) Carbonate Shelf-Margin and Slope Facies, Central Basin Platform and Hueco Mountains, Permian Basin, West Texas, USA. 10.2110/sepmsp.105.09.
- Wahlman, G. P. and West, R. R., 2010. Fusulinids from the Howe Limestone Member (Red Eagle Limestone, Lower Council Grove Group) in northeastern Kansas and their significance to the North American Carboniferous (Pennsylvanian)-Permian boundary. Lawrence: Kansas Geological Survey. *Current Research in Earth Sciences, Bulletin 258* (4), 13 pp.
- Ward, Z., 2017, Depositional Processes and Environments in Wolfcampian-leonardian Strata, Southern Midland Basin, Texas.
- Wardlaw, B. R., and Nestell, M. K., 2019, Conodont biostratigraphy of Lower Permian (Wolfcampian – Leonardian) stratotype sections of the Glass and Del Norte Mountains, West Texas, USA, in Ruppel, S.C., ed., *Anatomy of a Paleozoic basin: the Permian Basin, USA* (vol. 1, ch.8): The University of Texas at Austin, Bureau of Economic Geology Report of Investigations 285; AAPG Memoir 118, p. 229-249.
- Wilde, G. L., 1975, Fusulinid-defined Permian stages: West Texas Geological Society and Permian Basin Section, Society of Economic Paleontologists and Mineralogists Publication, v. 75, no. 65, p. 67-83.

- Winfree Keith, E., 1994, Post-Permian folding and fracturing of the Spraberry and San Andres formations within the Midland Basin region of West Texas, West Texas Geological Society 94-95: 189-212.
- Winfree Keith, E., 1995, Post-Permian epirogenic uplift and fracturing within the Midland Basin of West Texas, American Association of Petroleum Geologists and Society of Economic Paleontologists and Mineralogists 4: 105.
- Wuellner, D. E., L. R. Lehtonen, and W. C. James, 1986, Sedimentary-tectonic development of the Marathon and Val Verde basins, West Texas, USA: a Permo-Carboniferous migrating foredeep, *in* P. A. Allen, and P. Homewood, eds., Foreland basins, v. 8, The International Association of Sedimentologists, p. 347-368.
- Yang, K.-M., and S. L. Dorobek, 1995, The Permian Basin of west Texas and New Mexico: Tectonic history of a “composite” foreland basin and its effects on stratigraphic development, Stratigraphic evolution of foreland basins: SEPM Special Publication, v. 52, SEPM Society for Sedimentary Geology, p. 149-174.
- Ye, Hongzhuan & Royden, Leigh & Burchfiel, Clark & Schuepbach, Martin, 1996, Late Paleozoic deformation of interior North America: The greater Ancestral Rocky Mountains. *Aapg Bulletin - AAPG BULL.* 80. 1397-1432.
- Zeller, M., Reid, S. B., Eberli, G. P., Weger, R. J., and Massaferro, J.L., 2015, Sequence architecture and heterogeneities of a field–Scale Vaca Muerta analog (Neuquén Basin, Argentina)—From outcrop to synthetic seismic: *Marine and Petroleum Geology* v. 66, p. 829-847, doi: 10.1016/j.marpetgeo.2015.07.021.

APPENDIX

Sample Name	Bottom Depth (cm)	Outcrop Depth (cm)	AZO3 (wt%)	SiO2 (wt%)	CaO (wt%)	MgO (wt%)	K2O (wt%)	SO3 (wt%)	Rb (ppm)	Sr (ppm)	Zr (ppm)	FTIR Calculated TOC (wt%)	TO2 (wt%)	Fa2O3 (wt%)	MnO (wt%)	P2O5 (wt%)	Mo (ppm)	Ni (ppm)	V (ppm)	Th (ppm)	U (ppm)	Cr (ppm)	Zn (ppm)
CM_8	427.00	427.00	3.99	60.22	1.44	0.52	1.36	0.10	72.95	64.75	188.19	0.09	0.25	2.21	0.02	0.04	8.39	30.14	57.89	8.70	2.81	29.50	52.68
CM_8	425.00	425.00	4.56	64.27	2.67	0.47	1.53	0.08	90.05	71.84	217.53	0.10	0.32	2.82	0.03	0.05	6.18	43.90	64.33	7.90	3.30	56.58	82.27
CM_8	424.00	424.00	3.86	64.94	2.28	0.52	1.40	0.01	70.82	71.84	163.91	0.10	0.21	1.90	0.02	0.03	5.98	29.58	65.00	11.30	3.20	30.27	257.64
CM_8	423.00	423.00	4.97	63.88	3.73	0.54	1.77	0.12	92.07	70.82	198.31	0.18	0.29	2.60	0.03	0.05	5.41	46.03	91.58	7.70	2.20	40.89	205.53
CM_8	421.00	421.00	3.30	81.06	1.39	0.40	1.09	0.05	73.86	56.66	217.53	0.10	0.20	1.70	0.01	0.03	6.50	25.63	53.00	9.80	3.30	18.78	96.26
CM_8	420.00	420.00	1.97	68.98	2.00	0.46	1.07	0.12	59.70	54.64	99.15	0.09	0.28	2.23	0.01	0.02	6.05	33.86	87.37	9.30	3.61	13.79	27.17
CM_8	419.00	419.00	3.25	44.70	1.41	0.59	1.69	0.08	68.80	53.62	133.55	0.10	0.18	1.48	0.01	0.01	4.23	22.78	58.89	7.20	2.80	54.85	18.89
CM_8	417.00	417.00	5.54	77.89	1.15	0.64	1.63	0.01	80.94	73.86	236.76	0.17	0.23	2.07	0.02	0.08	7.42	23.52	80.13	9.20	2.51	49.93	26.38
CM_8	415.00	415.00	5.31	79.56	2.73	0.60	1.52	0.12	75.28	68.69	220.18	0.20	0.25	2.00	0.02	0.06	7.89	34.33	84.89	6.31	2.80	47.90	21.23
CM_8	413.00	413.00	2.78	58.88	4.00	0.33	0.60	0.03	22.02	35.83	191.99	0.18	0.25	2.13	0.02	0.04	6.25	31.25	66.25	8.40	2.71	63.08	120.90
CM_8	411.00	411.00	1.98	63.80	3.37	0.47	0.04	0.03	3.48	244.33	199.32	0.19	0.35	2.78	0.02	0.03	7.50	41.25	108.75	7.90	2.90	35.90	33.35
CM_8	410.00	410.00	3.23	83.40	1.89	0.49	0.79	0.06	27.00	42.35	239.79	0.11	0.30	2.42	0.01	0.02	6.53	35.89	94.61	8.05	2.89	36.96	29.26
CM_8	409.00	409.00	2.13	75.80	5.62	0.39	0.39	0.02	1.24	190.89	212.73	0.18	0.26	2.11	0.01	0.02	5.68	31.22	82.31	7.85	2.77	15.71	25.55
CM_8	408.00	408.00	1.87	71.20	4.53	0.52	0.12	0.04	7.27	275.76	223.34	0.16	0.23	1.83	0.02	0.02	4.94	27.16	71.61	7.96	2.76	29.89	22.62
SV Peak_8	400.00	400.00	1.20	30.05	39.55	0.66	0.20	0.03	10.20	110.42	97.34	0.65	0.15	0.97	0.03	<LOD	1.88	9.80	<LOD	1.19	1.46	<LOD	55.34
SV Peak_8	399.00	399.00	3.78	17.89	43.41	0.94	1.29	<LOD	4.66	198.85	40.08		0.16	1.33	0.08	0.07	1.91	23.02	14.72	2.10	3.00	<LOD	52.04
SV Peak_8	398.12	398.12	10.06	52.20	0.94	1.35	1.79	0.04	3.54	115.34	37.24		0.25	1.40	0.02	0.05	1.24	28.05	9.49	3.51	2.60	3.51	60.00
SV Peak_8	397.12	397.12	2.24	45.74	14.61	1.67	0.62	<LOD	3.04	66.78	27.32		0.06	1.09	0.01	0.47	1.78	14.04	19.85	2.80	1.90	48.95	19.03
SV Peak_8	396.50	396.50	4.61	58.96	11.96	4.26	1.08	0.02	23.70	40.82	72.51	1.61	0.18	0.95	0.01	<LOD	<LOD	7.70	27.97	2.17	0.88	20.37	85.19
SV Peak_8	396.12	396.12	2.30	14.19	30.14	1.05	0.18	0.04	16.85	71.07	62.50		0.02	0.20	0.02	0.25	2.89	20.03	7.02	3.11	2.51	<LOD	8.02
SV Peak_8	395.12	395.12	2.47	17.92	42.74	0.92	0.18	<LOD	21.95	85.87	58.40		0.02	0.17	0.01	0.30	3.10	34.02	16.50	4.11	2.31	<LOD	0.07
SV Peak_8	393.80	393.80	3.24	9.64	31.86	1.28	0.23	0.02	5.07	69.34	55.15		0.01	0.14	0.05	0.33	2.37	28.01	12.80	3.31	2.61	<LOD	15.04
SV Peak_8	392.80	392.80	2.65	14.86	46.20	0.90	0.15	<LOD	4.06	52.82	31.60		0.01	0.13	0.02	0.31	3.09	39.07	1.82	3.01	2.60	<LOD	7.08
SV Peak_8	391.80	391.80	4.68	25.21	27.45	1.84	0.62	0.03	22.30	32.54	49.40		0.07	0.63	0.03	0.20	2.84	22.05	6.27	1.70	2.70	4.80	11.01
SV Peak_8	390.80	390.80	5.09	11.82	38.26	1.02	1.19	<LOD	49.68	9.53	18.41		0.13	1.00	0.07	0.09	1.72	77.04	6.13	4.00	30.00	39.25	12.07
SV Peak_8	389.80	389.80	2.02	21.38	27.84	1.08	0.52	<LOD	38.52	9.33	14.71		0.05	0.92	0.07	0.15	2.39	8.06	17.35	4.51	2.01	39.64	9.06
SV Peak_8	388.48	388.48	7.11	1.43	76.44	1.44	1.75	<LOD	43.59	5.78	160.41		0.17	1.01	0.02	0.02	1.88	13.08	25.25	2.60	2.20	26.75	10.06
SV Peak_8	387.48	387.48	9.88	3.68	66.37	2.44	2.23	<LOD	59.59	7.50	23.51		0.02	1.63	0.04	0.05	1.63	17.84	11.72	1.31	3.30	24.45	11.86
SV Peak_8	386.48	386.48	8.14	2.19	53.74	2.10	1.88	<LOD	66.91	7.70	47.01		0.13	1.81	0.02	0.02	1.31	18.02	30.27	2.10	2.20	29.02	27.07
SV Peak_8	385.50	385.50	2.16	29.50	74.87	1.83	2.38	<LOD	89.95	7.50	93.81		0.30	1.64	0.09	0.03	0.96	21.07	16.61	3.11	2.00	16.68	14.03
SV Peak_8	385.00	385.00	1.23	82.46	7.09	0.19	0.40	<LOD	8.01	16.33	41.19	2.50	0.05	0.40	0.01	<LOD	<LOD	1.98	14.19	0.87	<LOD	6.89	66.11
SV Peak_8	384.48	384.48	2.54	84.09	0.27	0.38	0.89	<LOD	16.22	55.76	202.59		0.03	0.83	0.02	0.09	1.47	9.00	9.90	2.51	3.40	10.84	45.01
SV Peak_8	383.16	383.16	1.56	66.56	9.13	0.70	0.48	<LOD	14.19	81.10	178.47		0.01	1.06	0.02	0.09	1.00	7.01	50.74	3.20	3.80	47.36	139.07
SV Peak_8	382.16	382.16	1.18	4.76	56.21	0.87	0.41	<LOD	12.17	57.79	162.85		0.01	0.43	0.03	0.04	0.96	5.92	5.99	1.20	2.00	42.13	125.00
SV Peak_8	381.16	381.16	1.45	17.65	42.29	1.07	0.42	0.03	11.15	145.98	157.85		0.02	0.36	0.05	0.22	1.16	13.50	14.86	2.71	3.30	33.49	25.01
SV Peak_8	380.16	380.16	7.88	13.23	38.48	0.95	1.39	0.04	26.36	83.13	47.01		0.13	1.81	0.02	0.02	1.43	12.00	9.16	3.31	2.61	2.20	138.08
SV Peak_8	379.16	379.16	1.04	17.22	54.31	1.58	0.26	<LOD	7.10	79.07	101.57		0.02	0.37	0.07	0.11	1.09	10.18	17.35	2.80	2.31	10.67	168.08
SV Peak_8	377.50	377.50	1.24	40.68	22.41	8.34	0.28	0.04	9.77	48.46	31.42	0.00	0.05	0.43	0.01	<LOD	<LOD	5.83	2.73	0.98	1.07	8.57	106.51
SV Peak_8	376.84	376.84	4.52	44.34	11.19	4.32	0.80	<LOD	19.26	43.59	100.80		0.07	0.95	0.03	0.06	1.01	5.52	6.96	3.10	2.20	8.52	31.30
SV Peak_8	375.00	375.00	1.26	7.04	49.77	2.63	0.17	0.04	9.33	186.67	14.26	0.00	0.05	0.67	0.02	<LOD	2.56	21.89	<LOD	4.40	2.40	4.00	93.92
SV Peak_8	374.84	374.84	3.63	48.03	8.21	1.74	0.67	<LOD	2.13	39.54	84.00		0.06	0.84	0.03	0.07	1.46	8.00	7.30	4.70	3.01	18.20	44.00
SV Peak_8	373.84	373.84	3.85	10.23	32.55	4.62	0.28	0.06	10.14	180.59	68.95		0.03	0.37	0.01	0.24	2.45	26.00	13.93	4.40	0.80	<LOD	25.02
SV Peak_8	372.52	372.52	1.96	6.42	48.02	0.94	0.10	<LOD	7.59	37.06	42.78		0.03	0.04	0.00	0.19	2.53	46.00	16.76	4.01	1.70	<LOD	14.06
SV Peak_8	371.52	371.52	0.99	0.23	20.22	0.78	0.06	0.17	14.24	183.49	21.90		0.07	0.10	0.06	0.11	2.89	14.01	20.82	3.60	1.91	17.41	21.01
SV Peak_8	370.52	370.52	4.83	11.04	31.91	4.41	0.89	<LOD	5.07	275.75	52.33		0.05	1.04	0.04	0.32	3.00	18.00	20.61	4.10	1.80	11.70	106.05
SV Peak_8	369.52	369.52	2.11	14.87	51.93	1.02	0.09	<LOD	17.74	406.53	28.49		0.04	0.07	0.05	0.33	2.24	15.00	15.87	4.60	1.40	<LOD	10.07
SV Peak_8	368.52	368.52	3.59	34.49	7.94	0.78	0.13	<LOD	27.76	32.44	24.00		0.04	0.25	0.03	0.04	1.23	10.00	21.77	3.00	1.50	18.78	0.04
SV Peak_8	367.20	367.20	2.95	22.46	21.20	1.68	0.19	<LOD	4.06	61.84	44.94		0.10	0.22	0.03	0.15	0.84	9.00	10.51	3.40	1.30	20.05	52.02
SV Peak_8	366.00	366.00	6.85	22.87	26.37	11.87	1.04	0.06	40.27	181.11	37.30	0.00	0.03	0.36	0.05	0.22	1.16	13.50	14.86	2.71	3.30	33.49	25.01
SV Peak_8	365.00	365.00	3.35	20.46	27.85	13.13	0.56	0.08	23.26	117.64	31.42	0.00	0.11	3.00	0.12	<LOD	0.81	8.58	11.57	2.06	1.65	10.86	11.96
SV Peak_8	364.00	364.00	5.89	36.40	19.94	9.14	1.02	0.09	37.53	117.43	131.65	0.00	0.23	2.11	0.05	<LOD	<LOD	9.79	44.68	4.34	2.53	24.59	19.66
SV Peak_8	363.00	363.00	5.60	34.67	21.02	9.12	0.93	0.09	35.11	121.72	126.46	0.00	0.23	1.98	0.05	<LOD	<LOD	6.71	40.27	4.23	1.94	25.18	17.88
SV Peak_8	361.00	361.00	3.98	27.29	25.19</																		

SV Peak_8	331.28	-331.28	1.93	7.14	46.48	1.83	0.11	<0.00	10.62	43.19	7.00	0.33	0.15	0.04	0.24	3.07	27.01	36.04	1.81	2.81	<0.00	26.02	
SV Peak_8	329.96	-329.96	2.00	3.27	39.02	1.25	0.12	<0.00	14.57	39.64	3.20	0.64	0.23	0.08	0.29	2.18	25.01	8.58	1.31	2.71	<0.00	32.04	
SV Peak_8	328.96	-328.96	0.99	1.35	18.98	1.47	0.06	0.21	26.32	22.00	11.30	0.09	0.14	0.04	0.25	2.14	7.00	2.92	1.40	2.21	<0.00	24.02	
SV Peak_8	327.96	-327.96	1.43	9.36	21.43	1.57	0.36	<0.00	14.19	16.22	9.48	0.01	0.40	0.06	0.13	2.82	9.00	25.63	3.10	1.51	6.54	47.03	
SV Peak_8	326.96	-326.96	0.75	36.15	23.88	2.98	0.25	<0.00	10.14	16.32	67.39	0.11	0.85	0.06	0.23	0.70	13.00	33.35	1.60	2.00	39.21	14.07	
SV Peak_8	325.96	-325.96	1.70	15.31	32.52	1.12	0.14	<0.00	5.07	48.86	20.18	0.06	0.32	0.04	0.23	2.12	14.00	26.92	1.71	1.81	<0.00	12.05	
SV Peak_8	324.64	-324.64	6.36	20.39	32.61	1.39	0.60	<0.00	8.11	32.24	45.09	0.05	0.93	0.01	0.52	2.34	26.00	2.79	3.51	3.10	18.74	65.06	
SV Peak_8	323.64	-323.64	2.15	66.56	0.60	0.57	0.44	<0.00	14.19	1.42	101.67	0.22	0.36	0.02	0.06	0.89	6.00	11.07	3.00	2.10	16.41	26.00	
SV Peak_8	322.64	-322.64	0.91	17.14	25.31	1.20	0.18	<0.00	9.12	12.17	63.49	0.10	0.29	0.04	0.22	2.27	11.01	6.95	2.90	2.11	45.87	6.03	
SV Peak_8	321.64	-321.64	0.96	56.69	14.16	0.88	0.27	<0.00	9.12	3.85	114.01	0.14	0.37	0.07	0.13	0.73	51.00	10.61	4.70	3.10	27.01	12.03	
SV Peak_8	320.64	-320.64	1.48	2.12	30.64	0.97	0.10	0.05	10.14	44.71	8.41	0.07	0.14	0.07	0.16	2.62	3.01	7.29	2.40	2.90	62.71	0.09	
SV Peak_8	319.32	-319.32	1.87	15.35	29.06	1.67	0.29	<0.00	7.10	12.88	34.40	0.01	0.22	0.04	0.21	2.38	15.01	28.89	2.30	2.80	25.37	17.04	
SV Peak_8	318.32	-318.32	3.16	13.90	46.11	0.74	0.23	<0.00	5.07	59.20	19.49	0.03	0.22	0.07	0.30	2.20	28.00	4.16	2.60	2.20	<0.00	35.01	
SV Peak_8	317.50	-317.50	0.77	16.81	45.13	1.23	0.16	0.08	7.88	234.55	13.07	0.99	0.02	0.98	0.01	0.06	3.63	18.15	<0.00	1.74	2.82	<0.00	56.79
SV Peak_8	317.32	-317.32	3.19	9.02	44.67	0.84	0.20	<0.00	8.70	58.29	7.95	0.02	0.23	0.02	0.21	2.57	47.00	9.75	1.90	2.20	19.32	25.08	
SV Peak_8	316.32	-316.32	2.03	10.37	41.58	0.97	0.12	<0.00	3.65	31.22	13.85	0.06	0.16	0.05	0.33	2.68	49.00	29.49	2.60	1.70	13.21	51.00	
SV Peak_8	315.32	-315.32	3.23	11.15	44.81	1.60	0.25	<0.00	5.07	28.89	20.18	0.01	0.23	0.04	0.31	2.32	38.00	21.89	2.00	3.21	45.40	18.03	
SV Peak_8	315.00	-315.00	0.34	4.01	52.65	0.90	0.06	0.04	3.62	216.55	4.09	0.19	<0.00	0.20	0.01	<0.00	2.83	22.11	<0.00	<0.00	0.58	<0.00	8.11
SV Peak_8	314.00	-314.00	1.40	13.84	27.67	0.92	0.12	0.07	3.62	26.87	31.04	0.06	0.08	0.04	0.28	2.80	17.00	44.96	2.60	1.90	42.14	20.07	
SV Peak_8	313.00	-313.00	3.07	72.91	6.94	1.94	0.58	<0.00	16.22	3.45	73.04	0.33	0.61	0.03	0.14	0.56	11.01	17.18	3.00	2.70	33.98	87.07	
SV Peak_8	312.00	-312.00	2.85	9.02	43.93	1.16	0.18	<0.00	7.60	49.98	26.73	0.01	0.22	0.08	0.28	2.23	39.01	18.86	1.90	2.30	<0.00	17.01	
SV Peak_8	311.00	-311.00	3.68	9.08	31.56	0.87	0.37	0.03	5.07	57.68	17.38	0.03	0.29	0.03	0.26	2.58	28.00	17.79	3.20	3.00	<0.00	32.03	
SV Peak_8	310.00	-310.00	1.79	46.10	24.49	1.46	0.18	<0.00	12.64	11.05	57.61	0.10	0.27	0.03	0.17	2.10	7.01	28.09	3.70	3.10	26.71	12.07	
PT_B	295.00	-295.00	2.44	83.96	6.62	0.38	0.69	<0.00	25.02	40.71	64.13	0.92	0.15	1.12	0.02	0.01	<0.00	28.82	37.22	2.39	1.65	28.31	75.20
PT_B	292.50	-292.50	0.37	7.03	51.96	0.54	0.05	0.04	3.95	277.57	4.89	0.00	0.00	0.25	0.01	<0.00	2.69	20.02	<0.00	<0.00	<0.00	10.30	
PT_B	289.00	-289.00	3.18	82.48	5.94	0.52	0.83	<0.00	26.09	44.06	64.23	2.73	0.22	1.24	0.01	0.02	0.81	26.84	44.05	3.26	1.85	55.26	133.97
PT_B	282.50	-282.50	<0.00	9.97	50.38	0.70	<0.00	0.04	2.19	336.91	2.59	0.00	<0.00	0.15	0.02	<0.00	2.42	19.47	<0.00	<0.00	<0.00	8.01	
PT_B	280.00	-280.00	0.50	27.11	39.90	0.47	0.11	0.04	6.47	245.54	10.77	0.31	0.03	1.04	0.02	0.15	2.42	17.38	<0.00	0.65	1.94	<0.00	10.40
PT_B	277.50	-277.50	2.88	15.88	44.19	1.08	0.59	0.05	23.70	206.87	30.32	0.00	0.14	0.85	0.10	<0.00	2.83	75.23	<0.00	2.50	1.17	<0.00	11.96
PT_B	276.50	-276.50	7.00	43.04	23.61	2.53	1.76	0.02	60.68	191.22	80.38	0.22	0.37	2.64	0.03	<0.00	1.08	29.26	66.45	5.32	3.89	95.48	15.19
PT_B	275.00	-275.00	5.84	45.93	23.95	2.19	1.46	0.03	50.03	110.94	101.33	1.46	0.36	1.19	0.02	0.06	0.81	31.89	52.04	4.56	6.22	98.30	100.58
PT_B	274.00	-274.00	4.40	41.97	26.33	1.05	0.77	0.05	41.15	57.25	122.07	0.96	0.41	1.90	0.01	<0.00	<0.00	33.76	121.86	4.34	2.72	41.79	162.47
PT_B	273.00	-273.00	8.70	66.75	7.22	2.19	2.06	<0.00	66.71	87.08	204.55	2.00	0.56	2.69	0.02	0.05	<0.00	24.42	66.97	7.27	3.50	79.50	182.13
PT_B	272.00	-272.00	10.39	68.91	3.95	2.20	2.64	<0.00	88.44	74.73	225.80	1.08	0.66	3.18	0.03	0.02	<0.00	45.42	80.12	8.36	3.89	89.74	79.78
PT_B	271.00	-271.00	11.12	69.97	2.98	2.80	2.78	0.01	92.06	86.03	215.82	0.08	0.88	3.17	0.03	0.02	<0.00	53.56	88.00	8.47	3.79	153.05	37.13
PT_B	269.00	-269.00	9.37	62.02	9.10	2.68	2.24	<0.00	78.78	123.71	179.02	2.36	0.58	3.47	0.02	0.12	<0.00	40.36	70.76	7.38	4.28	194.94	157.27
PT_B	268.00	-268.00	5.36	44.81	28.13	1.86	1.14	0.03	44.66	147.58	104.12	0.77	0.39	1.91	0.15	<0.00	4.17	61.81	60.45	4.45	2.14	54.53	81.75
PT_B	267.00	-267.00	9.86	73.16	2.66	2.30	2.54	<0.00	86.79	65.52	168.35	0.00	0.57	3.54	0.03	0.03	<0.00	51.69	80.64	7.92	3.89	94.75	57.83
PT_B	266.00	-266.00	11.02	75.05	1.75	2.24	2.75	<0.00	95.90	65.21	176.53	0.00	0.59	3.30	0.02	0.04	<0.00	42.12	86.21	8.68	3.31	97.68	40.19
PT_B	265.00	-265.00	11.56	71.99	1.23	2.26	2.99	<0.00	108.30	62.90	181.12	0.35	0.63	4.04	0.01	0.05	<0.00	34.53	87.79	9.01	3.79	120.66	30.75
PT_B	264.00	-264.00	11.59	73.21	0.85	2.00	3.03	<0.00	108.41	59.03	172.04	0.00	0.64	3.77	0.02	0.03	<0.00	41.35	93.68	8.90	3.50	114.29	45.14
PT_B	263.00	-263.00	12.01	69.61	2.37	2.43	3.14	<0.00	120.69	62.79	154.39	0.00	0.63	4.11	0.03	0.05	<0.00	62.36	108.82	9.23	4.57	147.77	34.43
PT_B	262.00	-262.00	11.39	72.39	1.85	2.44	2.94	<0.00	107.97	76.72	154.09	0.00	0.59	3.61	0.02	0.04	<0.00	53.34	83.90	9.12	4.57	161.72	45.26
PT_B	261.00	-261.00	10.00	72.64	2.95	2.27	2.58	0.00	93.37	62.16	149.60	0.00	0.54	3.28	0.02	0.04	<0.00	67.20	72.02	8.58	4.38	155.76	53.67
PT_B	260.00	-260.00	5.08	78.23	6.21	1.03	1.17	<0.00	40.49	53.17	98.63	1.46	0.33	1.94	0.06	0.05	3.23	84.47	61.51	4.45	2.63	82.32	213.75
PT_B	259.00	-259.00	0.59	13.99	47.21	0.66	0.11	0.06	6.80	255.11	11.27	0.77	0.02	0.83	0.05	<0.00	2.96	23.32	<0.00	0.52	0.68	<0.00	47.85
PT_B	258.00	-258.00	7.24	77.14	4.76	1.58	1.83	0.03	57.17	60.29	118.88	0.60	0.42	2.18	0.01	0.03	<0.00	25.30	59.82	4.99	2.53	76.16	150.62
PT_B	257.00	-257.00	8.48	78.83	3.12	1.43	2.08	0.01	68.03	52.65	143.62	0.69	0.48	2.73	0.01	0.05	<0.00	27.61	61.81	6.51	3.21	91.83	150.51
PT_B	256.00	-256.00	10.45	74.97	1.95	2.01	2.65	<0.00	91.51	59.34	165.06	0.64	0.58	3.17	0.01	0.04	<0.00	33.21	83.90	8.36	3.11	107.39	121.90
PT_B	255.00	-255.00	11.59	72.90	1.20	1.86	2.99	<0.00	110.16	53.27	184.36	0.00	0.63	3.97	0.01	0.04	<0.00	49.94	112.18	9.23	4.28	132.78	147.80
PT_B	254.00	-254.00	9.85	69.51	2.91	1.81	2.49	<0.00	90.30	60.18	164.96	0.00	0.56	3.12	0.05	0.03	1.48	75.01	73.60	7.82	3.40	120.03	44.62
PT_B	253.00	-253.00	12.97	64.50	4.10	2.36	3.38	<0.00	123.88	77.35	184.31	0.00	0.70	4.16	0.01	0.07	<0.00	50.10	101.14	10.42	4.96	184.70	58.87
PT_B	252.00	-252.00	3.13	16.15	42.02	3.85	0.64	0.04	24.47	273.17	49.07	0.60	0.15	1.70	0.03	<0.00	2.69	19.69	3.78	2.39	<0.00	28.73	13.73
PT_B	251.00	-251.00	11.71	70.69	2.																		

PT_B	212.00	-212.00	0.85	48.41	28.55	0.36	0.23	0.02	10.20	187.56	20.64	2.41	0.07	3.39	0.04	0.05	6.19	48.17	15.98	1.41	2.63	30.30	49.72
PT_B	211.00	-211.00	10.17	73.00	2.88	2.38	2.44	<0.00	77.24	61.86	206.65	0.32	0.65	2.93	0.13	0.05	<0.00	151.77	71.39	7.71	3.99	118.26	155.40
PT_B	210.00	-210.00	9.77	65.82	3.91	2.47	2.39	1.32	80.43	71.38	196.47	1.46	0.63	3.02	0.03	0.02	<0.00	69.28	66.03	7.72	3.60	108.65	143.85
PT_B	209.00	-209.00	10.33	72.81	2.50	2.30	2.52	<0.00	79.66	61.02	186.50	0.00	0.62	3.13	0.04	0.03	<0.00	42.12	62.45	7.38	3.31	101.86	148.64
PT_B	208.00	-208.00	10.41	69.68	2.67	2.11	2.60	<0.00	89.31	62.58	187.60	0.00	0.64	3.71	0.01	0.03	<0.00	39.04	84.95	8.68	4.38	107.60	94.76
PT_B	207.00	-207.00	11.16	69.85	2.33	2.28	2.86	<0.00	95.02	62.27	182.11	0.00	0.67	4.04	0.02	0.03	<0.00	38.16	75.28	8.68	4.76	112.41	134.70
PT_B	206.00	-206.00	10.91	69.97	2.56	2.34	2.74	<0.00	89.09	63.95	200.76	0.70	0.69	3.48	0.04	0.05	<0.00	58.51	75.17	8.47	5.18	136.75	88.10
PT_B	205.00	-205.00	9.79	70.75	2.91	2.16	2.50	<0.00	78.78	63.95	181.12	1.00	0.61	3.03	0.02	0.07	<0.00	44.32	71.07	7.82	4.47	141.87	295.71
PT_B	204.00	-204.00	8.89	76.06	2.44	2.00	2.16	<0.00	68.36	60.91	186.20	0.58	0.59	2.85	0.01	0.04	<0.00	44.32	67.39	6.51	4.57	117.11	328.58
PT_B	203.00	-203.00	9.81	67.47	3.61	2.34	2.31	1.44	75.60	80.28	206.65	1.18	0.64	2.89	0.02	0.03	<0.00	54.77	67.08	7.38	4.28	119.57	106.93
PT_B	202.00	-202.00	11.13	69.78	2.76	2.26	2.78	<0.00	91.51	68.55	220.31	1.08	0.70	3.47	0.02	0.04	<0.00	36.40	71.70	8.58	4.47	118.51	86.64
PT_B	201.00	-201.00	10.72	68.56	4.06	2.37	2.64	<0.00	89.75	85.20	209.64	0.92	0.67	3.16	0.02	0.06	<0.00	37.83	73.70	8.47	3.99	108.33	23.72
PT_B	200.00	-200.00	1.76	10.41	33.95	15.88	0.36	0.05	15.36	571.78	29.72	0.00	0.08	1.90	0.09	0.06	1.75	14.19	45.84	1.52	<0.00	6.79	9.88
PT_B	199.00	-199.00	11.34	69.30	2.69	2.41	2.76	<0.00	91.29	70.75	229.19	0.68	0.72	3.60	0.01	0.04	<0.00	29.15	89.47	8.58	5.15	107.18	34.12
PT_B	198.00	-198.00	9.96	71.50	3.55	2.24	2.39	<0.00	76.59	71.49	236.07	1.79	0.65	3.16	0.02	0.07	1.35	27.61	71.49	7.82	4.67	125.99	157.68
PT_B	197.00	-197.00	10.30	70.74	3.14	2.44	2.46	<0.00	78.12	73.26	253.32	1.46	0.71	3.24	0.02	0.12	<0.00	40.47	71.49	9.68	4.47	133.93	125.74
PT_B	196.00	-196.00	10.12	68.97	2.27	1.97	2.50	<0.00	83.99	58.19	211.33	0.88	0.63	3.08	0.01	0.03	2.29	32.66	70.34	7.92	4.67	114.60	60.74
PT_B	195.00	-195.00	0.80	30.55	36.52	0.62	0.17	0.06	8.45	314.83	16.06	1.50	0.05	2.69	0.06	0.10	7.13	29.26	15.35	1.41	4.08	10.24	10.40
PT_B	194.00	-194.00	10.17	71.87	1.70	1.89	2.61	<0.00	81.74	57.15	176.63	0.96	0.60	3.60	0.01	0.12	<0.00	39.59	72.44	8.03	6.81	175.09	402.84
PT_B	193.00	-193.00	9.65	76.53	1.32	1.90	2.37	<0.00	78.78	56.83	178.22	0.56	0.59	2.95	0.07	0.05	1.21	103.93	83.69	7.16	5.54	150.43	497.08
PT_B	192.00	-192.00	10.60	74.37	1.31	1.93	2.67	<0.00	90.52	52.54	167.85	0.00	0.60	3.36	0.01	0.06	<0.00	39.59	74.96	7.71	4.47	145.42	169.30
PT_B	191.00	-191.00	10.46	76.03	0.72	1.62	2.63	<0.00	87.89	49.51	171.04	0.46	0.62	3.69	0.04	0.08	<0.00	56.86	79.06	7.82	4.67	130.06	136.15
PT_B	190.00	-190.00	10.67	73.08	1.35	1.87	2.77	0.01	96.78	60.18	178.32	0.00	0.61	3.17	0.03	0.06	<0.00	60.82	79.80	7.92	4.96	120.14	63.67
PT_B	189.00	-189.00	11.29	71.73	1.46	1.88	3.00	<0.00	105.55	56.52	170.04	0.13	0.65	3.38	0.01	0.04	<0.00	37.72	96.83	8.79	4.57	140.62	46.29
PT_B	188.00	-188.00	1.38	22.82	41.20	0.58	0.24	0.07	12.84	245.02	16.95	0.32	0.08	1.50	0.04	<0.00	4.04	23.32	<0.00	1.52	1.65	6.89	30.37
PT_B	187.00	-187.00	9.61	76.56	2.70	1.96	2.26	<0.00	69.13	62.27	206.85	0.36	0.61	2.91	0.01	0.05	<0.00	30.03	63.40	7.16	3.89	109.27	223.73
PT_B	186.00	-186.00	9.54	75.40	2.54	1.90	2.23	<0.00	70.55	54.32	204.25	1.12	0.59	2.93	0.01	0.06	<0.00	46.96	68.44	7.16	5.15	122.26	143.95
PT_B	185.00	-185.00	12.94	69.51	1.89	2.10	3.25	<0.00	114.66	59.03	196.77	0.00	0.71	3.92	0.01	0.05	<0.00	37.50	79.48	9.88	4.47	132.54	37.13
PT_B	184.00	-184.00	0.66	9.82	49.39	0.87	0.12	0.06	6.14	337.75	9.28	0.00	0.04	1.08	0.06	<0.00	3.23	17.27	<0.00	0.76	1.26	<0.00	14.77
PT_B	183.00	-183.00	1.37	12.08	47.62	0.97	0.21	0.05	9.55	256.85	10.17	0.01	0.06	1.08	0.07	<0.00	3.63	22.77	<0.00	0.47	<0.00	<0.00	16.54
PT_B	182.00	-182.00	1.18	12.70	46.64	0.73	0.20	0.05	10.20	296.05	23.94	0.32	0.07	1.39	0.05	0.07	4.04	29.26	<0.00	1.30	1.65	<0.00	15.19
PT_B	179.00	-179.00	11.85	68.47	2.08	2.21	2.95	<0.00	100.07	72.43	225.80	0.15	0.73	3.63	0.01	0.08	<0.00	40.36	90.94	9.44	5.15	179.48	48.99
PT_B	178.00	-178.00	12.77	66.43	1.65	2.28	3.26	<0.00	122.12	64.89	206.15	0.00	0.76	4.27	0.01	0.05	<0.00	43.44	119.23	9.66	5.06	235.16	159.35
PT_B	177.00	-177.00	12.32	67.96	2.17	2.30	3.08	<0.00	109.39	67.93	237.26	0.23	0.74	3.84	0.02	0.06	<0.00	45.86	80.01	9.77	4.28	192.12	240.17
PT_B	176.00	-176.00	10.60	72.65	2.16	2.10	2.51	<0.00	77.57	57.77	261.00	0.57	0.71	2.93	0.02	0.04	<0.00	31.56	61.93	8.36	3.89	111.57	74.27
PT_B	164.00	-164.00	10.91	67.94	3.45	2.57	2.58	<0.00	80.54	76.82	270.28	1.29	0.75	3.71	0.01	0.05	<0.00	31.56	61.93	8.36	3.89	111.57	74.27
PT_B	163.00	-163.00	11.62	65.43	3.74	2.87	2.64	<0.00	84.49	87.71	263.40	0.59	0.74	3.79	0.04	0.04	<0.00	61.81	83.06	8.47	3.50	118.88	62.20
PT_B	162.00	-162.00	9.36	51.70	18.43	2.54	2.05	0.01	66.49	120.68	204.65	2.91	0.65	3.52	0.03	0.02	<0.00	36.51	41.95	6.95	3.99	110.11	50.86
PT_B	161.00	-161.00	10.24	57.89	10.44	2.61	2.39	<0.00	79.11	103.72	219.71	2.18	0.69	3.58	0.02	0.02	<0.00	30.90	72.97	7.92	4.34	119.99	91.12
PT_B	160.00	-160.00	0.48	63.52	18.94	0.15	0.18	0.04	6.80	132.82	28.72	2.80	0.04	1.79	0.02	0.25	0.94	10.45	25.44	1.90	2.14	19.91	41.61
PT_B	156.00	-156.00	7.68	84.35	0.95	0.95	1.72	<0.00	52.23	37.78	113.00	1.54	0.43	2.35	0.01	0.07	0.81	40.03	68.97	5.54	3.80	98.41	190.14
PT_B	154.00	-154.00	6.54	84.58	2.08	0.87	1.50	<0.00	47.62	43.75	100.33	1.29	0.38	2.21	0.01	0.10	0.81	51.58	83.80	4.34	5.54	133.09	315.89
PT_B	153.00	-153.00	9.12	78.82	1.38	1.27	2.05	<0.00	64.74	42.81	137.53	0.25	0.51	2.69	0.01	0.07	2.02	53.89	72.02	6.62	5.44	133.61	193.78
PT_B	152.00	-152.00	9.73	80.10	1.65	1.42	2.21	<0.00	73.52	47.94	140.42	1.00	0.53	2.74	0.00	0.18	1.48	54.00	70.86	7.16	6.80	200.65	257.12
PT_B	145.00	-145.00	0.30	4.12	44.41	12.46	0.06	0.04	4.81	369.63	81.18	0.00	0.00	1.30	0.08	0.05	3.10	31.12	8.10	0.52	<0.00	<0.00	68.13
PT_B	144.00	-144.00	0.12	12.96	34.11	15.12	0.03	0.03	2.96	387.78	3.59	0.00	<0.00	0.87	0.05	0.08	2.69	8.25	18.61	<0.00	<0.00	<0.00	9.67
PT_B	137.00	-137.00	0.22	22.58	41.65	0.54	0.06	0.06	4.94	315.98	8.78	1.02	0.01	1.46	0.03	0.08	2.56	13.31	<0.00	0.65	<0.00	<0.00	18.20
PT_B	135.00	-135.00	4.76	79.26	4.85	1.13	1.12	<0.00	39.06	60.60	106.42	2.28	0.31	2.01	0.03	0.10	<0.00	62.80	62.77	4.12	5.06	134.97	489.59
PT_B	134.00	-134.00	9.79	76.36	2.54	2.04	2.06	<0.00	78.67	63.84	147.51	0.61	0.54	3.05	0.01	0.07	<0.00	69.29	77.17	7.06	4.86	160.67	263.47
PT_B	133.00	-133.00	10.70	77.96	0.95	1.76	2.41	<0.00	81.52	47.31	166.06	0.39	0.61	3.56	0.01	0.07	<0.00	53.89	90.10	7.71	5.06	137.58	111.09
PT_B	132.00	-132.00	10.83	73.52	1.76	1.86	2.49	<0.00	91.29	54.32	183.11	0.74	0.62	3.16	0.01	0.08	<0.00	70.61	110.29	8.25	5.54	194.94	162.99
PT_B	131.00	-131.00	9.59	74.24	1.87	1.74	2.15	<0.00	70.22	52.33	156.08	1.75	0.54	3.60	0.03	0.07	1.21	133.41	84.64	6.84	6.51	228.16	398.06
PT_B																							

CM 85	366	-366	3.63	77.83	2.79	1.01	2.93	0.1	49.56	99.11	285.2	0.36	1.63	0.02	0.04	4.76	37.06	78.06	9	1.31	52.8	105.05
CM 85	365	-365	3.1	66.58	1.13	1.28	2.41	0.06	73.83	97.09	208.34	0.31	2.11	0.02	0.08	3.05	53.68	70.05	7.01	2.5	76.15	194.09
CM 85	364.2	-364.2	3.25	70.56	0.67	1.47	2.5	0.01	29.33	66.75	234.63	0.34	2.23	0.03	0.06	3.9	61.34	84.02	8	1.9	69.34	261.03
CM 85	363.2	-363.2	3.16	77.9	1.04	0.87	2.5	0.05	59.37	69.78	285.2	0.31	2.21	0.02	0.04	5.61	38.34	91.06	8	2.1	84.27	440.08
CM 85	361.88	-361.88	2.99	76.06	1.12	0.79	2.41	0.04	35.21	65.74	269.02	0.3	2.39	0.02	0.04	5.21	56.23	92.04	8	2.6	79.19	484.07
CM 85	360.88	-360.88	3.09	84.11	0.82	0.72	2.39	0.05	77.87	60.68	292.28	0.3	1.92	0.02	0.03	5.64	49.84	86.05	7	1.6	80.21	447.05
CM 85	359.88	-359.88	2.29	42.35	2.6	0.55	1.84	0.06	65.74	57.65	184.07	0.36	3.29	0.03	0.01	3.92	107.35	69.04	7	0.71	33.5	223.07
SV Peak 85	356.56	-356.56	1.15	51.19	14.48	12.07	0.31	0.11	6.07	47.53	90.35	0.01	0.31	0.01	0.10	2.26	20.03	20.76	2.21	1.00	30.65	64.05
SV Peak 85	355.56	-355.56	1.13	48.17	13.68	10.88	0.35	0.04	9.10	55.62	38.41	0.02	0.31	0.01	0.11	2.02	7.02	26.53	8.00	1.81	33.87	45.04
SV Peak 85	353.56	-353.56	0.79	1.95	40.82	1.02	0.48	0.11	11.12	22.25	11.12	0.05	0.04	0.02	0.09	3.18	23.52	30.96	5.04	1.70	<4.00	53.01
SV Peak 85	352.56	-352.56	0.86	11.32	36.19	0.73	0.39	0.07	9.10	35.40	27.98	0.01	0.09	0.02	0.09	3.31	18.00	27.11	3.84	1.21	<4.00	122.04
SV Peak 85	350.24	-350.24	1.76	2.02	44.39	0.86	0.75	0.06	14.16	18.20	13.15	0.01	0.20	0.01	0.01	3.88	14.05	18.66	3.56	2.01	<4.00	103.03
SV Peak 85	349.24	-349.24	1.23	16.12	41.90	4.70	0.43	0.06	9.10	24.27	25.96	0.02	0.36	0.01	0.11	4.16	9.04	16.86	3.09	1.80	<4.00	520.01
SV Peak 85	332.28	-332.28	0.60	12.85	21.64	2.50	0.35	0.09	13.15	33.37	23.90	0.03	0.11	0.02	0.11	4.13	16.05	18.36	2.65	2.70	29.78	448.04
SV Peak 85	329.96	-329.96	0.74	19.86	10.98	6.94	0.31	0.08	7.08	34.39	44.60	0.01	0.29	0.02	0.07	3.93	25.53	20.98	0.88	3.21	24.08	103.06
SV Peak 85	328.96	-328.96	0.50	22.39	11.95	6.50	0.24	0.10	6.07	34.39	55.22	0.01	0.40	0.01	0.05	3.24	32.05	20.24	0.95	1.70	20.39	102.05
SV Peak 85	327.96	-327.96	0.38	14.41	31.29	1.56	0.22	0.10	8.09	65.74	130.91	0.02	0.31	0.02	0.09	2.95	36.03	19.17	1.15	3.80	26.34	164.03
SV Peak 85	326.96	-326.96	1.49	24.46	24.73	4.81	0.40	0.09	8.09	27.31	70.98	0.02	0.46	0.02	0.08	3.14	29.52	21.16	1.54	2.50	36.84	246.08
SV Peak 85	324.64	-324.64	0.35	14.49	28.56	3.58	0.20	0.06	6.07	75.85	64.75	0.02	0.23	0.02	0.26	4.67	23.02	19.15	1.91	1.80	34.39	132.04
SV Peak 85	323.64	-323.64	0.50	15.12	60.26	6.02	0.15	0.06	4.05	68.77	75.53	0.01	0.25	0.05	0.16	5.11	31.04	24.57	2.19	1.70	<4.00	700.08
SV Peak 85	322.64	-322.64	1.50	9.50	28.38	9.85	0.11	0.03	4.05	140.58	125.44	0.01	0.28	0.13	0.13	5.62	38.06	29.01	2.21	1.31	21.90	#####
SV Peak 85	321.64	-321.64	1.83	0.37	38.43	0.73	0.07	0.06	5.30	282.17	39.35	0.01	1.00	0.00	0.26	5.62	33.01	32.57	1.96	1.81	21.70	180.01
SV Peak 85	320.64	-320.64	1.86	1.94	19.00	16.26	0.08	0.02	6.07	52.59	75.42	0.16	1.23	0.15	0.13	4.82	7.05	40.07	1.76	2.51	23.91	162.03
SV Peak 85	319.2	-319.20	1.86	1.41	18.48	15.71	0.07	0.06	6.07	48.54	88.23	0.04	0.04	0.13	0.10	3.89	7.02	56.20	1.69	2.20	28.96	11.06
SV Peak 85	317.88	-317.88	1.86	4.30	34.91	1.02	0.10	0.05	5.06	220.47	64.14	0.05	1.61	0.01	0.19	4.05	32.00	55.61	2.66	2.50	33.43	21.09
SV Peak 85	316.88	-316.88	1.33	0.19	29.92	1.11	0.07	0.06	5.06	397.46	20.70	0.03	1.42	0.01	0.21	4.51	22.05	49.18	3.90	3.30	35.22	22.08
SV Peak 85	315.88	-315.88	3.41	10.62	29.73	0.93	0.48	0.08	6.16	211.37	1.19	0.05	0.05	0.02	0.22	4.91	20.03	46.91	5.13	2.31	36.87	118.00
SV Peak 85	314.88	-314.88	2.87	4.15	41.64	0.79	0.18	0.11	5.19	387.35	8.32	0.02	0.08	0.02	0.31	4.78	32.06	35.13	5.62	1.51	39.92	87.08
SV Peak 85	313.88	-313.88	2.37	2.49	47.43	1.22	0.11	0.07	6.07	389.37	28.10	0.02	0.43	0.02	0.31	4.60	43.03	30.86	5.21	2.20	<4.00	19.01
SV Peak 85	312.56	-312.56	2.27	3.45	45.55	0.87	0.14	0.06	20.89	501.63	14.08	0.02	0.19	0.01	0.31	4.52	41.01	31.083	4.54	1.00	31.68	59.04
SV Peak 85	311.56	-311.56	2.02	2.75	39.11	1.07	0.12	0.06	17.04	436.90	19.57	0.01	0.07	0.01	0.40	4.26	26.04	23.85	3.75	1.20	24.75	36.02
SV Peak 85	310.56	-310.56	1.81	0.95	37.96	1.21	0.09	0.09	15.17	344.87	8.69	0.01	0.17	0.01	0.22	3.78	28.02	13.41	3.25	2.80	21.91	16.02
SV Peak 85	309.56	-309.56	2.79	7.58	42.17	1.43	0.17	0.08	12.90	428.81	12.64	0.01	0.09	0.00	0.27	3.03	30.00	14.03	2.65	2.50	<4.00	50.02
SV Peak 85	308.56	-308.56	2.36	17.31	29.59	2.00	1.62	0.10	23.26	61.69	166.35	0.16	0.03	0.07	0.06	2.42	17.01	13.40	1.96	1.80	47.38	314.07
SV Peak 85	307.24	-307.24	2.10	15.86	51.70	2.45	0.57	0.10	15.17	35.40	65.92	0.04	0.20	0.08	0.06	2.31	19.05	16.51	1.47	4.60	31.74	168.04
SV Peak 85	306.24	-306.24	2.58	13.57	60.94	4.82	0.64	0.08	18.20	34.39	164.81	0.05	0.87	0.14	0.05	2.48	9.05	27.57	1.15	3.10	<4.00	96.02
SV Peak 85	305.24	-305.24	2.44	14.64	25.67	1.40	0.62	0.06	20.23	21.24	118.39	0.06	0.39	0.07	0.02	2.99	9.00	44.08	1.03	3.90	23.83	68.04
SV Peak 85	304.24	-304.24	2.85	10.59	30.68	1.37	0.28	0.06	6.07	365.10	7.33	0.07	0.54	0.01	0.26	3.41	23.02	52.06	1.01	1.00	36.19	162.09
SV Peak 85	303.24	-303.24	1.66	1.27	37.36	1.80	0.09	0.03	9.16	393.42	16.92	0.08	0.41	0.01	0.30	3.60	28.00	70.03	0.96	1.80	31.10	35.02
SV Peak 85	301.92	-301.92	2.08	2.23	40.87	1.97	0.14	0.06	17.19	406.56	25.11	0.04	0.86	0.02	0.30	3.54	36.07	77.80	0.76	1.60	26.59	31.07
SV Peak 85	300.92	-300.92	2.78	2.91	48.31	1.09	0.15	0.02	18.20	432.86	43.77	0.04	0.04	0.02	0.34	3.34	36.03	75.32	0.80	1.20	23.58	46.08
SV Peak 85	299.92	-299.92	0.84	0.66	14.54	1.07	0.04	0.06	16.18	166.90	65.30	0.03	0.07	0.01	0.10	3.38	23.02	81.31	1.14	1.40	26.77	11.06
SV Peak 85	298.92	-298.92	1.38	19.17	32.86	0.95	0.08	0.05	14.16	283.18	101.35	0.03	0.14	0.01	0.21	3.52	23.00	80.81	1.50	1.90	30.47	63.03
SV Peak 85	297.92	-297.92	1.84	0.76	36.20	1.35	0.10	0.06	13.21	322.62	65.84	0.02	0.01	0.02	0.33	3.74	37.07	84.28	1.94	0.90	30.26	78.04
SV Peak 85	296.6	-296.60	1.47	3.54	28.47	1.19	0.09	0.08	13.15	192.15	74.47	0.02	0.15	0.01	0.24	4.04	17.05	89.27	2.32	1.50	31.33	141.08
SV Peak 85	295.6	-295.60	1.49	0.35	29.87	1.08	0.07	0.11	5.30	265.20	140.18	0.01	0.04	0.02	0.24	4.16	19.02	84.52	2.44	1.91	24.96	52.02
SV Peak 85	294.6	-294.60	2.25	0.38	51.05	1.51	0.09	0.07	6.16	449.04	4.00	0.01	0.25	0.02	0.30	4.61	45.07	75.05	2.10	1.91	<4.00	14.05
SV Peak 85	293.6	-293.60	1.38	24.75	28.50	1.72	0.08	0.06	5.19	121.36	63.81	0.06	0.03	0.05	0.17	5.14	14.05	65.31	1.49	2.80	24.32	20.01
SV Peak 85	292.6	-292.60	0.94	0.44	16.78	0.93	0.04	0.06	5.06	187.10	35.62	0.07	0.02	0.02	0.14	5.13	23.03	57.03	1.43	0.40	26.34	17.00
SV Peak 85	291.28	-291.28	1.84	3.10	33.60	0.87	0.16	0.09	8.09	331.72	75.56	0.08	0.03	0.03	0.26	4.30	23.01	59.02	1.85	1.90	31.01	51.06
SV Peak 85	290.28	-290.28	1.65	3.57	37.85	1.42	0.08	0.08	7.89	286.21	64.30	0.04	0.02	0.03	0.27	3.35	32.05	63.04	3.89	1.51	33.16	35.07
SV Peak 85	289.28	-289.28	3.60	11.15	31.08	2.62	0.39	0.10	6.85	287.22	3.56	0.05	0.13	0.01	0.24	3.54	30.07	67.52	5.95	2.50	37.14	189.09
SV Peak 85	288.28	-288.28	1.08	0.35	17.64	1.15	0.05	0.10	10.06	172.94	10.90	0.02	0.07	0.01	0.15	3.99	25.06	72.07	6.37	1.80	37.19	27.04
SV Peak 85	287.28	-287.28	1.68	0.16	40.11	0.94	0.07	0.08	8.07	295.31	32.69	0.02	0.81	0.01	0.28	4.43	25.05	67.06	5.28	1.81	37.18	11.08
SV Peak 85	285.96	-285.96	1.49	0.31	33.33	0.98	0.07	0.06	4.86	291.27	23.82	0.01	0.01	0.02	0.24	4.31	30.02	80.28	4.05	1.01		

SV Peak 8B	247.72	-247.72	1.35	2.41	18.80	1.34	0.13	0.13	5.67	313.52	30.35	0.03	0.44	0.00	0.15	5.14	10.07	14.96	1.12	2.11	34.42	9.08
SV Peak 8B	246.72	-246.72	2.41	6.57	39.99	1.27	0.16	0.06	8.03	509.72	19.71	0.01	0.34	0.00	0.23	4.70	34.00	21.00	1.39	2.90	28.62	21.09
SV Peak 8B	245.72	-245.72	2.14	5.01	37.23	1.27	0.12	0.06	12.10	458.14	55.27	0.02	0.08	0.00	0.26	4.57	29.05	32.02	2.12	2.01	24.96	8.06
SV Peak 8B	244.72	-244.72	2.36	5.62	38.10	1.27	0.15	0.06	4.05	566.36	74.92	0.01	0.58	0.00	0.23	4.52	38.01	49.36	2.23	1.70	20.35	29.03
SV Peak 8B	243.4	-243.40	2.65	5.87	43.67	1.14	0.16	0.01	5.67	606.81	136.36	0.01	0.24	0.01	0.28	4.39	44.03	62.33	2.23	2.00	28.64	56.08
SV Peak 8B	242.4	-242.40	2.27	3.11	37.98	1.36	0.15	0.06	8.03	611.87	48.09	0.05	0.29	0.01	0.27	3.88	29.00	77.67	2.18	4.00	33.79	30.09
SV Peak 8B	241.4	-241.40	2.48	5.58	41.44	1.03	0.20	0.02	4.05	680.64	3.97	0.06	0.26	0.01	0.27	3.06	30.06	77.00	1.50	2.20	33.87	9.02
SV Peak 8B	240.4	-240.40	0.96	5.68	28.28	1.40	0.20	0.18	4.05	283.18	46.72	0.07	0.20	0.02	0.21	2.22	20.03	80.33	1.63	1.60	26.44	9.02
SV Peak 8B	239.4	-239.40	2.51	5.16	38.12	1.72	0.19	0.02	5.30	479.38	57.31	0.01	0.64	0.01	0.24	1.99	15.05	77.33	1.87	1.50	21.30	9.03
SV Peak 8B	239.08	-239.08	1.27	2.29	16.62	1.21	0.14	0.06	6.07	241.71	7.56	0.02	0.59	0.01	0.13	2.80	17.03	52.44	4.48	2.71	22.10	8.02
SV Peak 8B	237.08	-237.08	3.62	8.21	33.06	1.77	0.36	0.05	6.07	550.17	16.41	0.03	0.46	0.01	0.23	2.77	17.06	64.14	5.35	1.20	24.53	62.02
SV Peak 8B	236.08	-236.08	0.77	4.96	28.44	2.74	0.20	0.11	5.06	236.66	5.72	0.05	0.13	0.01	0.22	3.35	19.07	44.77	5.56	1.80	28.28	83.01
SV Peak 8B	235.08	-235.08	2.65	7.89	28.66	1.35	0.25	0.05	5.06	563.32	14.67	0.03	0.59	0.03	0.25	4.20	26.06	37.17	5.94	1.80	33.99	54.04
SV Peak 8B	234.08	-234.08	0.64	4.97	28.43	1.27	0.15	0.05	6.16	207.33	5.13	0.01	0.79	0.01	0.18	3.29	14.04	35.30	4.13	0.71	33.89	12.04
PT 8B	232.76	-232.76	3.27	23.49	27.46	1.27	0.96	0.04	24.27	162.83	30.34	0.18	0.58	0.02	0.04	1.35	52.40	53.05	2.00	2.30	<1.00	33.89
PT 8B	231.76	-231.76	5.18	17.80	33.27	0.88	0.76	0.07	15.17	243.74	21.24	0.14	0.28	0.04	0.11	3.08	66.46	53.03	1.00	3.21	13.20	47.08
PT 8B	230.76	-230.76	6.42	43.54	61.13	0.73	2.26	0.02	59.66	116.31	181.03	0.65	0.89	0.17	0.11	3.51	181.00	53.08	4.00	2.61	91.38	380.06
PT 8B	229.76	-229.76	8.90	72.99	9.05	1.07	2.90	0.04	69.78	94.06	185.08	0.58	0.65	0.02	0.10	4.80	37.91	77.04	5.01	3.00	89.35	243.09
PT 8B	228.76	-228.76	10.53	69.56	3.85	1.07	2.98	0.02	98.10	117.32	240.70	0.68	2.26	0.03	0.10	3.95	78.05	69.00	5.00	2.70	85.29	108.07
PT 8B	227.44	-227.44	8.14	49.87	11.54	0.71	2.68	0.04	64.73	105.18	156.76	0.53	1.80	0.01	0.12	2.60	36.68	71.08	5.01	3.50	57.87	175.01
PT 8B	226.44	-226.44	9.62	68.78	2.37	1.00	2.91	0.03	79.90	73.83	159.79	0.55	1.96	0.02	0.13	4.75	35.68	71.09	6.00	4.01	71.07	112.02
PT 8B	225.44	-225.44	9.45	60.21	5.19	0.75	2.45	0.07	68.77	97.09	216.43	0.58	1.74	0.01	0.14	4.36	42.37	57.03	6.00	4.31	73.10	122.09
PT 8B	224.44	-224.44	11.62	47.54	1.14	0.73	3.61	0.08	120.35	814.14	264.97	0.74	2.05	0.02	0.19	3.92	61.33	122.01	7.00	3.90	86.30	313.04
PT 8B	223.44	-223.44	9.68	49.48	0.92	0.82	3.49	0.03	95.07	65.74	201.26	0.72	1.69	0.02	0.02	2.65	55.75	93.03	9.01	3.80	97.47	197.06
PT 8B	222.12	-222.12	1.52	3.33	28.53	0.68	2.33	0.02	75.85	44.50	148.67	0.58	2.96	0.02	0.09	2.16	92.55	20.09	5.01	3.40	221.34	16.03
PT 8B	221.12	-221.12	8.05	44.99	10.90	1.40	2.33	0.03	61.69	153.73	137.54	0.53	2.70	0.02	0.19	1.76	71.36	42.07	5.00	3.00	106.61	142.05
PT 8B	220.12	-220.12	10.44	69.32	3.80	1.14	3.33	0.02	104.17	91.02	227.55	0.67	0.15	0.02	0.11	3.90	41.26	70.07	6.00	4.20	109.65	187.01
PT 8B	219.12	-219.12	7.83	45.42	2.23	0.88	2.92	0.29	87.99	74.84	123.38	0.49	2.11	0.02	0.05	2.60	43.49	33.04	8.00	1.91	51.78	153.07
PT 8B	218.12	-218.12	11.07	75.60	1.66	1.20	3.63	0.05	124.40	72.82	172.94	0.65	1.85	0.03	0.07	3.47	63.56	86.01	7.00	5.11	89.35	114.04
PT 8B	216.8	-216.80	6.48	31.70	13.90	1.21	1.94	0.04	11.12	109.23	23.26	0.47	2.49	0.01	0.08	2.62	33.45	66.08	1.00	4.70	46.70	73.06
PT 8B	215.8	-215.80	4.76	26.53	14.11	0.47	1.46	0.04	15.17	80.91	15.17	0.57	2.33	0.00	0.10	2.18	18.96	66.03	1.01	3.00	<1.00	64.03
PT 8B	214.8	-214.80	4.76	42.11	12.72	0.75	2.88	0.02	23.26	48.54	10.11	0.23	1.46	0.02	0.03	1.77	53.52	21.07	1.00	3.61	72.09	34.11
PT 8B	213.8	-213.80	10.99	71.51	1.23	1.30	4.11	0.05	133.50	65.74	154.74	0.80	0.09	0.02	0.07	2.64	60.21	130.07	11.00	3.91	140.11	94.08
PT 8B	212.8	-212.80	9.84	68.96	1.23	0.90	3.79	0.03	114.28	75.85	104.88	0.66	0.75	0.02	0.10	2.63	71.36	108.02	9.00	2.51	111.68	105.09
PT 8B	211.48	-211.48	6.84	83.43	4.24	0.91	3.72	0.07	105.18	66.75	138.65	0.64	3.16	0.02	0.06	2.63	53.52	119.04	8.00	2.70	122.85	111.04
PT 8B	210.48	-210.48	1.74	9.23	31.80	0.68	2.80	0.01	72.82	75.85	112.26	0.49	2.65	0.03	0.11	5.61	124.00	115.07	7.01	3.11	<1.00	328.06
PT 8B	209.48	-209.48	8.90	70.41	4.57	0.74	3.21	0.02	83.94	76.86	137.54	0.57	2.56	0.02	0.10	2.67	67.66	79.04	7.00	3.20	110.67	170.01
PT 8B	208.48	-208.48	9.90	79.29	3.04	0.83	3.29	0.03	97.09	79.90	124.40	0.53	3.66	0.02	0.09	3.07	61.62	101.08	6.01	3.20	113.71	226.08
PT 8B	207.48	-207.48	10.39	79.14	1.69	0.90	3.46	0.04	109.23	76.86	133.80	0.55	2.32	0.02	0.08	2.59	51.96	108.07	7.00	4.51	107.62	237.01
PT 8B	206.16	-206.16	9.74	71.35	1.06	0.81	3.16	0.04	85.96	65.74	139.57	0.53	2.17	0.02	0.10	3.12	45.92	90.00	6.00	3.80	96.45	210.03
PT 8B	205.16	-205.16	4.47	51.02	2.11	0.58	1.36	0.03	41.47	56.64	71.81	0.28	2.17	0.01	0.07	2.15	31.42	70.06	4.00	3.90	54.83	141.04
PT 8B	204.16	-204.16	6.84	83.43	4.24	0.53	2.08	0.03	69.79	100.12	121.36	0.41	2.07	0.02	0.12	5.60	45.92	66.07	4.00	4.30	109.65	238.01
PT 8B	203.16	-203.16	8.87	82.48	3.18	0.77	0.17	0.03	73.83	180.02	5.06	0.08	1.36	0.00	0.12	4.77	54.37	18.02	1.00	4.71	149.87	17.00
PT 8B	202.16	-202.16	8.90	70.41	4.57	0.65	2.89	0.03	98.10	99.11	164.95	0.54	1.55	0.01	0.12	4.37	41.08	73.03	5.00	4.50	99.50	163.01
PT 8B	200.84	-200.84	4.24	45.11	3.09	0.55	1.46	0.02	49.56	83.94	80.91	0.34	0.35	0.01	0.03	4.30	27.79	82.07	4.00	4.70	48.73	81.08
PT 8B	199.84	-199.84	9.19	74.08	3.12	1.02	2.69	0.04	109.23	92.03	155.75	0.54	1.76	0.02	0.11	4.79	41.08	91.05	6.01	3.80	94.42	182.06
PT 8B	198.84	-198.84	1.74	9.23	41.68	0.89	2.94	0.03	22.25	89.00	136.52	0.52	1.20	0.02	0.09	3.09	35.04	81.06	6.00	3.20	79.19	143.07
PT 8B	197.84	-197.84	10.05	73.51	2.23	0.98	3.42	0.03	83.94	79.90	140.58	0.59	1.93	0.02	0.09	2.61	54.37	108.08	7.00	4.50	85.29	161.05
PT 8B	196.84	-196.84	12.10	83.27	1.05	0.95	4.21	0.05	96.08	65.74	148.67	0.67	1.60	0.05	0.07	3.08	100.29	104.03	8.00	5.40	83.25	167.01
PT 8B	195.52	-195.52	8.37	53.25	1.08	0.85	2.95	0.04	90.01	63.72	130.46	0.55	2.37	0.02	0.04	2.22	36.25	96.08	7.00	4.80	68.03	61.02
PT 8B	194.52	-194.52	10.72	49.36	1.83	0.73	3.67	0.12	106.19	56.64	164.85	0.65	2.30	0.02	0.10	3.07	49.54	96.02	8.01	4.90	98.48	78.02
PT 8B	193.52	-193.52	11.69	77.02	2.10	1.17	4.16	0.04	97.09	74.84	164.85	0.68	2.20	0.03	0.06	1.75	76.12	109.01	8.00	5.00	93.41	25.03
PT 8B	192.52	-192.52	3.48	57.18	8.23	0.51	1.07	0.04	28.32	232.61	37.42	0.21	2.88	0.03	0.02	2.67	55.58	38.00	3.00	5.00	46.70	14.04
PT 8B	191.52	-191.52	8.56	54.52	9.20	1.56	2.84	0.10	70.79	234.63	126.42	0.52	2.31	0.02	0.17	2.62	64.04	38.07	5.00	4.71	98.48	42.06
PT 8B	190.2	-190.20	11.79	77.22	2.32	1.49	4.08	0.10	90.01	96.08	160.80	0.67										

PT 88	151.96	-151.96	6.05	44.20	1.19	0.79	2.38	0.05	77.87	69.78	138.65	0.49	2.12	0.02	0.09	2.61	39.87	55.06	6.00	3.21	43.66	152.09
PT 88	150.96	-150.96	9.48	52.16	1.67	1.02	3.52	0.08	91.02	75.85	194.18	0.73	1.94	0.03	0.04	4.37	65.25	99.06	7.00	3.00	92.39	270.07
PT 88	149.96	-149.96	12.34	75.93	2.18	1.39	4.20	0.05	96.08	78.89	214.41	0.76	1.80	0.03	0.08	3.95	76.12	87.07	8.00	5.40	96.45	225.04
PT 88	148.96	-148.96	12.26	79.61	1.66	1.45	4.22	0.06	90.01	73.83	209.36	0.75	3.14	0.03	0.06	4.80	74.91	77.04	7.00	3.30	71.07	119.00
PT 88	147.64	-147.64	11.42	67.27	1.94	1.22	3.94	0.05	96.08	78.89	197.21	0.70	2.29	0.04	0.10	5.67	78.54	66.05	7.00	5.50	86.30	100.06
PT 88	146.64	-146.64	10.70	62.88	1.47	1.24	3.72	0.06	98.10	76.86	181.03	0.67	2.12	0.02	0.05	3.10	37.46	84.01	7.01	3.50	68.03	40.05
PT 88	145.64	-145.64	10.33	59.04	2.16	1.15	3.96	0.08	107.20	69.78	168.90	0.70	2.33	0.03	0.06	2.65	50.75	94.08	8.00	5.00	78.18	51.07
PT 88	144.64	-144.64	12.51	75.41	1.60	1.48	4.52	0.05	100.12	75.85	191.15	0.75	2.34	0.03	0.06	4.77	61.62	95.02	8.00	4.91	91.38	54.01
PT 88	143.64	-143.64	6.02	38.66	0.91	0.76	2.25	0.04	72.82	54.61	118.33	0.48	2.38	0.02	0.10	2.15	51.96	73.00	7.00	3.30	53.81	173.08
PT 88	142.32	-142.32	7.72	59.43	2.62	0.67	2.76	2.33	76.86	72.82	194.18	0.57	2.50	0.02	0.04	3.45	43.50	59.06	5.00	5.00	78.18	288.00
PT 88	141.32	-141.32	6.05	43.91	1.48	0.83	2.25	0.04	71.81	56.64	168.90	0.51	2.25	0.02	0.01	3.03	38.67	64.02	5.00	3.30	50.77	187.07
PT 88	140.32	-140.32	8.81	54.80	0.92	0.87	3.02	0.06	73.93	55.62	156.76	0.61	2.16	0.02	0.04	3.48	48.33	91.02	6.00	4.70	80.21	301.04
PT 88	139.32	-139.32	3.67	34.27	16.12	0.57	1.40	0.03	53.60	63.72	143.61	0.35	1.97	0.01	0.09	1.77	30.21	38.07	5.01	4.81	17.26	62.03
PT 88	138.32	-138.32	8.64	51.89	1.63	0.89	3.19	0.03	90.01	64.73	164.85	0.60	2.15	0.02	0.03	3.08	42.29	83.05	7.00	3.11	70.06	139.02
PT 88	137	-137.00	12.32	75.00	2.10	1.31	4.38	0.03	95.07	70.79	197.21	0.75	1.15	0.03	0.08	3.89	54.37	88.03	8.00	2.30	109.65	217.02
PT 88	136	-136.00	1.68	9.71	37.97	3.52	0.72	0.03	22.25	317.56	23.26	0.09	2.10	0.02	0.12	2.62	27.79	32.08	2.01	5.00	<L00	5.01
PT 88	135	-135.00	9.73	45.23	8.42	1.53	3.55	0.03	89.90	143.60	146.65	0.62	2.42	0.03	0.12	2.66	54.37	32.00	7.00	4.90	65.99	16.07
PT 88	134	-134.00	11.89	56.48	5.81	1.81	4.54	0.03	105.18	109.23	175.97	0.75	1.19	0.03	0.10	3.88	58.00	56.05	8.00	3.30	87.32	16.03
PT 88	133	-133.00	12.22	66.76	2.65	1.62	4.43	0.03	102.15	83.94	220.47	0.78	2.50	0.03	0.07	3.09	55.58	82.02	8.01	3.70	107.62	23.03
PT 88	131.68	-131.68	6.96	40.83	3.38	1.03	2.92	0.03	103.16	72.82	206.32	0.62	2.60	0.02	0.04	3.53	45.92	88.02	7.01	4.51	69.04	31.07
PT 88	130.68	-130.68	12.03	70.61	2.45	1.38	4.35	0.04	98.10	73.83	215.42	0.76	2.57	0.03	0.07	4.37	54.37	88.02	7.00	4.01	100.51	24.09
PT 88	129.68	-129.68	11.08	71.43	2.60	1.21	3.93	0.03	90.01	65.74	224.52	0.71	2.51	0.03	0.09	3.94	53.17	82.03	7.00	3.10	95.44	46.03
PT 88	128.68	-128.68	7.96	49.81	2.16	1.01	3.00	0.04	84.95	62.70	176.99	0.60	2.40	0.02	0.04	3.03	39.87	68.01	6.01	3.00	85.29	99.03
PT 88	127.68	-127.68	10.36	75.02	1.90	1.04	3.78	0.04	89.00	61.69	195.19	0.67	2.34	0.02	0.09	3.88	48.33	83.02	7.01	3.00	122.85	217.09
PT 88	126.36	-126.36	11.55	72.92	1.95	0.97	4.42	0.05	9.66	259.77	10.29	0.60	2.37	0.07	0.04	3.73	22.77	77.98	8.00	2.71	148.23	16.54
PT 88	125.36	-125.36	2.72	21.76	1.77	0.73	0.40	0.05	10.32	298.40	24.21	0.52	2.39	0.05	0.07	4.16	29.26	66.81	6.00	3.51	<L00	15.24
PT 88	124.36	-124.36	11.85	63.68	2.08	2.21	2.95	0.03	101.21	73.25	228.36	0.63	3.67	0.02	0.11	3.63	40.36	99.26	9.44	5.16	99.95	49.07
PT 88	123.36	-123.36	12.77	61.78	1.65	2.28	3.26	0.04	123.51	65.63	206.49	0.77	4.32	0.01	0.07	3.80	43.44	119.26	9.67	5.06	102.70	159.36
PT 88	122.36	-122.36	12.32	63.20	2.17	2.30	3.08	0.05	110.63	68.70	239.95	0.75	3.88	0.02	0.08	3.25	45.86	80.02	9.78	4.28	97.20	240.23
PT 88	121.04	-121.04	10.60	67.56	2.16	2.10	2.51	0.05	78.45	58.43	263.96	0.72	2.96	0.03	0.06	3.11	31.56	62.00	8.36	3.89	87.12	74.33
PT 88	120.04	-120.04	10.91	63.18	3.45	2.57	2.58	0.06	81.45	77.69	273.35	0.76	3.75	0.01	0.05	3.99	29.59	65.76	9.01	3.60	83.07	91.06
PT 88	119.04	-119.04	11.62	60.85	3.74	2.87	2.64	0.06	85.45	88.71	266.39	0.75	3.83	0.04	0.03	4.12	61.81	83.12	8.48	3.50	84.35	62.24
PT 88	118.04	-118.04	9.36	48.08	18.43	2.54	2.05	0.01	67.24	122.05	206.97	0.66	3.56	0.03	0.13	3.48	36.51	41.96	6.96	3.99	104.80	50.88
PT 88	117.04	-117.04	10.24	53.84	10.44	2.61	2.39	0.06	80.01	104.90	222.20	0.70	3.62	0.02	0.15	2.96	30.90	72.99	7.92	4.36	97.13	91.20
PT 88	115.72	-115.72	9.79	71.01	2.54	2.04	2.26	0.05	79.56	64.56	149.18	0.55	3.08	0.01	0.09	1.82	69.29	77.24	7.07	4.67	108.65	263.54
PT 88	114.72	-114.72	11.23	55.46	7.02	1.76	2.41	0.04	82.45	47.85	167.94	0.62	3.60	0.02	0.07	1.63	53.89	90.16	7.72	5.06	101.86	111.12
PT 88	113.72	-113.72	1.20	14.48	46.64	1.86	2.49	0.03	92.33	54.94	185.19	0.63	3.19	0.02	0.08	1.42	70.61	110.37	8.25	5.54	<L00	163.06
PT 88	112.72	-112.72	10.66	63.43	9.07	1.74	2.15	0.03	71.02	52.92	157.85	0.55	3.64	0.03	0.10	1.30	133.41	84.65	6.84	6.52	112.41	398.10
PT 88	111.72	-111.72	8.41	84.03	2.42	1.52	1.89	0.03	65.70	50.07	134.65	0.49	2.99	0.01	0.10	2.06	105.80	80.41	6.08	6.30	126.75	336.41
PT 88	110.4	-110.40	0.30	16.71	24.88	12.46	0.06	0.04	4.86	372.81	8.27	0.44	1.31	0.08	0.09	3.19	31.12	8.12	0.52	3.70	103.24	68.20
PT 88	109.4	-109.40	0.12	12.05	34.11	15.12	0.03	0.03	2.99	392.18	3.63	0.43	0.88	0.05	0.11	2.81	8.25	18.70	0.55	1.27	<L00	9.69
PT 88	108.4	-108.40	0.22	29.66	41.65	0.54	0.06	0.06	5.00	319.57	8.88	0.01	1.48	0.03	0.11	2.63	13.31	18.68	0.66	0.88	<L00	18.21
PT 88	107.4	-107.40	4.76	73.71	4.85	1.13	1.12	0.05	39.50	61.29	107.63	0.31	2.03	0.04	0.10	2.30	62.80	62.80	4.13	5.06	194.05	489.65
PT 88	106.4	-106.40	0.48	59.07	18.94	0.15	0.18	0.04	6.88	134.33	30.06	0.04	1.81	0.02	0.18	1.60	10.45	25.50	1.30	2.14	117.58	41.63
PT 88	105.08	-105.08	7.68	78.45	0.95	0.95	1.72	0.08	52.82	38.21	114.28	0.43	2.37	0.01	0.10	0.90	40.03	69.04	5.64	3.60	79.24	180.15
PT 88	104.08	-104.08	6.54	78.66	2.08	0.87	1.50	0.06	48.16	44.25	101.47	0.38	2.23	0.01	0.15	0.84	51.58	83.80	4.34	5.54	88.18	315.91
PT 88	103.08	-103.08	9.12	73.30	1.38	1.27	2.05	0.05	65.47	43.30	139.08	0.52	2.72	0.04	0.13	0.89	53.89	82.10	6.62	5.45	186.27	193.81
PT 88	102.08	-102.08	9.73	74.49	1.65	1.42	2.21	0.05	74.46	48.48	142.01	0.54	2.77	0.06	0.13	1.51	54.00	70.91	7.16	6.91	47.29	257.15
PT 88	101.08	-101.08	3.86	26.15	2.62	0.93	0.08	0.06	7.21	328.99	10.79	0.02	0.64	0.03	0.12	4.09	21.45	25.44	1.19	1.08	141.87	30.82
PT 88	99.76	-99.76	3.03	19.32	1.48	0.77	0.25	0.05	12.10	396.31	34.60	0.08	2.91	0.07	0.10	9.30	98.98	31.52	1.85	2.92	117.11	360.76
PT 88	98.76	-98.76	9.87	83.40	2.31	2.31	2.30	0.06	82.01	72.61	145.05	0.56	3.77	0.02	0.08	1.68	112.07	136.05	7.38	6.71	118.57	595.43
PT 88	97.76	-97.76	9.70	78.23	3.74	2.57	2.26	0.07	83.45	88.38	178.33	0.60	3.23	0.02	0.07	0.63	110.86	113.91	7.39	6.72	119.51	353.71
PT 88	96.76	-96.76	11.43	65.42	3.64	2.71	2.59	0.08	97.54	95.37	182.47	0.66	4.24	0.03	0.09	1.90	88.96	92.24	8.79	4.18	110.02	29.08
PT 88	95.76	-95.76	11.23	57.24	7.02	2.43	2.59	0.09	100.87	113.79	168.64	0.62	4.25	0.03	0.13	4.77	73.69	124.08	8.03	4.77	118.88	25.71
PT 88	94.44	-94.44	1.20	43.81	13.16	0.98	0.14	0.08	8.88	449.13	18.46	0.05	3.42									

DR 85	39.24	-39.24	2.56	6.49	36.41	1.16	0.22	0.16	6.07	408.59	14.62	0.02	0.52	0.01	0.20	1.73	40.42	21.36	7.98	3.40	35.94	15.06
DR 86	38.24	-38.24	1.30	8.17	29.91	1.23	0.09	0.04	9.66	#####	43.29	0.01	0.14	0.01	0.17	1.46	14.15	19.78	3.97	3.10	19.68	11.04
DR 87	37.24	-37.24	2.18	16.74	24.35	1.14	0.21	0.10	7.08	172.94	27.40	0.02	0.37	0.01	0.20	2.27	14.15	5.66	3.91	4.91	23.72	10.03
DR 88	35.92	-35.92	0.75	13.86	17.72	1.49	0.27	0.09	16.18	163.84	7.49	0.01	1.35	0.01	0.12	2.27	13.14	8.55	4.29	4.60	20.51	13.04
DR 89	34.92	-34.92	2.09	0.92	48.28	1.21	0.12	0.16	8.99	461.18	0.12	0.01	0.14	0.01	0.20	2.82	41.43	21.30	3.20	2.91	<0.0	7.01
DR 90	33.92	-33.92	1.85	2.95	37.53	0.92	0.11	0.10	16.03	420.72	16.31	0.03	0.09	0.02	0.18	3.70	43.45	24.78	2.83	3.31	30.99	16.08
DR 91	32.92	-32.92	1.31	0.45	28.55	0.87	0.06	0.29	17.14	308.46	28.11	0.03	0.04	0.02	0.20	2.78	26.27	34.40	2.04	2.70	31.78	10.08
DR 92	31.92	-31.92	2.66	21.17	30.73	1.13	0.26	0.29	7.08	118.43	4.08	0.04	0.60	0.11	0.24	2.71	46.48	64.16	0.74	7.40	39.19	15.04
DR 93	30.6	-30.60	1.10	15.16	15.14	1.33	0.33	0.09	18.20	155.75	10.84	0.03	0.50	0.04	0.10	3.07	13.14	70.73	0.93	2.80	30.70	11.03
DR 94	29.6	-29.60	0.81	13.85	32.11	1.25	0.13	0.09	4.88	686.71	6.22	0.04	0.31	0.04	0.24	2.81	14.15	77.30	1.52	4.51	46.91	12.06
DR 95	28.6	-28.60	0.26	8.88	18.08	1.04	0.18	0.03	15.17	54.61	12.49	0.07	0.37	0.02	0.15	2.93	7.07	86.39	0.93	4.41	35.17	8.02
DR 96	27.6	-27.60	1.96	1.21	35.20	0.78	0.14	0.09	4.55	109.21	10.47	0.12	0.10	0.01	0.26	3.67	24.25	74.77	1.10	5.50	35.94	9.07
DR 97	26.6	-26.60	2.52	16.82	37.74	0.87	0.26	0.07	13.15	724.13	6.31	0.05	0.46	0.01	0.22	3.40	27.28	77.80	0.84	2.90	19.68	65.02
DR 98	25.28	-25.28	2.33	4.84	32.90	0.99	0.15	0.02	5.71	433.67	0.32	0.01	0.17	0.02	0.22	3.34	30.31	88.41	0.69	2.40	23.72	41.05
DR 99	24.28	-24.28	1.81	3.54	40.26	0.77	0.13	0.13	7.77	367.12	38.25	0.04	0.11	0.02	0.15	5.03	14.15	92.45	0.90	2.71	20.51	18.03
DR 100	23.28	-23.28	1.61	5.53	40.26	0.90	0.09	0.07	4.86	523.88	9.33	0.04	0.11	0.01	0.18	5.03	34.36	89.92	1.38	2.80	17.51	28.03
DR 101	22.28	-22.28	2.70	6.40	33.62	1.29	0.27	0.05	13.98	405.55	88.47	0.02	0.24	0.02	0.22	3.27	39.41	78.30	1.64	1.40	11.87	36.08
DR 102	19.96	-19.96	2.09	2.92	46.57	1.27	0.08	0.05	21.97	747.39	74.08	0.02	0.09	0.01	0.30	2.52	36.38	61.64	2.25	2.60	<0.0	15.04
DR 103	18.96	-18.96	7.96	25.56	38.32	1.28	0.64	0.04	10.71	256.88	42.57	0.08	0.49	0.01	0.33	2.25	34.36	53.55	2.39	2.11	8.01	32.06
DR 104	17.96	-17.96	2.09	2.76	34.36	0.90	0.14	0.04	4.44	282.17	71.57	0.04	0.25	0.02	0.22	3.79	24.25	53.55	2.50	2.80	11.94	27.04
DR 105	16.96	-16.96	1.76	11.45	44.78	0.91	0.08	0.04	15.09	390.38	78.03	0.04	0.05	0.02	0.28	3.93	39.41	65.68	1.70	1.90	11.38	24.01
DR 106	15.96	-15.96	13.09	45.71	12.06	1.66	2.77	0.11	36.41	122.37	44.47	0.34	3.03	0.03	0.23	3.48	83.86	73.76	1.27	1.60	19.95	122.02
DR 107	14.64	-14.64	5.14	11.93	25.08	1.05	0.76	0.13	15.17	242.72	53.84	0.08	0.73	0.02	0.23	3.40	20.21	70.73	1.59	4.10	24.66	13.01
DR 108	13.64	-13.64	3.98	55.94	10.31	1.05	0.16	0.09	7.08	76.86	53.77	0.04	0.58	0.02	0.08	3.34	8.09	71.74	2.10	3.11	35.00	12.01
DR 109	12.64	-12.64	1.37	1.13	27.69	0.89	0.08	0.09	13.87	320.60	29.59	0.07	0.05	0.03	0.21	3.21	22.23	64.67	5.68	2.50	34.50	12.01
DR 110	11.64	-11.64	2.78	4.42	48.29	1.24	0.17	0.07	69.53	432.86	17.72	0.12	0.22	0.01	0.35	2.65	44.46	90.43	6.23	2.51	<0.0	23.00
DR 111	10.64	-10.64	0.67	2.68	26.85	1.09	0.12	0.10	72.74	147.66	22.06	0.37	0.08	0.03	0.23	1.84	15.16	110.64	6.52	3.20	33.38	19.07
DR 112	9.32	-9.32	2.09	2.19	19.83	1.49	0.07	0.10	27.74	83.94	13.04	0.34	0.06	0.05	0.16	1.02	12.13	59.11	4.05	3.30	46.07	23.09
DR 113	8.32	-8.32	1.37	7.17	18.13	1.34	0.08	0.07	31.01	116.31	20.31	0.33	0.06	0.06	0.13	0.75	11.11	31.32	4.05	2.61	43.67	11.01
DR 114	7.32	-7.32	0.67	2.06	22.19	1.34	0.17	0.11	36.73	105.18	16.90	0.16	0.05	0.05	0.18	1.57	20.21	56.58	3.55	1.90	16.93	18.06
DR 115	6.32	-6.32	0.81	0.58	21.14	1.34	0.06	0.04	30.74	115.29	4.65	0.20	0.02	0.09	0.13	1.57	16.17	52.04	3.33	2.11	22.83	10.05
DR 116	5.32	-5.32	1.11	3.62	36.25	2.04	0.11	0.05	32.13	174.96	8.73	0.19	0.08	0.10	0.27	2.11	16.17	60.12	2.05	3.30	25.34	16.07
DR 117	4	-4.00	0.70	4.27	29.75	1.09	0.12	0.05	25.08	187.10	14.88	0.18	0.06	0.05	0.26	3.00	20.21	76.79	1.69	2.60	18.18	21.07
DR 118	3	-3.00	0.75	6.28	34.05	1.60	0.10	0.04	9.66	165.86	95.61	0.12	0.07	0.02	0.23	2.08	21.22	27.46	1.78	2.81	13.53	11.01
DR 119	2	-2.00	0.67	0.60	28.60	0.90	0.08	0.03	8.99	123.38	145.97	0.10	0.03	0.01	0.21	2.00	19.20	34.63	1.35	3.10	12.38	10.03
DR 120	1	-1.00	0.81	0.61	26.15	1.29	0.07	0.05	16.03	105.18	10.27	0.05	0.05	0.01	0.18	2.36	16.17	71.33	3.85	3.20	8.57	8.07
DR Peak 0	0	0.00	0.67	1.74	33.77	1.36	0.11	0.05	17.14	172.94	146.14	0.09	0.06	0.02	0.23	2.10	20.21	58.27	1.89	1.80	7.73	8.07
SV Peak 10	232	-232.00	3.00	5.97	56.41	2.14	0.21	0.08	5.06	379.26	113.29	0.18	0.01	0.21	4.52	38.39	26.78	1.85	1.50	2.20	45.20	20.09
SV Peak 10	230	-230.00	2.32	35.61	6.85	3.28	0.15	0.17	8.09	69.78	92.37	0.23	0.01	0.08	4.86	19.70	33.37	1.58	3.70	2.30	48.25	16.30
SV Peak 10	213	-213.00	2.30	3.41	90.39	0.92	0.16	0.04	7.89	227.55	43.49	0.28	0.02	0.14	4.82	19.20	47.87	1.77	2.81	2.30	48.23	20.17
SV Peak 10	195	-195.00	1.05	18.58	34.62	0.99	0.21	0.04	3.03	72.82	41.47	0.27	0.01	0.15	4.62	12.13	46.63	3.21	2.61	3.80	46.20	69.85
SV Peak 10	162	-162.00	1.25	1.97	25.19	1.09	0.10	0.19	4.86	132.49	47.20	0.30	0.00	0.10	3.93	12.13	36.63	1.04	2.11	1.80	39.31	9.06
SV Peak 10	142	-142.00	2.47	5.10	46.61	0.95	0.21	0.08	6.07	495.55	29.67	0.26	0.01	0.16	3.62	15.16	28.36	1.13	2.71	2.90	36.23	24.03
SV Peak 10	141.32	-141.32	2.51	6.71	68.62	2.71	0.18	0.12	6.57	224.52	102.62	0.31	0.01	0.20	4.35	18.19	34.03	1.82	2.70	3.49	<0.0	26.36
SV Peak 10	140	-140.00	1.27	2.97	80.28	2.10	0.15	0.11	7.99	145.67	67.93	0.30	0.01	0.19	4.22	17.64	33.01	1.62	2.31	3.38	25.82	12.04
SV Peak 10	139	-139.00	3.62	10.67	59.51	0.96	0.18	0.04	5.46	159.19	42.48	0.29	0.01	0.18	4.09	17.11	32.01	0.81	3.01	3.28	<0.0	44.58
SV Peak 10	138	-138.00	0.77	6.45	51.20	1.04	0.16	0.12	3.95	102.65	44.33	0.28	0.01	0.18	3.97	16.60	31.06	1.31	2.60	1.80	<0.0	27.77
SV Peak 10	137	-137.00	2.65	10.26	51.59	1.02	0.16	0.14	5.46	314.02	38.43	0.27	0.01	0.17	3.85	16.10	30.12	0.61	2.30	3.80	33.81	45.54
SV Peak 10	136	-136.00	0.64	6.46	51.17	0.80	0.18	0.07	5.10	416.27	24.92	0.27	0.01	0.17	3.73	15.62	29.22	0.71	3.11	2.99	<0.0	29.96
PT 10	118	-118.00	8.90	70.41	4.57	0.84	1.64	0.10	80.61	79.46	162.59	1.69	3.89	0.08	0.08	7.28	89.10	73.15	5.29	5.88	20.31	121.84
PT 10	117	-117.00	2.40	11.75	34.11	2.78	0.27	0.11	6.62	391.90	147.25	1.13	2.59	0.05	0.05	4.86	69.40	93.00	5.98	3.92	43.66	84.10
PT 10	116	-116.00	11.07	75.60	1.66	0.64	1.41	0.11	67.18	89.00	142.46	1.41	3.24	0.06	0.06	6.07	74.25	43.55	6.21	4.40	63.86	156.98
PT 10	115	-115.00	9.52	79.26	4.85	0.63	1.60	0.10	79.75	81.34	166.15	1.28	2.95	0.06	0.06	5.52	67.50	74.22	4.14	4.46	60.92	452.60
PT 10	114	-114.00	9.79	76.36	2.54	0.64	1.44	0.09	60.39	54.90	153.44	1.17	2.68	0.05	0.05	5.02	61.36	123.63	3.91	4.05	62.95	479.64
PT 10	113	-113.00	11.23	89.45	7.02	0.63	1.39	0.09	61.40	44.79	137.69	1.06	2.43	0.05	0.05	4.56	55.78	111.78	4.14	3.69	15.23	412.01
PT 10	112	-112.00	2.40	13.16	45.64	0.95	0.09	0.17	4.23	317.53	41.06	0.96	2									

PT 10	59	-59.00	5.70	65.40	1.85	0.70	1.25	0.05	86.98	90.01	184.07	0.23	2.26	0.11	0.13	3.74	46.48	57.31	2.53	2.23	40.29	108.08
PT 10	58	-58.00	5.86	79.92	2.02	0.68	1.29	0.04	97.09	94.06	184.07	0.21	3.59	0.12	0.16	3.44	58.61	28.66	7.36	2.39	62.85	108.97
PT 10	56	-56.00	3.72	15.82	46.68	0.79	0.64	0.02	9.10	284.19	12.14	0.11	1.60	0.02	0.06	16.17	65.68	50.40	5.07	1.51	<LOD	36.19
PT 10	55	-55.00	4.91	67.60	9.32	0.48	1.75	0.10	73.83	64.73	3.03	0.03	1.00	0.04	0.10	3.44	97.50	37.55	5.98	1.70	81.29	242.43
PT 10	54	-54.00	7.60	76.31	15.56	0.44	0.09	0.16	113.27	92.03	35.40	0.30	2.24	0.01	0.11	2.93	73.76	88.60	5.30	2.38	107.38	165.19
PT 10	53	-53.00	8.73	44.79	2.57	1.06	1.04	0.05	44.50	20.23	195.19	0.29	2.16	0.04	0.12	3.84	46.48	146.78	2.76	2.50	53.95	31.16
PT 10	52	-52.00	1.74	5.67	49.72	1.00	1.63	0.04	17.19	184.07	218.45	0.29	2.06	0.04	0.08	3.34	119.23	126.93	5.06	2.90	<LOD	5.63
PT 10	49	-49.00	1.44	9.29	43.37	0.71	1.25	0.10	32.36	144.62	203.28	0.26	2.97	0.06	0.05	3.23	75.78	126.59	7.13	6.31	<LOD	28.33
PT 10	48	-48.00	3.86	12.72	23.07	0.59	1.41	0.10	53.60	51.58	225.53	0.32	2.00	0.11	0.09	3.44	71.74	91.54	4.14	1.07	18.33	35.40
PT 10	47	-47.00	4.76	58.27	10.17	0.63	1.35	0.07	80.91	36.41	219.46	0.23	2.81	0.11	0.13	4.04	59.61	102.41	2.30	3.10	39.97	32.07
DR 10	42	-42.00	0.37	4.38	30.60	0.97	0.11	0.17	6.04	315.54	33.04	0.14	0.00	0.11	3.79	21.22	29.36	1.10	5.61	2.00	37.88	22.84
DR 10	32	-32.00	0.55	3.24	24.22	0.94	0.23	0.15	4.05	269.02	43.15	0.31	0.00	0.09	4.03	9.09	23.63	0.89	5.21	2.32	40.27	57.23
DR 10	24	-24.00	0.54	5.57	35.50	1.44	0.19	0.25	4.67	164.85	66.75	0.23	0.01	0.15	4.31	26.27	19.11	0.89	4.80	1.96	43.12	46.39
DR 10	12	-12.00	0.58	5.56	36.88	0.94	0.37	0.06	8.09	163.84	61.69	2.95	0.02	0.19	4.20	37.39	20.33	0.96	3.70	3.79	42.02	38.69
DR 10	11	-11.00	0.67	6.65	44.61	0.89	0.28	0.20	5.06	166.90	58.66	0.47	0.03	0.16	4.02	15.16	18.04	1.16	4.00	2.03	40.23	30.36
DR 10	9	-9.00	0.66	10.43	43.21	0.99	0.40	0.20	7.08	34.39	96.75	2.77	0.04	0.18	3.82	36.38	19.71	1.56	4.10	0.12	38.18	35.52
DR 10	7	-7.00	0.55	3.90	68.72	0.96	0.15	0.08	6.07	223.51	114.96	0.35	0.02	0.28	2.96	35.67	20.94	2.22	4.60	0.74	20.57	30.97
DR 10	5	-5.00	1.05	8.71	50.25	1.94	0.33	0.11	5.19	182.04	114.62	0.21	0.02	0.76	3.43	20.21	22.55	1.93	5.61	2.69	34.32	47.62
DR 10	0	0.00	0.79	7.46	70.35	1.69	0.29	0.10	4.51	158.38	99.72	0.18	0.02	0.66	2.99	17.58	19.61	1.36	4.70	2.34	16.98	53.64

Table A 1. 648 rows of data from ED-XRF measurements from samples collected from the Decie Ranch, Poplar Tank, Sullivan Peak, Dugout Mountain members.

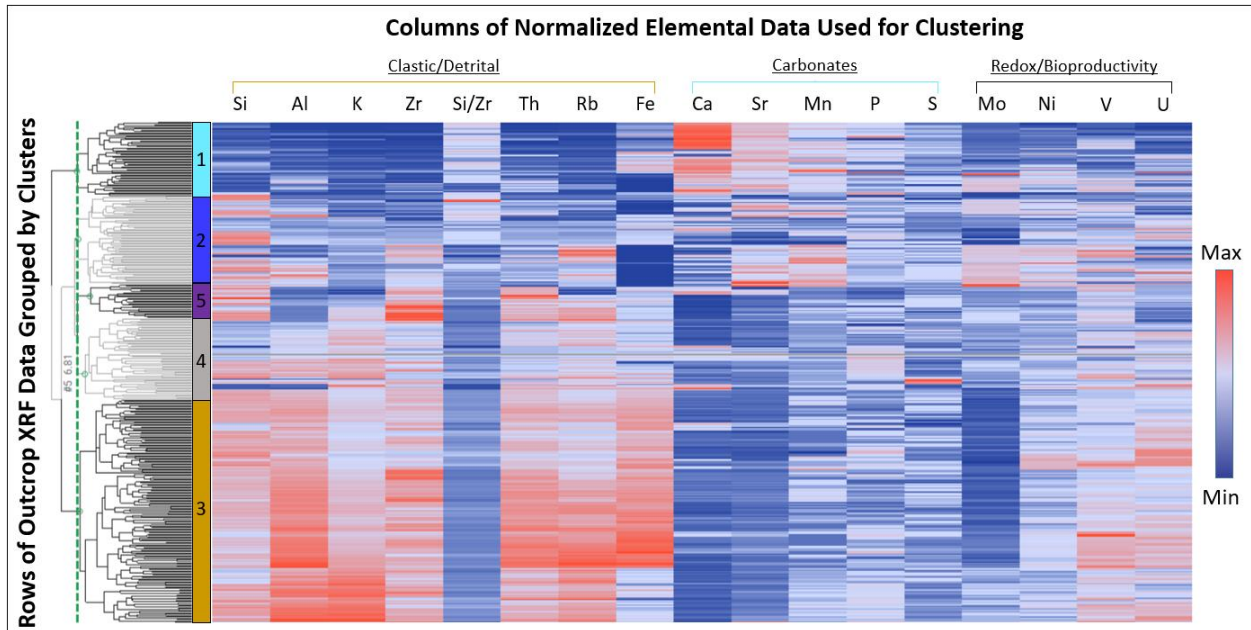


Figure A 1. Dendrogram visualization tree produced in TIBCO Spotfire. Rows of ED-XRF data are clustered together (y-axis) and based on similarity of elemental data, specifically relative abundance clastic/detrital, carbonate, redox, and bioproductivity/paleoproductivity proxies (x-axis). Higher measured elemental abundance is colored red, lower abundance in blue.

Facies 1		Facies 2		Facies 3		Facies 4		Facies 5	
Ca	3.95	Mo	3.12	K	1.43	S	1.92	Zr	1.50
Sr	2.56	Si/Zr	2.06	Al	1.41	U	1.24	Th	1.27
Si/Zr	1.94	Mn	1.75	Rb	1.36	Ni	1.21	Si	1.22
Mn	1.53	Ni	1.18	Th	1.30	P	1.14	V	1.00
Mo	1.51	S	1.13	Zr	1.29	K	1.07	Fe	0.82
P	1.19	Si	1.00	Fe	1.21	Si	1.06	Sr	0.81
Ni	0.81	P	0.97	Si	1.17	Al	1.06	S	0.76
S	0.79	V	0.88	V	1.15	Rb	1.02	K	0.75
V	0.71	Sr	0.82	U	1.14	Fe	1.02	Ni	0.74
U	0.69	Ca	0.81	Ni	0.96	Th	0.99	Rb	0.73
Fe	0.67	Rb	0.81	P	0.95	Zr	0.99	P	0.67
Th	0.41	U	0.81	S	0.72	V	0.98	U	0.65
Si	0.31	Fe	0.81	Mn	0.72	Sr	0.66	Mn	0.62
Zr	0.29	Al	0.76	Sr	0.70	Mn	0.64	Ca	0.59
K	0.25	Zr	0.69	Si/Zr	0.50	Si/Zr	0.60	Mo	0.58
Al	0.24	Th	0.65	Ca	0.35	Ca	0.46	Si/Zr	0.45
Rb	0.24	K	0.56	Mo	0.33	Mo	0.25	Al	0.42

$$\text{Partitioning Index}_{\text{Element } x} = \frac{\text{Avg in Cluster}}{\text{Avg in Dataset}}$$

Figure A 2. Partitioning index displaying elemental distribution between each facies derived from hierarchal clustering. Elements are colored and listed in order of significance for each facies.

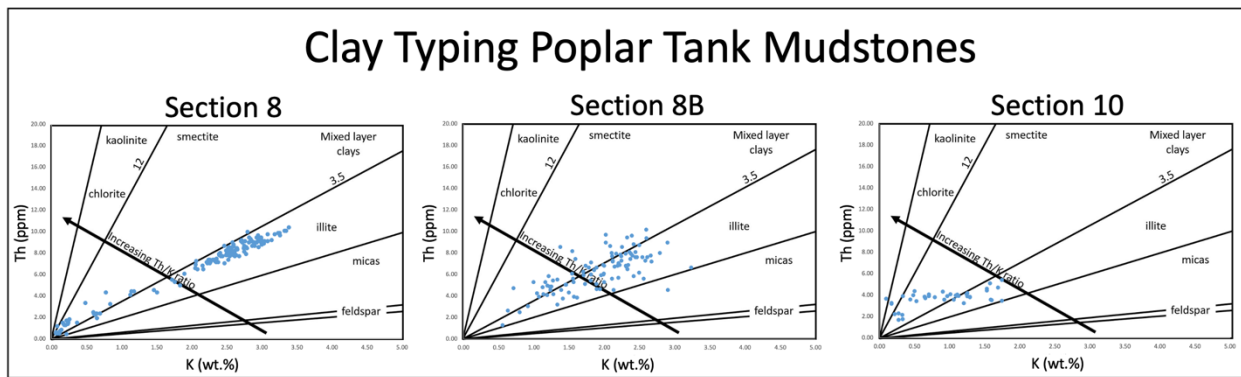


Figure A 3. Th-K cross plots demonstrating clay mineralogy within the Poplar Tank Member at each measured section. Plots indicate that the dominant clay mineralogy is illite and mixed layer.

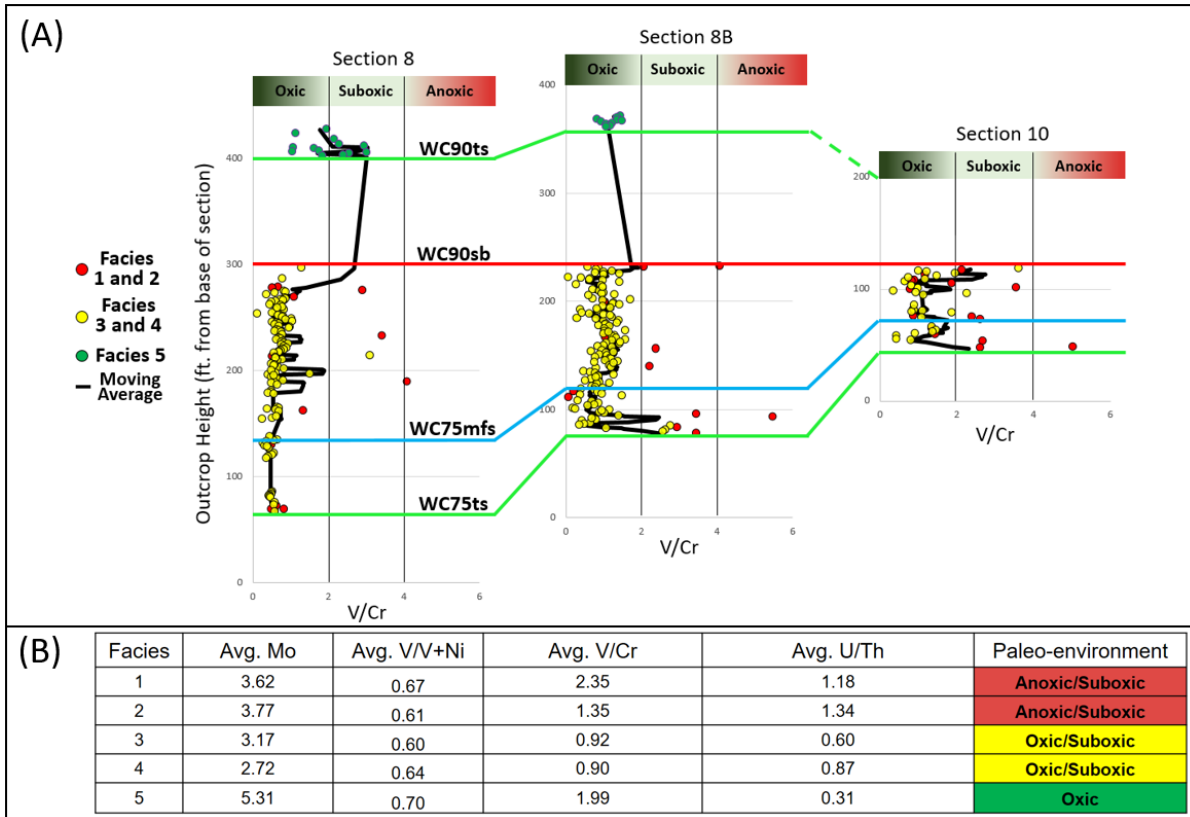


Figure A 4. (A) Paleoredox through time at each measured section is illustrated and denoted by elemental distribution of V/Cr values. Anoxic/suboxic conditions (Facies 1 and 2, red color), oxic/suboxic (Facies 3 and 4, yellow color), oxic (Facies 5, dark green color). Sequence stratigraphic interpretations denoted by the transgressive surface (WC75ts and WC90ts – green line), maximum flooding surface (WC75mfs – blue line), and sequence boundary (WC90sb – red line). (B) Average values of paleoredox proxies and interpreted redox conditions of the paleo-environment denoted in table.

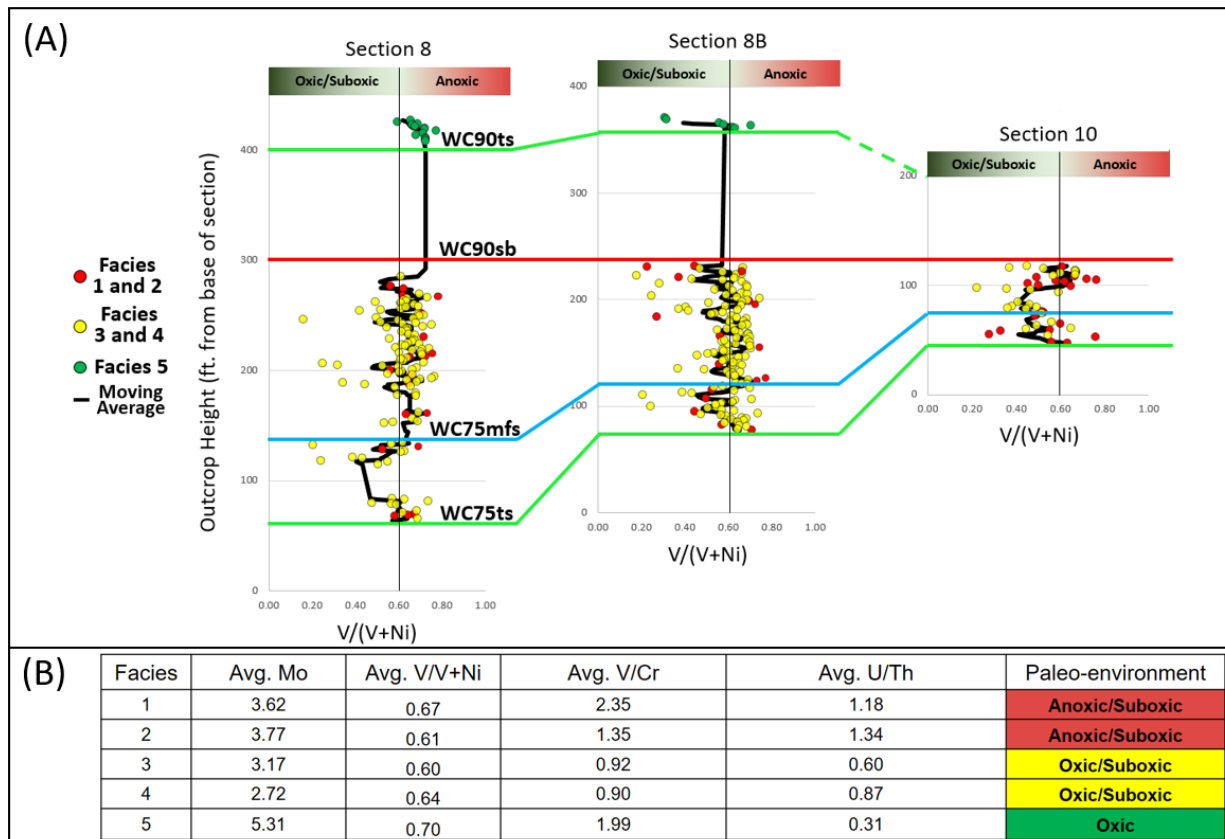


Figure A 5. (A) Paleoredox through time at each measured section is illustrated and denoted by elemental distribution of $V/(V+Ni)$ values. Anoxic/suboxic conditions (Facies 1 and 2, red color), oxic/suboxic (Facies 3 and 4, yellow color), oxic (Facies 5, dark green color). Sequence stratigraphic interpretations denoted by the transgressive surface (WC75ts and WC90ts – green line), maximum flooding surface (WC75mfs – blue line), and sequence boundary (WC90sb – red line). (B) Average values of paleoredox proxies and interpreted redox conditions of the paleo-environment denoted in table.

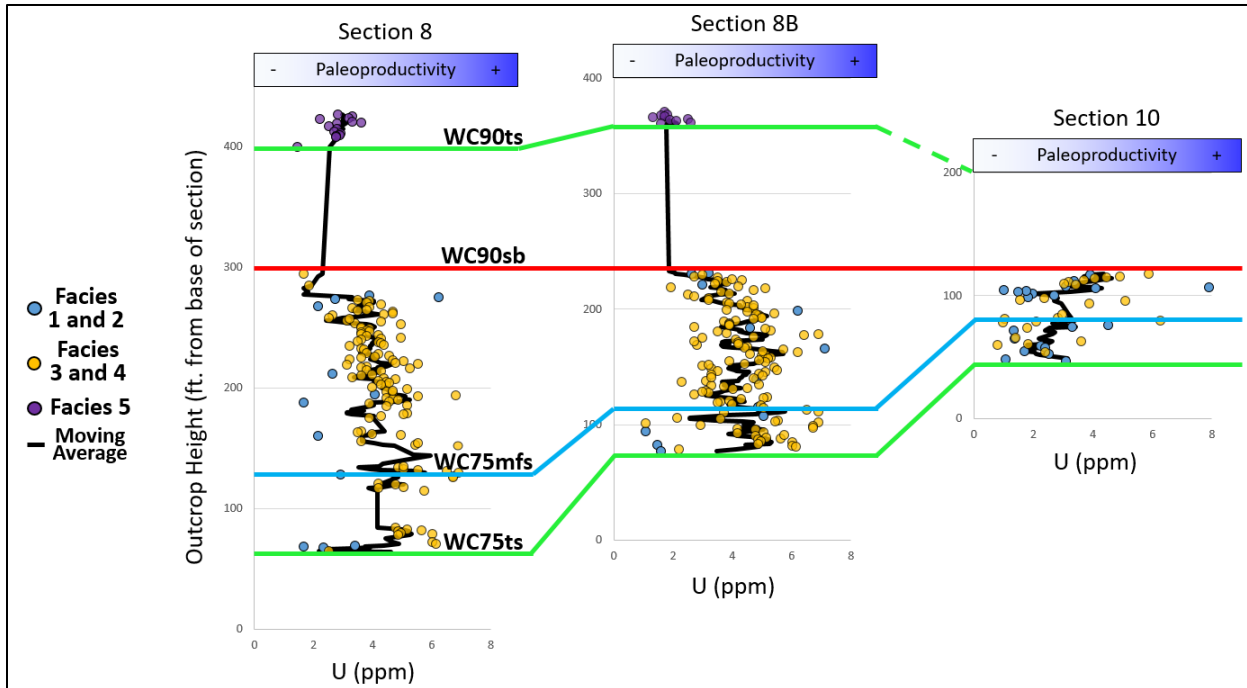


Figure A 6. Paleoproductivity/bioproductivity illustrated by measured values of uranium (U), colored by Facies representation at each measured section. Sequence stratigraphic interpretations denoted by the transgressive surface (WC75ts and WC90ts – green line), maximum flooding surface (WC75mfs – blue line), and sequence boundary (WC90sb – red line).

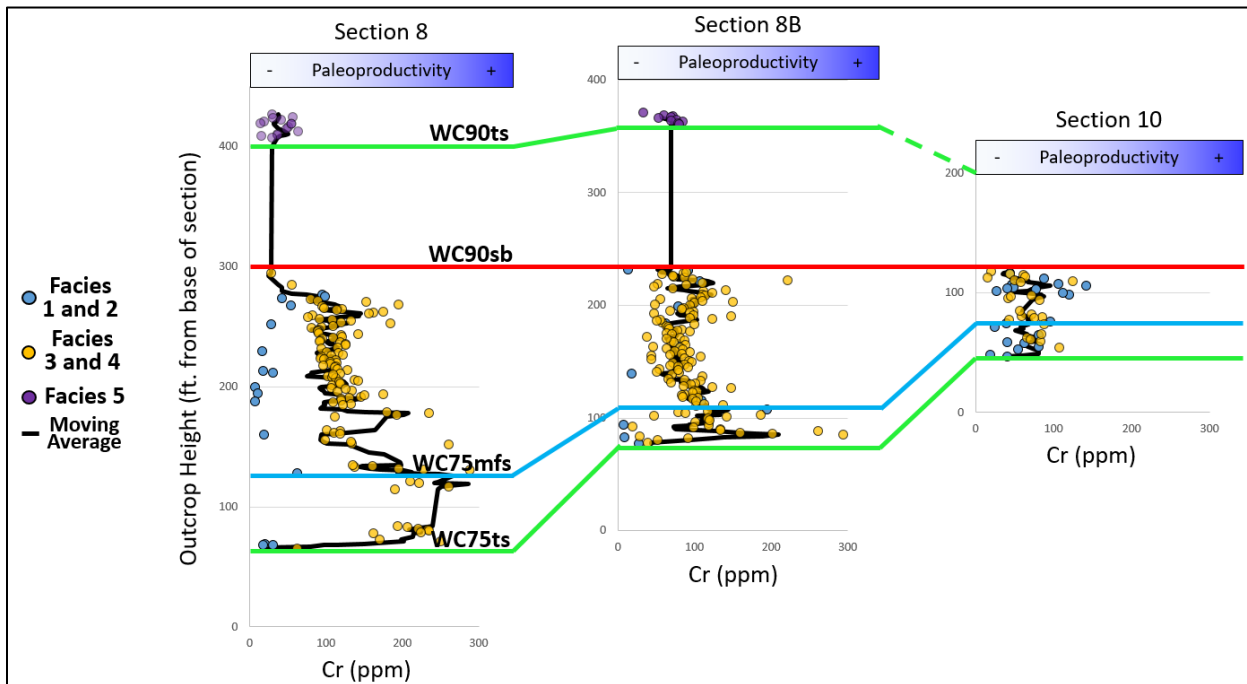


Figure A 7. Paleoproductivity/bioproductivity illustrated by measured values of chromium (Cr), colored by Facies representation at each measured section. Sequence stratigraphic interpretations denoted by the transgressive surface (WC75ts and WC90ts – green line), maximum flooding surface (WC75mfs – blue line), and sequence boundary (WC90sb – red line).

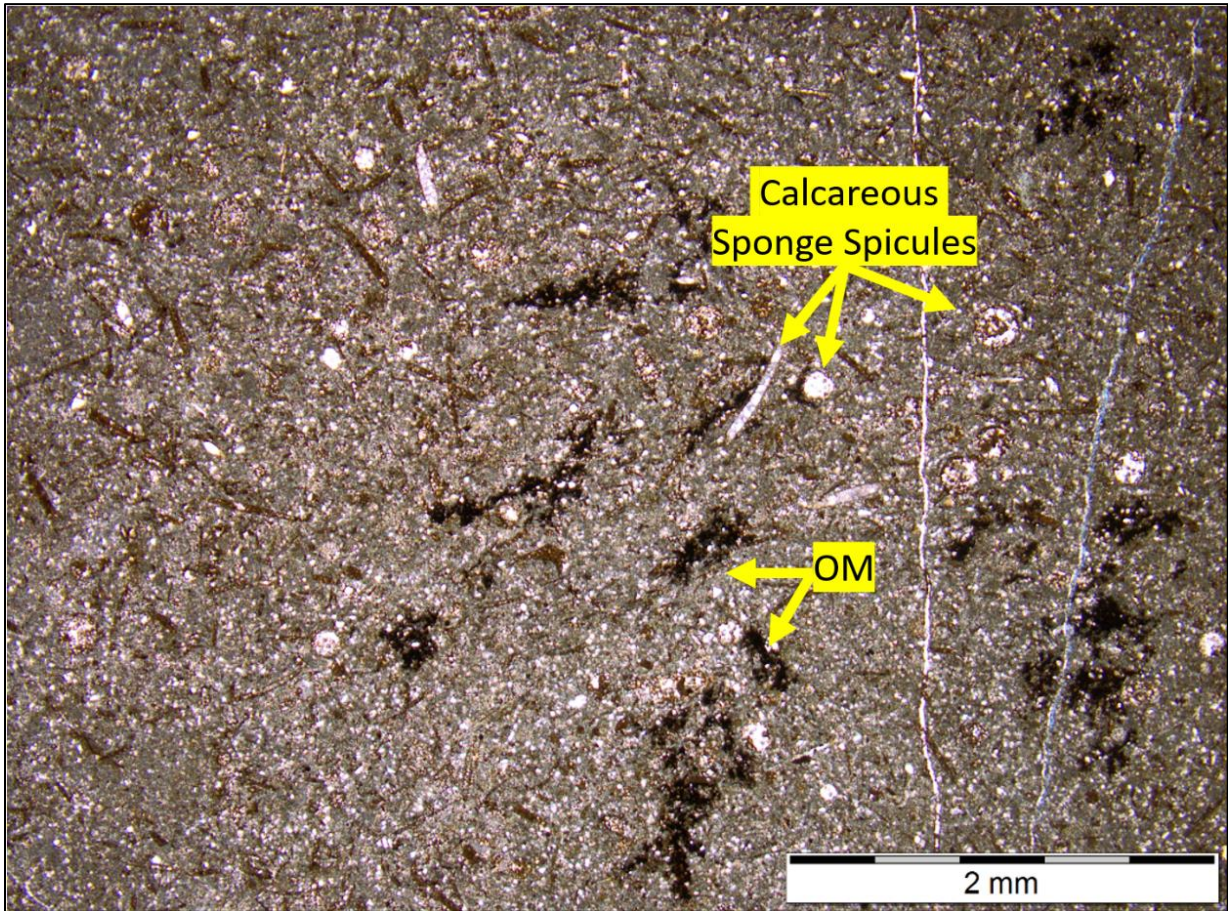


Figure A 8. Skeletal wackestone with numerous fine-grained bioclasts. Abundant calcareous sponge spicules as well as lime mud. Organic matter occurs as black discontinuous lenses.

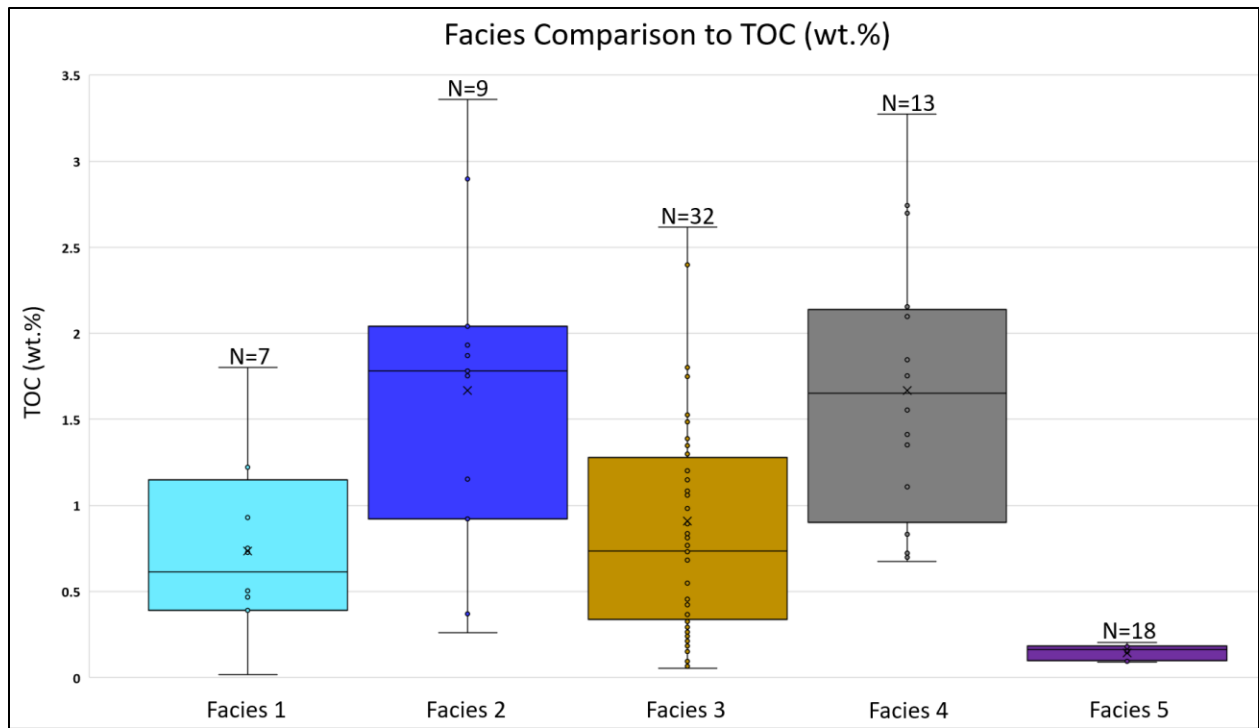


Figure A 9. Box plot comparison of measured TOC from each facies. Median and mean of TOC is denoted by the solid black line and x, respectively, within each box. Higher average TOC values are plotted within Facies 2 (calcareous silty mudstone) and Facies 4 (siliceous mudstone/siltstone). Basal Dugout Mountain shale and siltstone of Facies 5 contains the lowest TOC content.

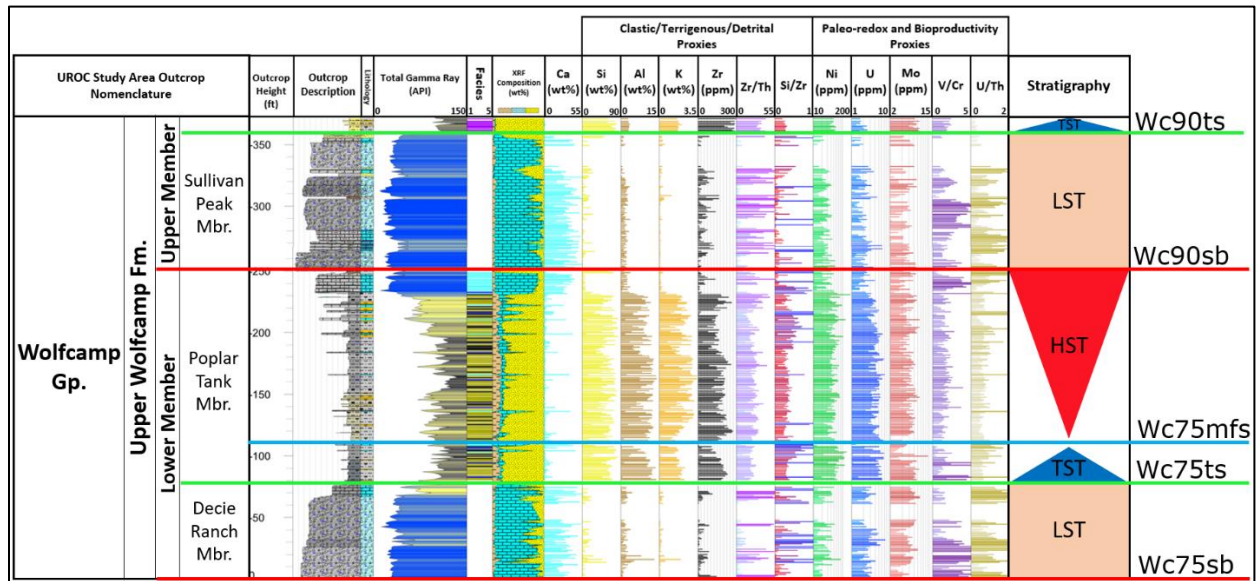


Figure A 10. Elemental distribution, outcrop description, total gamma ray, and facies of Section 8B. Sequence boundary (red), transgressive surface (green), and maximum flooding surface (blue) based on observed outcrop sedimentology, total gamma ray, and chemostratigraphic proxies.

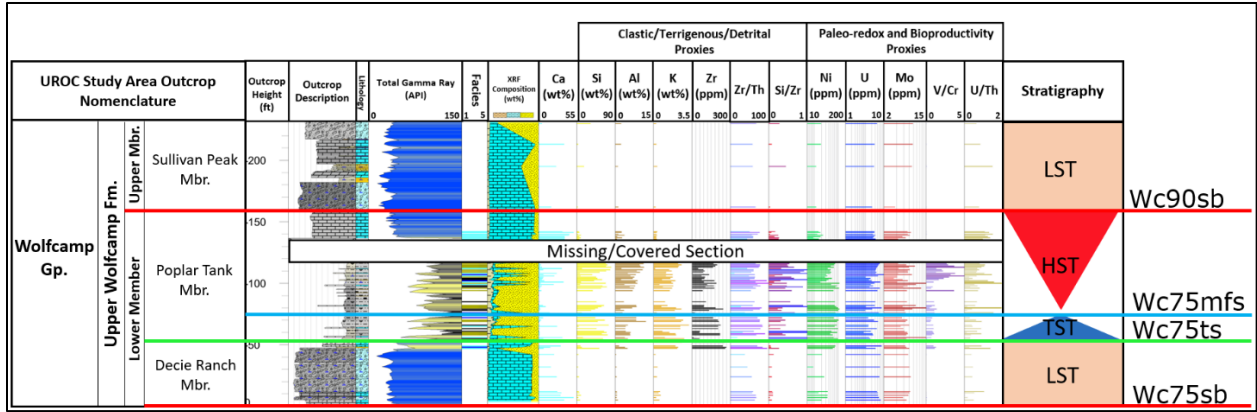


Figure A 11. Elemental distribution, outcrop description, total gamma ray, and facies of Section 10. Sequence boundary (red), transgressive surface (green), and maximum flooding surface (blue) based on observed outcrop sedimentology, total gamma ray, and chemostratigraphic proxies.

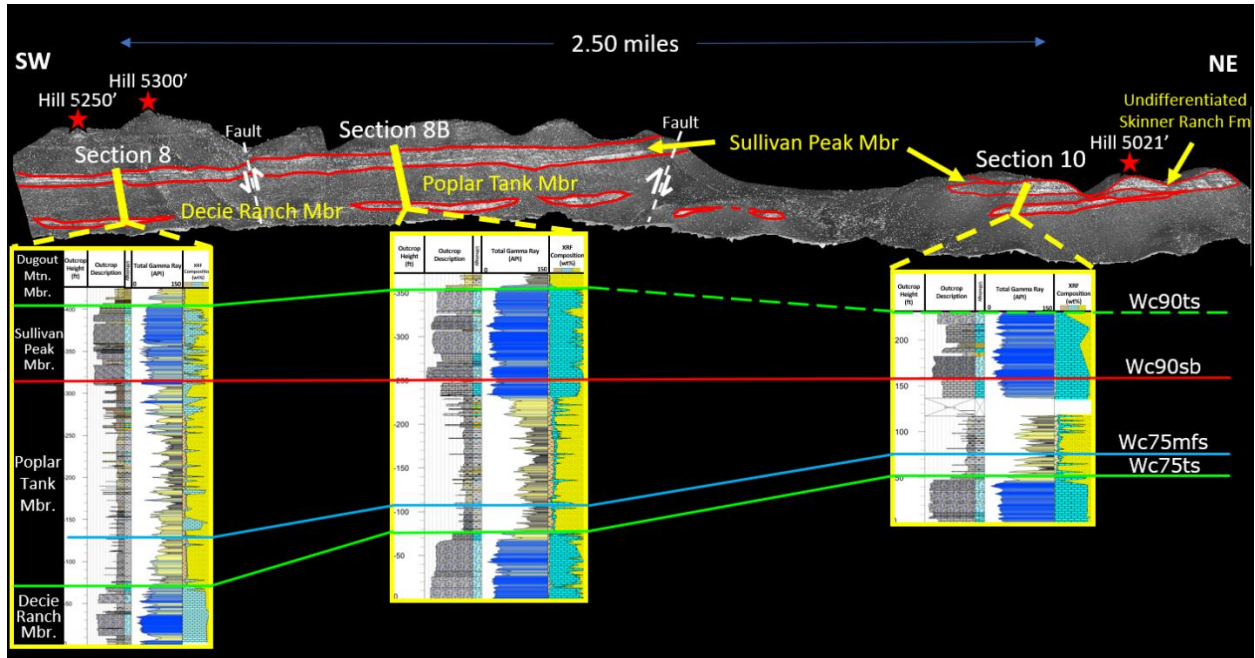


Figure A 12. Stratigraphic correlations between measured sections of the study area. Outcrop description, total gamma ray, and gross compositional profiles of the respective members were illustrated within Easycore software. Sequence stratigraphic interpretations denoted by the transgressive surface (WC75ts and WC90ts – green line), maximum flooding surface (WC75mfs – blue line), and sequence boundary (WC90sb – red line).